International Scientific-Technical and Production Journal

The Paton WELDING JOURNAL

July 2006 # 7

English translation of the monthly «Avtomaticheskaya Svarka» (Automatic Welding) journal published in Russian since 1948

Founders: *E.O. Paton Electric Welding Institute of the NAS of Ukraine*
International Association «Welding»

Publisher: *International Association «Welding»*

Address:
E.O. Paton Electric Welding Institute,
International Association «Welding»,
11, Bozhenko str., 03680, Kyiv, Ukraine
Tel.: (38044) 287 67 57
Fax: (38044) 528 04 86
E-mail: journal@paton.kiev.ua
http://www.nas.gov.ua/pwj

State Registration Certificate
KV 4790 of 09.01.2001

Subscriptions:
$324, 12 issues per year,
postage and packaging included.
Back issues available.

CONTENTS

SCIENTIFIC AND TECHNICAL

Paton B.E., Lobanov L.M., Samilov V.N., Pilishenko I.S., Makhnenko O.V., Pashchin N.A., Gorinov V.A. and **Shiyan K.V.** Design and features of fabrication technology of a large-sized transformable shell structure 2

Portnov O.M. and **Maksimov S.Yu.** Numerical modelling of absorption of gases by deposited metal in wet underwater welding 11

Kulik V.M. and **Vasiliev V.G.** Variations in structure and properties of HAZ metal in welded joints on steel 30KhGSA in arc treatment 16

Borisov Yu.S., Golnik V.F., Ipatova Z.G., Mits I.V., Saakov A.G. and **Saakov V.A.** Aluminoceramic plasma coatings 22

Pokhmursky V.I., Student M.M., Ryabtsev I.A., Sidorak I.I., Dzioba Yu.V., Dovgunyk V.M. and **Formanek B.** Influence of electric arc metallizing modes and compositions of applied flux-cored wires on structure and abrasive wear resistance of coatings 26

INDUSTRIAL

Thomy C., Kohn H. and **Vollertsen F.** Application of high-power fibre lasers in laser and laser-MIG hybrid welding 31

Kalita W., Kolodziejczak P., Kwiatkowski L., Grobelny M. and **Hoffman J.** Properties of CO_2-laser welded joints of dissimilar magnesium alloys 34

Koehler G., Mueller G., Basler U., Dahms St., Luhn R., Kasch S. and **Waechter S.** Glass joining technologies and examples of their application 38

Zaruba I.I., Dymenko V.V., Andreev V.V. and **Shatan A.F.** Power sources with improved performance for AC arc welding 43

BRIEF INFORMATION

Zhadkevich M.L., Tyurin Yu.N., Kolisnichenko O.V. and **Mazunin V.M.** On heating and acceleration of disperse particles with pulse plasma 48

Lankin Yu.N., Masalov Yu.A. and **Bajshtruk E.N.** Schematic for control of welding machine drives 50

Theses for a scientific degree 52

NEWS

Cooperation between PWI and Brazilian Welding Society 54

Developed at PWI 30, 42, 51

DESIGN AND FEATURES OF FABRICATION TECHNOLOGY OF A LARGE-SIZED TRANSFORMABLE SHELL STRUCTURE

B.E. PATON, L.M. LOBANOV, V.N. SAMILOV, I.S. PILISHENKO, O.V. MAKHNENKO, N.A. PASHCHIN, V.A. GORINOV and **K.V. SHIYAN**
E.O. Paton Electric Welding Institute, NASU, Kiev, Ukraine

Main principles of design of shell-type transformable structures intended for storage of liquid and loose products, such as fuel, water, grain, etc., are described. Calculation diagrams and results of calculation of the strength and robustness of structures, as well as their ability to resist service and wind loads are presented. The technology for assembly and welding of thin-walled joints in structures with long welds is described.

Keywords: *welded structures, transformable shell, design, assembly, arc welding, residual stresses, deforming fixture, mounting*

At the modern stage of engineering development in a number of cases a contradiction is found between the need to increase the weight and dimensions of welded structures and complexity of their transportation. This is particularly urgent for space engineering, where reaching the objectives is essentially dependent on the weight and dimensions of the object.

The E.O. Paton Electric Welding Institute defined the main principles of design and manufacturing of all-welded metal shells, the dimensions of which can be reduced to those of the transportation containers for the period of transportation to orbit. Such a possibility was for the first time theoretically substantiated by B.M. Balitsky, Cand. of Sci. (Eng.), this allowing isometric transformation of closed shells from steel and titanium alloys. The structures were designed for mounting in space the living and laboratory compartments, lock chambers, passages, storage and production facilities, etc. [1].

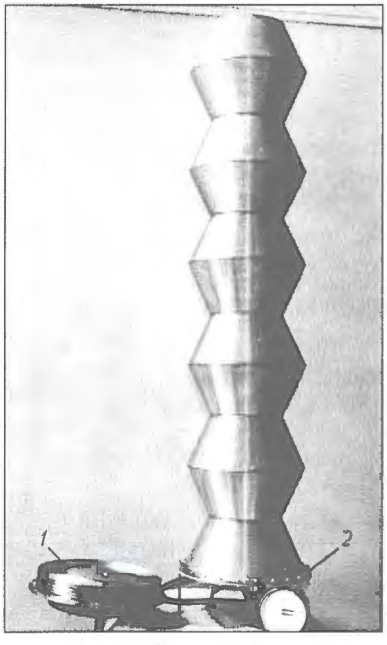

Figure 1. Mock-up of a shell structure with the base element in the form of a truncated cone for space engineering before (*1*) and after (*2*) transformation [1]

The authors defined the main requirements to welded structures of a transformable volume, namely complete factory readiness; tightness; minimum requirements for transportation; minimum labour consumption in mounting and deployment in the site.

Theoretical and laboratory research conducted at the E.O. Paton Electric Welding Institute allowed selection from a large number of currently available variants of transformable shell forming one variant, which is the simplest in terms of technology, namely transformation of the surface of a truncated cone into a corrugated disc. Substantiation of the possibility of a purposeful forming of closed shells is based on the principles of the theory of isometric surface bending, described by Kodazzi–Gauss equations. According to the theory of isometric transformations, it is assumed that a shell can be bent without tension or compression of the material, from which the shell is made.

Transformable structures are based on the principles of transformation of truncated conical shells into corrugated discs, which are conjugated by end faces into a compact package. Excess internal pressure was applied to transform it into an air-tight shell of design dimensions and volume. Figure 1 shows a mock-up of the shell of a transformable volume from VT1-0 titanium alloy of 400 mm diameter with 0.1 mm wall thickness. The shell has the height of 65 mm in the transportation position, and of 2000 mm in the working position.

The objective of this work was development of calculation procedure for assessment of the stressed-strained state of a large-sized welded structure of a transformable volume for liquid product storage, as well as technology of its manufacture. For this purpose the shell structural material was selected, calculation estimate of the stressed-strained state of the structural elements of the shell at different loading patterns was conducted, technology of shell assembly and welding

was developed, experiments on its transformation, installation and mounting in site were conducted.

High-alloyed 08Kh18N10T steel (19.5 wt.% Cr) was selected as the shell structural material which is characterized by a high corrosion resistance, good weldability and workability. An experimental welded tank of 40 m^3 volume, 3.8 m diameter with 2.5 mm wall thickness has been designed and manufactured, and its schematics is shown in Figure 2.

Design calculation of the stressed-strained state and strength characteristics of this tank has been performed, allowing for its weight proper, weight of the stored product, pressure of the product liquid column and wind load at wind velocity of 50 m/s.

The theory of axially symmetrical deformation of thin-walled shells of revolution [2] was used to determine the residual stresses in the shell wall after its deployment and their interaction with stresses caused by hydrostatic pressure of the poured in liquid and weight of the structure proper. Under the above loading conditions, the shell material behaves in keeping with the theory of elasto-plastic flow at isotropic deformation strengthening in combination with Mises yield criterion. Additional stresses from the wind load were determined on the basis of the theory of elasticity of thin-walled conical shells of revolution for the case of asymmetrical loading [3]. Checking calculation for strength and loss of stability at compression was performed for vertical support columns, on which the tank was mounted.

The tested tank consists of four sections, which at deployment take the shape of thick-walled conical shells with end face section diameters of 3800 and 2750 mm at cone height H_c = 1126 mm, this corresponding to the final angle of conicity $\alpha_c \cong 25°$ (see Figure 2). Conical bottoms with necks are located at the top and bottom of the tank. Schematic of nodes *A, B, E* connecting the sections to each other by rings and of nodes *F, G* connecting the bottoms to the reinforcement in the neck zone is shown in Figure 3.

During tank deployment the geometry of the bottoms and nodes *D, E, B, A, C* does not change significantly. Transformation mainly involves four sections *DE, EB, BA, AC* of each tank. At forming, the initial corrugations change their dimensions, their number remaining constant. It may be assumed that the section end faces have constant diameters, determined by the respective rings, i.e. distance *H* between the end faces is increased at transformation.

A certain arbitrary condition of deployment was considered, when the current angle of conicity α of the shell at deployment is less than α_c (Figure 4). The length of the individual corrugation base $2b(\alpha) = \frac{1900 - 1375}{N \sin \alpha}$ [mm], where *N* is the number of the same corrugations; $H = (1900–1375) \times \text{ctg}\ \alpha$ [mm]. In *y, x* system of coordinates the geometry of the median of a corrugated conical surface generatrix can be described by the following expression:

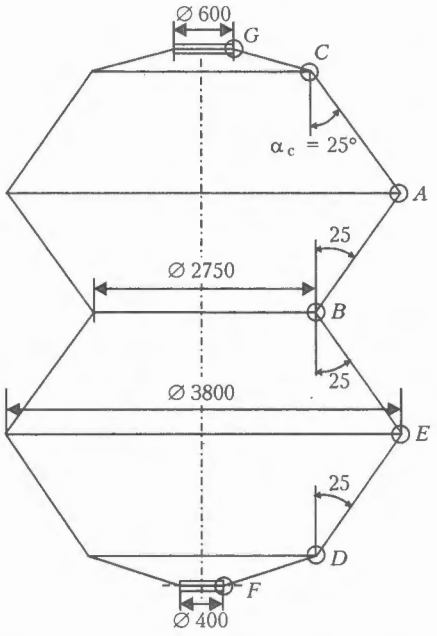

Figure 2. Schematic of a large-sized tank in the deployed condition (for designations see the text)

$$y = a\left(1 - \cos\frac{\pi x}{b}\right),$$

where *a, b* is the half-height and half-length of the corrugation, respectively.

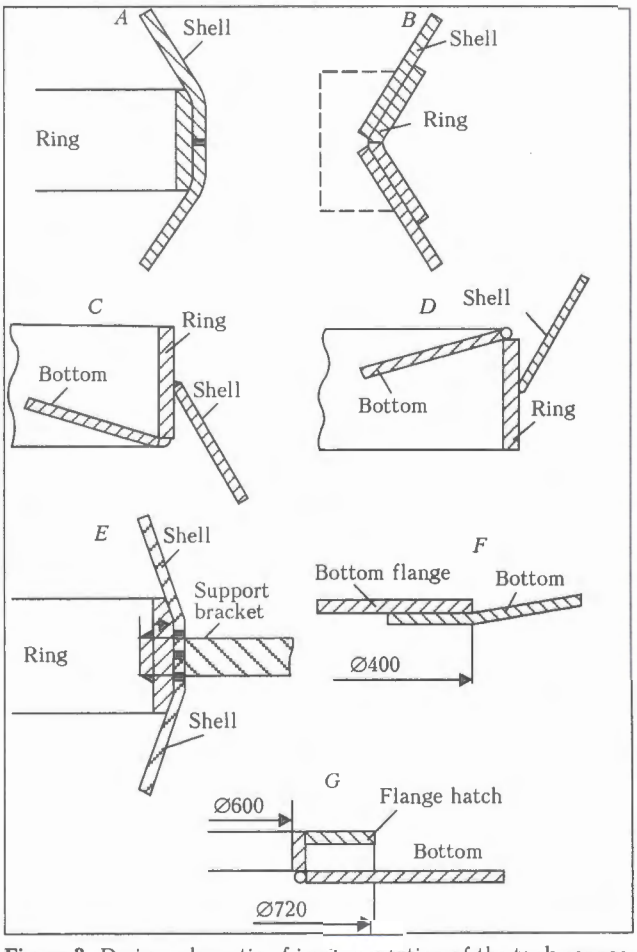

Figure 3. Design schematic of implementation of the tank connection nodes

Design values of half-height a and half-length b of the corrugation, as well as maximum of curvature K_s^{max} of the shell, depending on the angle of conicity α

α, degr	$\pi a/b$	$2b$	$2a$	K_s^{max}, 1/mm
25.0	0	177.0	0	0
26.0	0.40	171.2	21.8	0.00734
27.4	0.70	163.4	36.4	0.04345
30.9	1.00	145.9	46.5	0.04304
35.8	1.40	128.0	57.2	0.16869
41.7	1.80	112.6	64.5	0.10039
53.0	2.40	93.9	71.7	0.16051
63.1	2.80	84.1	75.0	0.20908
70.2	3.00	79.7	76.0	0.23639
81.3	3.20	75.9	77.4	0.26477
90.0	3.29	75.0	78.6	0.27548

The length of the median generatrix of one corrugation is equal to

$$B = 4\int_0^{b/2}\sqrt{1+\left(\frac{dy}{dx}\right)^2}\,dx,$$

where

$$\frac{dy}{dx} = a\frac{\pi}{b}\sin\frac{\pi x}{b}. \qquad (1)$$

Value B is known and equal to

$$B = 2b(\alpha_c) = \frac{1900-1375}{N\sin\alpha_c} = 177\ [\text{mm}].$$

At $N = 7$ and $\alpha_c = 25°$ from (1) dimensions $2a$ and $2b$ of corrugation can be found for different α values from the following system of equations:

$$\sin\alpha = \frac{2}{\pi}\sin\alpha_c E(k)\sqrt{1+x^2},\quad b = \frac{1900-1375}{N\sin\alpha},$$

$$x = \frac{\pi a}{b},\quad k^2 = \frac{x^2}{\sqrt{1+x^2}},$$

where $E(k)$ is the complete elliptic integral of the second kind.

The Table gives the results of such a calculation at $\alpha_c = 25°$ and data on the relative change of maximum curvature K_s^{max} of the shell along the generatrix, i.e. in the corrugation apex. It can be seen from the Table that the height of corrugation $2a$ and curvature K_s^{max} decrease with reduction of angle α. In the thin-walled shell, the change of curvature ΔK_s determines $\Delta\varepsilon_{ss}$ increment of the respective deformations along the generatrix through the product of $\Delta K_s h/2$, where h is the wall thickness. The tabulated data show that increments of maximum deformations $\Delta\varepsilon_{ss}^{max} \times (\sim K_s^{max}\,\delta/2)$ during deployment of the shell can be equal to 20–25 % in the extreme fibres. For austenitic steel, however, development of such deformations does not create any serious hazard, considering the good formability of this steel of a small thickness.

Distribution of residual stresses in the shell after deployment was calculated by applying the method of successive tracing of development of elasto-plastic deformations at increase of internal pressure. The following system of coordinates was used: s is the coordinate along a curvilinear generatrix; β is the angle of revolution around axis z (Figure 5). Continuous generatrix $0 < s < 7B$ is represented by discrete sections of length Δs with respective numbering of the nodes (ends of sections) 0, 1, 2, ..., $n-1$, n, $n+1$ (see Figure 4).

For each node n with coordinate s_n value of coordinate $x_n(\alpha)$ is determined by the following dependence:

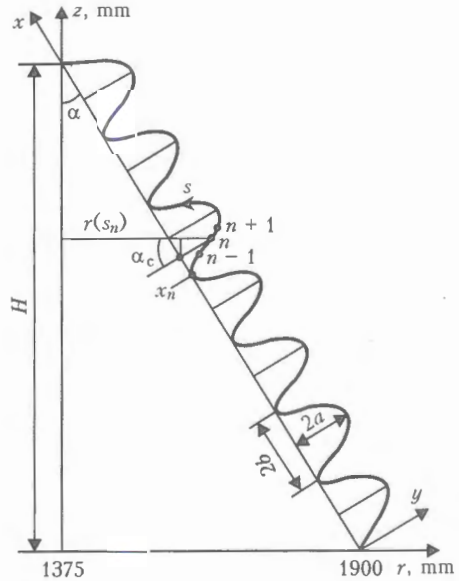

Figure 4. Schematic of forming the corrugated wall of the tank depending on angle α

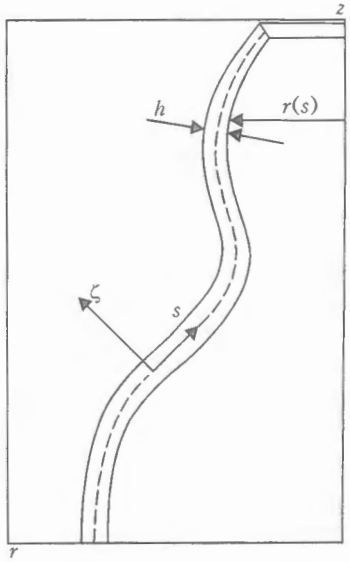

Figure 5. Schematic of a thin-walled shell with an arbitrary shape of the meridian

$$x_n(\alpha) = x_{n-1}(\alpha) + \frac{\Delta s_{n,\,n-1}}{\sqrt{1 + \left(\frac{a\pi}{b}\right)^2 \sin^2 \frac{\pi x_{n-1}}{b}}}.$$

Knowing coordinate $x_n(\alpha)$, we will find $y_n(\alpha)$ from (1), and then shell radius $r_n(s_n, \alpha)$:

$$r_n(s_n, \alpha) = r_0 \left[\frac{H(\alpha)}{\cos\alpha} - x_n(\alpha) - y_n(\alpha)\,\mathrm{tg}\,(\alpha)\right] \sin\alpha +$$

$$+ y_n(\alpha)/\cos\alpha = 1900 - x_n \sin\alpha + y_n \cos\alpha,$$

where $r_0 = R_1 = 1375$ mm; $H(\alpha) = 525$ ctg α [mm]; $y_n = a\left(1 - \cos\frac{\pi x_n}{b}\right)$.

From $r_n(s_n, \alpha)$ we determine the values of curvature K_s^n and K_β^n for each n-th point by the following dependencies [1]:

$$K_s^n = -\frac{r_n''}{\sqrt{1 - r'^2}}; \quad K_\beta^n = \frac{\sqrt{1 - r'^2}}{r_0},$$

where $r_n'' = \frac{r_{n+1} + r_{n-1} - 2r_n}{\Delta s^2}$; $r_n' = \frac{r_{n+1} - r_n}{\Delta s}$ (n = = 1, 2, ...). Obtained results are given in Figure 6.

For each moment of deployment determined by α, the level of internal pressure P guaranteeing the continuity of the deployment process, was assessed. This is related to the fact that with decrease of the current angle α of conicity and, hence, dimensions $2a$ of corrugations, process continuation requires increase of pressure P. Taken as the criterion of the required level of pressure P at a given value of α was such a value of P, at which a rather well-developed plastic flow occurs. Data on stresses and strains obtained for angle α were used as the initial data for the next step of tracing, determined by the next angle $\alpha - \Delta\alpha$. If pressure P is not increased, partial unloading takes place, confirming the need to increase pressure P in order to ensure the transformation process.

According to the theory of thin-walled shells, the stressed-strained state is determined by displacement of U and W points of the median surface, i.e. $U(s)$ and $W(s)$, stresses $\sigma_{ss}(s, \zeta)$, $\sigma_{\beta\beta}(s, \zeta)$ and strains $\varepsilon_{ss}(s, \zeta)$ and $\varepsilon_{\beta\beta}(s, \zeta)$, where ζ is the coordinate across the shell thickness, calculated from its median surface (Figure 5). Here a calculation algorithm of solving the elastoplastic problem was used [4]. Solution is reduced to determination of six functions of s coordinate: force $N_s = \int_{-\delta/2}^{\delta/2} \sigma_{ss} d\zeta$, moment $M_s = \int_{-\delta/2}^{\delta/2} \sigma_{ss}\zeta d\zeta$, intersecting force Q_s, displacements ΔU and ΔW and increment of the angle of revolution of $\Delta\Theta$ normals.

Stresses σ_{ss} and $\sigma_{\beta\beta}$ are related to increments of displacements and angle of revolution by the following dependencies [2, 4]:

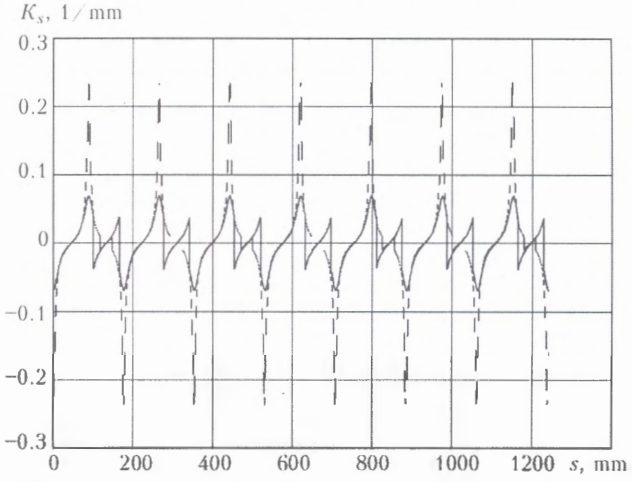

Figure 6. Distribution of curvature $K_s(s)$ of a corrugated tank wall at $\alpha = 35.8°$ (solid curves) and 70.2° (dashed)

$$\sigma_{ss} = A_1\left(K_s\Delta W - \frac{\partial\Delta U}{\partial s} + \zeta\frac{\partial\Delta\Theta}{\partial s}\right) +$$

$$+ A_2(K_0\Delta U + K_\beta\Delta W + K_0\zeta\Delta\Theta) + Y_{ss};$$

$$\sigma_{\beta\beta} = A_2\left(K_s\Delta W - \frac{\partial\Delta U}{\partial s} + \zeta\frac{\partial\Delta\Theta}{\partial s}\right) +$$

$$+ A_1(K_0\Delta U + K_\beta\Delta W + K_0\zeta\Delta\Theta) + Y_{\beta\beta};$$

$$A_1 = \frac{2\psi + K}{\psi(\psi + K)}; \quad A_2 = \frac{\psi - K}{\psi(\psi + K)};$$

$$Y_{ss} = A_1 b_{ss} + A_2 b_{\beta\beta}; \quad Y_{\beta\beta} = A_1 b_{\beta\beta} + A_1 b_{ss};$$

$$b_{ss} = \left(\frac{\sigma_{ss}}{2G}\right) + b^*; \quad b_{\beta\beta} = \left(\frac{\sigma_{\beta\beta}}{2G} + b^*\right);$$

$$b^* = \left[\frac{\sigma_{ss} + \sigma_{\beta\beta}}{3}\left(K - \frac{1}{2G}\right)\right]^*,$$

where $K = 1 - 2\nu/E$ is the coefficient of bulk compression (here ν is the Poisson's ratio); $K_0 = = \partial r/r\partial s$; ψ is the function of material condition; $G = E/2(1 + + \nu)$ is the shear modulus; * is the index, referring the value to the previous tracing step, in keeping with which $\Delta U(s)$, $\Delta W(s)$ and $\Delta\Theta(s)$ are determined. At elastic deformation $\psi = 1/2G$, at plastic flow $\psi > > 1/2G$ is found from Mises yield criterion. To calculate $\psi(s, \zeta)$ at each tracing step, the iteration process from [4] was used.

At each iteration the resolving system has the following form:

$$\frac{d\mathbf{j}}{ds} = B(s)\mathbf{j} + \mathbf{f}(s), \qquad (2)$$

where vectors $\mathbf{j}$ and $\mathbf{f}$ consist of six functions of s coordinate:

$$\mathbf{j}(s) = \begin{vmatrix} N_s \\ M_s \\ Q_s \\ \Delta U \\ \Delta W \\ \Delta\Theta \end{vmatrix}; \quad \mathbf{f}(s) = \begin{vmatrix} f_N \\ f_M \\ f_Q \\ f_U \\ f_W \\ f_\Theta \end{vmatrix},$$

where

$$f_N = K_0 \times$$

$$\times \left\{ Y_{\beta_1} + \frac{1}{D} [L_{22}(Y_{s1}L_{12} - Y_{s2}L_{11}) - L_{21}(Y_{s1}L_{13} - Y_{s2}L_{12})] \right\};$$

$$f_M = K_0 \times$$

$$\times \left\{ Y_{\beta_2} + \frac{1}{D} [L_{22}(Y_{s1}L_{12} - Y_{s2}L_{11}) - L_{22}(Y_{s1}L_{13} - Y_{s2}L_{12})] \right\};$$

$$f_Q = \frac{K_\beta}{K_0} f_N - P; \quad f_U = \frac{1}{D}(Y_{s2}L_{12} - Y_{s1}L_{13});$$

$$f_W = 0; \quad f_\Theta = (Y_{s1}L_{12} - Y_{s2}L_{11}); \quad D = L_{11}L_{13} - L_{12}^2;$$

$$L_{m,n} = \int_{-\delta/2}^{\delta/2} A_m \zeta^{n-1} dz; \quad Y_{m,n} = \int_{-\delta/2}^{\delta/2} Y_{ll}\, \zeta^{n-1} dz;$$

$$m = 1, 2; \quad n = 1, 2, 3; \quad l = s, \beta.$$

$B(s)$ matrix of 6×6 size has the following form:

$$B(s) = \begin{vmatrix} a_{11} & a_{12} & \dots & a_{16} \\ a_{21} & a_{22} & \dots & a_{26} \\ \dots & \dots & \dots & \dots \\ \dots & \dots & \dots & \dots \\ a_{61} & a_{62} & \dots & a_{66} \end{vmatrix},$$

where

$$a_{11} = K_0 \left[\frac{1}{D}(L_{13}L_{21} - L_{22}L_{12}) - 1 \right];$$

$$a_{12} = \frac{K_0}{D}(L_{11}L_{13} - L_{21}L_{12});$$

$$a_{13}, a_{14} = K_0^2 \times$$

$$\times \left\{ L_{11} - \frac{1}{D} [L_{21}(L_{11}L_{13} - L_{23}L_{12}) - L_{22}(L_{21}L_{12} - L_{22}L_{11})] \right\};$$

$$a_{21} = \frac{K_0}{D}(L_{23}L_{12} - L_{22}L_{13});$$

$$a_{22} = K_0 \left[\frac{1}{D}(L_{22}L_{12} - L_{23}L_{11}) - 1 \right]; \quad a_{23} = 1;$$

$$a_{24} = K_0^2 \times$$

$$\times \left\{ L_{12} - \frac{1}{D} [L_{22}(L_{21}L_{13} - L_{22}L_{12}) - L_{23}(L_{21}L_{12} - L_{22}L_{11})] \right\};$$

$$a_{25} = a_{24} \frac{K_\beta}{K_0};$$

$$a_{26} = K_0^2 \times$$

$$\times \left\{ L_{13} - \frac{1}{D} [L_{22}(L_{22}L_{13} - L_{23}L_{12}) - L_{23}(L_{22}L_{12} - L_{23}L_{11})] \right\};$$

$$a_{31} = K_\beta \left(\frac{a_{11}}{K_0 + 1} \right) + K_s; \quad a_{32} = a_{12} \frac{K_\beta}{K_0}; \quad a_{33} = -K_0;$$

$$a_{34} = a_{14} \frac{K_\beta}{K_0}; \quad a_{35} = \frac{K_\beta}{K_0}; \quad a_{36} = a_{16} \frac{K_\beta}{K_0}; \quad a_{41} = \frac{L_{13}}{D};$$

$$a_{42} = -\frac{L_{12}}{D}; \quad a_{43} = 0; \quad a_{44} = \frac{K_0}{D}(L_{22}L_{12} - L_{21}L_{13});$$

$$a_{45} = a_{44} \frac{K_\beta}{K_0 - K_s}; \quad a_{46} = a_{21}; \quad a_{51} = 0; \quad a_{52} = 0; \quad a_{53} = 0;$$

$$a_{54} = K_s; \quad a_{55} = 0; \quad a_{56} = -1; \quad a_{61} = -\frac{L_{12}}{D};$$

$$a_{62} = \frac{L_{11}}{D}; \quad a_{63} = 0; \quad a_{64} = \frac{K_0}{D}(L_{12}L_{12} - L_{22}L_{11});$$

$$a_{65} = a_{64} \frac{K_\beta}{K_0}; \quad a_{66} = a_{22} + K_0.$$

The system of regular differential equations (2) should be complemented by conditions on the edges $s = 0$ and $s = s_0$.

Considering approximately the same behaviour of elements DE, EB, AB, AC (see Figure 2) at deployment of a tank under the action of internal pressure P it is possible to analyze just one element DE, placing the origin of coordinates $s = 0$ into point D.

In this case, the symmetry condition is applied in point E ($s = s_0$), and in point D ($s = 0$) — the condition of abutting a sufficiently rigid bottom, which can be written in the following form:

$$\begin{aligned} &s = 0 \\ &\quad N_s = PR_0/2\cos\alpha, \\ &\quad \Delta U \cos(\beta - \alpha) + W \sin(\beta - \alpha) \cong 0, \ \Delta\Theta \cong 0; \\ &s = s_0 \\ &\quad \Delta U \cos\alpha - W \sin\alpha = 0, \ Q_s = 0, \ \Delta\Theta \cong 0. \end{aligned} \tag{3}$$

Two latter conditions in (3) are taken as approximately conservative, this being related to a quite complex configuration of node D (see Figure 3). Therefore, alongside (3) also the condition of considerable yielding of node D was used as evaluation condition, having the following form:

$$\begin{aligned} &s = 0 \\ &\quad N_s = PR_0/2\cos\alpha; \\ &\quad M_s = 0; \\ &\quad Q_s = 0. \end{aligned}$$

Variation of these conditions only slightly affects the residual stresses of deployment in the entire shell, except for a small zone at $s = 0$.

The finally derived system was solved by the numerical method using a program, developed at the E.O. Paton Electric Welding Institute [2]. Such properties of austenitic steel as the modulus of elasticity $E = 2 \cdot 10^5$ MPa, Poisson's ratio $\nu = 0.3$, yield point $\sigma_y = 280$ MPa were taken into account.

Figure 7 gives the calculation data, obtained at the required pressure P for deployment of the tank with reduction of the current angle of conicity α. From the Figure it is seen that in the initial moments at $\alpha > 41°$ the required P values turned out to be quite small. With decrease of α, however, the required pressure rises. These design data agree quite well with the experimental data determined at deployment of the full-scale model of the tank, made from steel St3, the mechanical properties of which are quite close to those accepted in the calculation.

Figure 8, *a* shows the distribution of residual stresses σ_{ss} on the inner and outer surfaces of the shell under the conditions of a rigid fastening on the edge ($s = 0$). The Figure shows that these conditions are

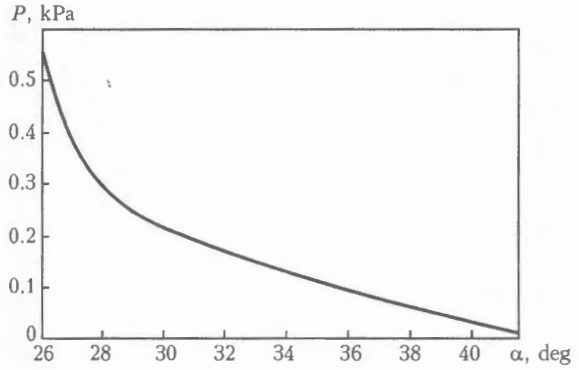

Figure 7. Change of pressure P required for tank deployment, depending on the angle of conicity α

effective in a small region near the edge $s = 0$. In the rest of the shell stresses σ_{ss} change practically in keeping with the geometry of corrugation location. Maximum values of residual stresses σ_{ss} do not exceed 100 MPa. Calculation of distribution of residual stresses on the shell inner and outer surfaces (Figure 8, *b*) showed that these stresses also vary in accordance with the corrugation location on the shell, but more smoothly than σ_{ss}. Level of $\sigma_{\beta\beta}$ does not exceed 150 MPa. Here, local stress peaks near the edge ($s = 0$) characteristic for σ_{ss} are absent.

It should be noted that the residual stress level after deployment of the tank is quite low, so that loading of the already deployed structure by internal pressure $P \approx 0.1$ MPa (which is almost 2 times higher than the maximum operating pressure) proceeds in the elastic deformation region (Figure 9).

This phenomenon is related to deep unloading of the tank at the final deployment stage. This stage is preceded by a quite intensive plastic flow with formation of «plastic hinges» in the zone of the straightening corrugations (Figure 10). This leads to an essential reduction of bending deformation resistance, while the impact of a relatively low internal pressure at deployment is noticeably higher than the deformation resistance. A jump-like straightening of the tank wall and subsequent relaxation of stresses from those given in Figure 10 to residual stresses take place (see Figure 9).

Ring cross-section was calculated (see nodes *A* and *E* in Figure 3), allowing for the resistance to loss of stability at tank deployment by internal pressure and subsequent loading by operating load (hydrostatic pressure). As the ring (nodes *A* and *B* in Figure 3) is welded to the tank shell, the probability was considered of the loss of stability of the respective ring section of the tank, consisting of the ring and the shell elements connected to it.

Such a schematic features a certain conservatism, as the shell has a higher rigidity, both due to curvature in the circular direction and along the corrugation generatrix, and design of nodes *A* and *E*. The length of the adjoined elements was selected as the «final effect» zone for the conical shell [3].

Calculation showed that at maximum deployment pressure of 0.1 MPa no loss of stability for nodes *A*

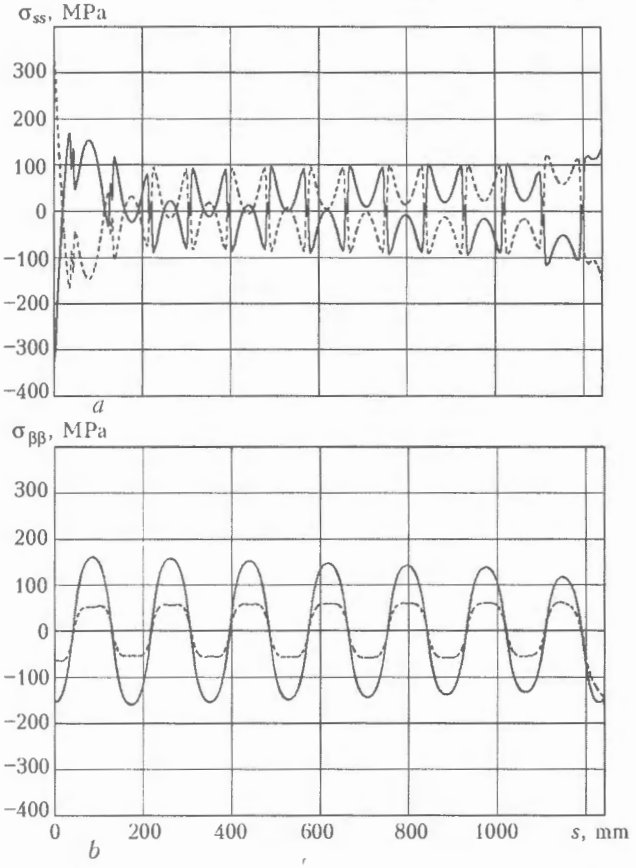

Figure 8. Distribution of residual stresses σ_{ss} (*a*) and $\sigma_{\beta\beta}$ (*b*) on the inner (solid curves) and outer (dashed) surfaces of the tank wall under the conditions of rigid restraint on the edge ($s = 0$)

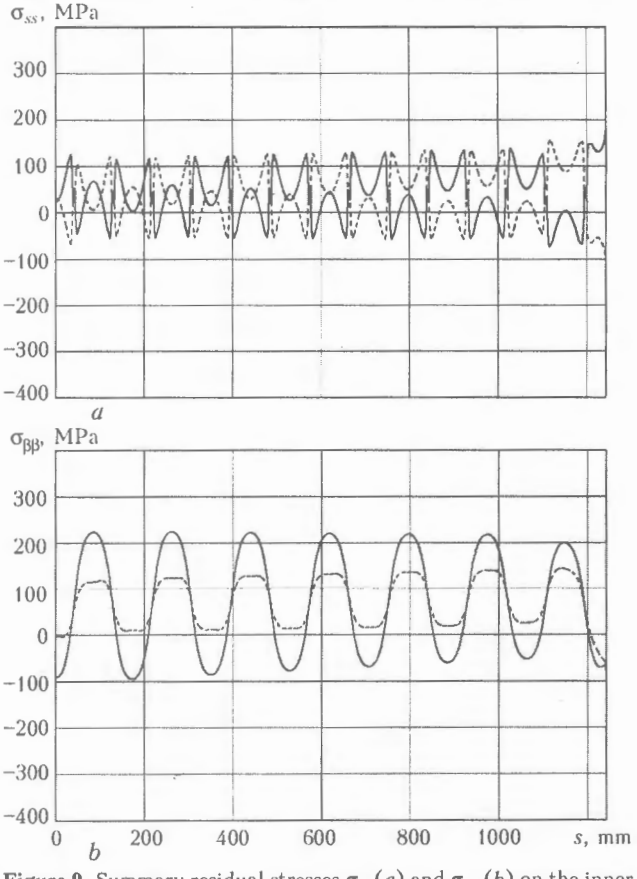

Figure 9. Summary residual stresses σ_{ss} (*a*) and $\sigma_{\beta\beta}$ (*b*) on the inner (solid curves) and outer (dashed) surfaces of the tank wall after its deployment and loading by internal pressure $P = 0.1$ MPa

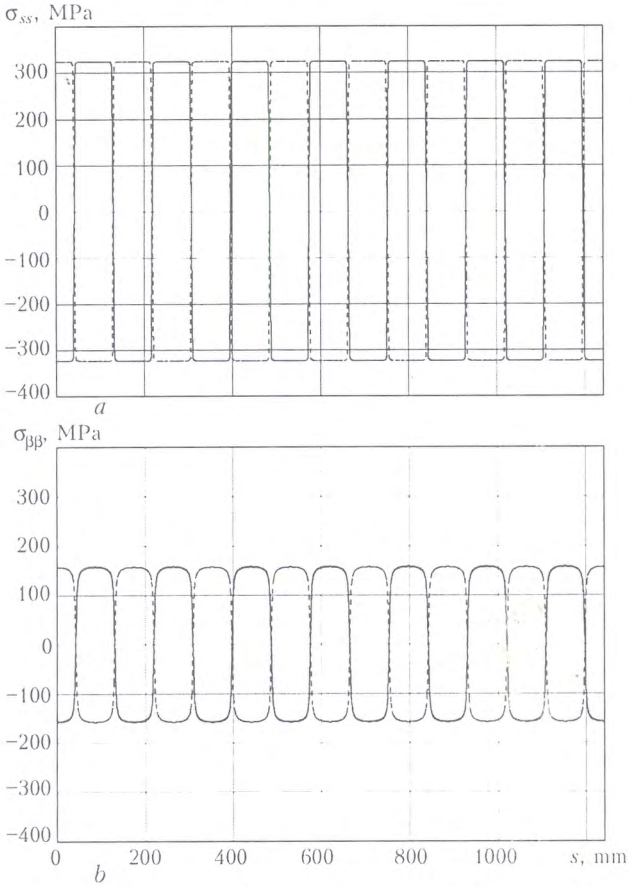

Figure 10. Distribution of residual stresses σ_{ss} (*a*) and $\sigma_{\beta\beta}$ (*b*) on the inner (solid curves) and outer (dashed) surfaces of the tank wall in the initial period of its deployment

and *E* of the considered dimensions takes place, which is confirmed experimentally.

At operating loading by hydrostatic pressure the compressive loads in regions *A* and *E* during tank filling are lower than at deployment ($P < 0.05$ MPa), so that it may be assumed that stability of nodes *A* and *B* of the above dimensions is ensured.

Tank deployment is accompanied by considerable local plastic deformations, leading to formation of a residual stressed state, in which the operating internal pressure right up to 0.1 MPa creates only an elastic loading of the tank wall; ring sections (nodes *A* and *E* in Figure 3) are sufficient in terms of resistance to loss of stability at tank deployment.

Calculation of stresses developing in the tank under the impact of its own weight and hydrostatic pressure of the poured-in liquid has been performed. For this purpose the ring section was calculated (see Figure 2) at maximum filling of the tank that showed that ring section of 100 × 10 mm is the most favourable in terms of the structure stressed-strained state. The level of maximum stresses in the local zone adjacent to the ring does not exceed 175 MPa on the shell and 140 MPa on the bottom, which is admissible for austenitic steel with σ_y = 280 MPa.

Stressed state of node *D* (see Figure 3) was determined for the above specified section of the ring during tank deployment at the final stage of loading by maximum pressure $P \approx 0.1$ MPa. It was established that at deployment in the region of node *D* with the ring of section 100 × 10 mm the shell develops a local zone of plastic deformations from wall bending directly at the ring. The plastic deformation zone spreads to a distance of about 200 mm from node *D*, and the ring operates in the elastic stress region. Small values of plastic deformations on surface *ED* and bottom *DF* at deployment (P = 0.1 MPa) correspond to a low level of residual stresses after pressure relief. Calculation showed that summing up of the above stress fields with the stresses corresponding to tank loading by the maximum operating load, does not lead to any significant changes of the shell stressed state.

Thus, design of node *D* with a ring of 100 × 10 mm cross-section ensures the performance of this node both at deployment and at its loading by a maximum working load (complete filling with water).

Performed calculation of the influence of wind load (wind velocity of 50 m/s) on the structure showed that the level of normal and tangential stresses induced by the wind impact is not more than 8 MPa in the entire shell. Level of circumferential stresses is not higher than 20 MPa, being an order of magnitude lower than those induced by hydrostatic pressure. Thus, it may be assumed that maximum stresses may rise by not more than 10 MPa above the mentioned load.

The welds were made by automatic non-consumable electrode argon-arc welding. Special attention was given to butt welded joints when making conical billets. It is established that the welds are subjected to bending deformations at the shell forming, so that the quality of the manufacturing should be high. Selection and optimization of the welding modes was performed in keeping with the following requirements: full penetration single-pass welding; weld reinforcement of not more than 0.5 mm; application of Sv-06Kh19N9T filler wire with a higher (19 wt.%) chromium content, this compensating its burning losses in the weld metal and preserving the anticorrosion properties of the latter on the level of those of the base metal.

Verification of various welding modes on joint simulation samples resulted in selection of the follow-

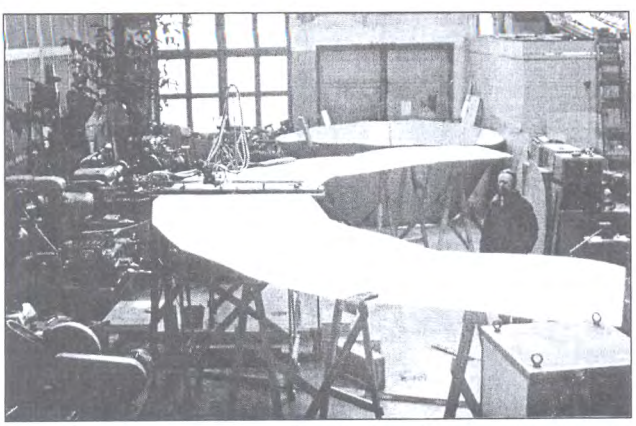

Figure 11. General view of a flat blank of the conical shell in the berth

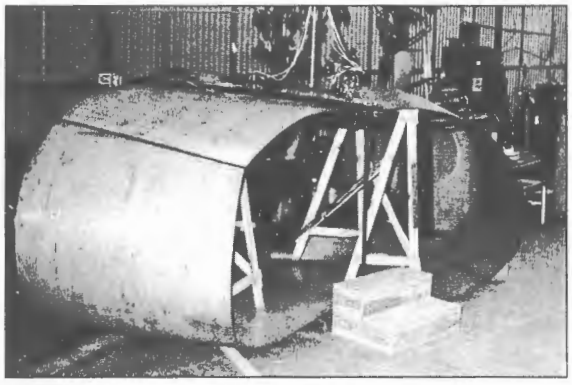

Figure 12. Closing butt of the weld of a conical shell assembled for welding in the berth

Figure 13. General view of the welded conical shell before corrugation formation

ing mode parameters: welding current I_w = 175 A; arc voltage U_a = 10 V; welding speed v_w = 11 m/h; wire feed rate v_f = 24 m/h; welding wire diameter of 1 mm.

Conically-shaped shells which were part of the tank, were made in the form of a development of six sectors, with their subsequent folding into a cone and welding up of the closing butt joint. Assembly and welding were conducted in a specialized berth, which provided a high accuracy of positioning of the assembled butt relative to the welding head. Welding process and general view of the flat blank for making the conical shell are given in Figure 11. The most critical welding operation is filling the closing butt joint (Figure 12), that largely determines the accuracy of the geometry of the conical billet as a whole and may essentially influence the characteristics of the product at corrugation formation. It should be noted that all the butt joints (except for the closing joint) of the flat blank are made under the conditions of a free development of shrinkage shortening of the welds at cooling, which was ensured by the conditions of assembly of the panel in the berth. On the other hand, the closing butt joint was made under the conditions of the stressed state due to bending displacements of the edges being welded, and this required particular accuracy in the joint assembly. General view of the conical shell after making all the welds is given in Figure 13.

Corrosion resistance of welded joints was determined on samples by a standard procedure of accelerated testing by boiling in a solution of sulphuric acid for 24 h. Testing was conducted in two stages: in the first stage undeformed samples of 80 × 20 mm size were used, and in the second stage — samples bent through 90° angle for plastic deformation of the weld metal in the HAZ. No traces of corrosion damage were found during testing.

An important stage in the tank fabrication is the process of transforming the shape of the conical shell into a corrugated disc. An ingenious method was developed of forming flat discs with circular corrugations, based on the rotary forming of closed thin-walled conical shells of revolution (Figure 14). With this purpose local forming forces were applied to the rotating billet. Backup was created by circular fins of the mould, which are the protrusions made in the massive matrix mounted on the faceplate of the rotary-table lathe with a pitch equal to that of the disc corrugations. The force required to form the corrugations was created by a special tool in the form of a roller, mounted in the cutter-holder of the carriage and moving along the billet axis of revolution. After forming of the circular disc the height of the conical shell was reduced 15 times, so that it equaled the height of the corrugations.

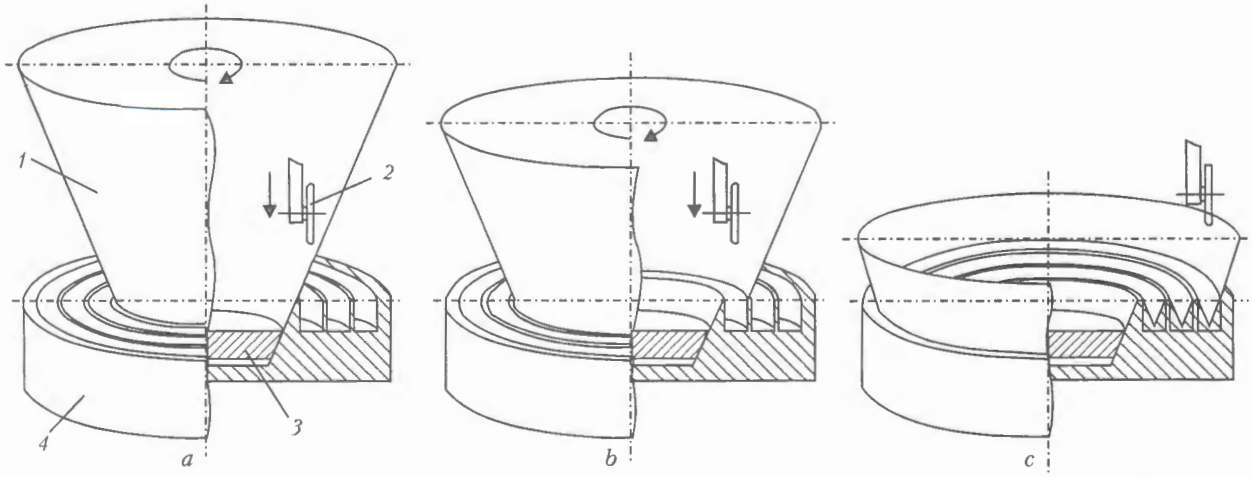

Figure 14. Schematic of transformation of a conical shell into a corrugated disc at the initial (*a*), intermediate (*b*) and final (*c*) stages: *1* — conical billet; *2* — forming roller; *3* — clamp for fastening the blank in the mould; *4* — mould-matrix

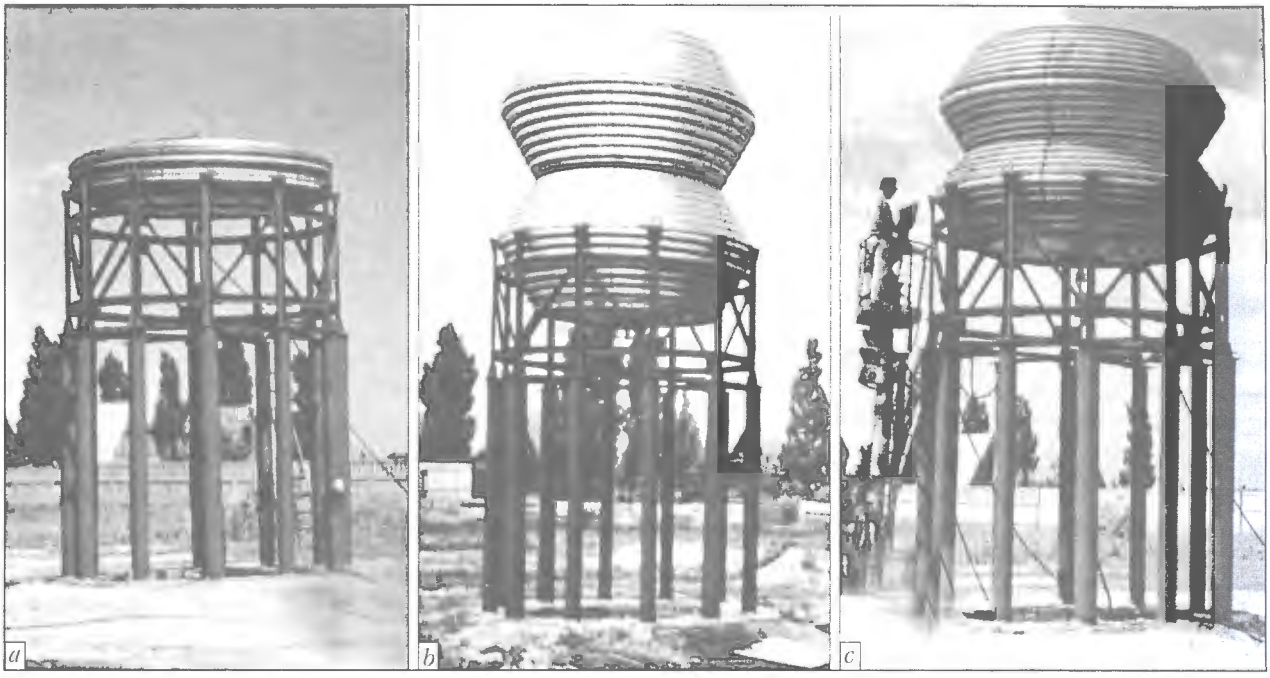

Figure 15. View of a large-sized welded structure of a transformable volume before (*a*) and during (*b*) deployment and after full deployment (*c*)

The developed method ensures sound production of circumferential corrugations and may be implemented in the metal fabrication plants with application of simple deforming rigging and assembly devices.

The produced flat discs with circular corrugations were used as base elements to develop structures of a transformable volume. A set of basic elements of 4 pcs was made, then subassembly and welding of the elements into one structure were performed. Site welded joints of the shell were tested for tightness. With this purpose the corrugated pack was loaded by excess internal pressure ($P = 0.03$ MPa). Check examination did not reveal any leaks or other defects in the produced joints.

The site for tank mounting was selected in Lazurnoe township of Kherson district. The dry climate of this region and permanent water deficit implied intensive use of the tank. Supporting platform 4.5 m high was first built in the construction site.

The structure was transported to the site by motor transport. Preparation to the tank deployment into the working position consisted in sealing the hatch and all the technological unions with connection of the compressed air feed. The tank prepared for deployment is shown in Figure 15, *a*. Pressure inside the structure was increased using a mobile diesel-compressor. The first motion was observed already at the pressure of 0.04–0.05 MPa. Deployment proceeded successively – corrugation after corrugation, starting with the first one of 3760 mm diameter, and was accompanied by soft popping sounds. Pressure dropped abruptly due to increase of the tank inner volume. Corrugations of 1710 mm diameter were the last to transform at the pressure of 0.1 MPa.

The process of tank deployment is shown in Figure 15, *b, c*. The height of the tank deployed up to the working condition, practically coincided with the design value. After hydraulic testing the tank of the transformable volume was put into operation as a water tower.

Experience gained in fabrication of transformable shells, demonstrated the broad capabilities of their application in welded structures for storage of liquid and loose products.

1. (2000) *Space: technologies, materials science, structures.* Ed. by B.E. Paton. Coll. Kiev: PWI.
2. Makhnenko, V.I., Velikoivanenko, E.A. (1982) Calculation of stresses and strains in thin-walled shell with circumferential welds. *Avtomatich. Svarka*, **3**, 1–8.
3. (1968) *Strength, stability, vibrations.* Ed. by I.A. Birger, Ya.G. Panovko. Vol. 1. Moscow: Mashinostroenie.
4. Makhnenko, V.I. (1976) *Computational methods of investigation of welding stress and strain kinetics.* Kiev: Naukova Dumka.

NUMERICAL MODELLING OF ABSORPTION OF GASES BY DEPOSITED METAL IN WET UNDERWATER WELDING

O.M. PORTNOV and **S.Yu. MAKSIMOV**
E.O. Paton Electric Welding Institute, NASU, Kiev, Ukraine

Results of mathematical modelling of composition of atmosphere of a vapour-gas bubble and content of hydrogen and oxygen in the weld metal as a function of slag in wet underwater welding are given. The mathematical model is based on calculation of thermodynamic equilibrium in an isolated three-phase gas–slag–metal system. It is shown that atmosphere of the vapour-gas channel in a temperature range of 2000–2500 K consists of a water vapour and molecular hydrogen.

Keywords: *underwater arc welding, vapour-gas bubble, isobaric-isothermal potential, gas–slag–metal system, hydrogen, oxygen, water vapour, basicity of slag*

The arc in underwater welding is ignited in the atmosphere of a water vapour formed due to heating of water at short-circuiting of electrodes. It functions in a vapour-gas bubble, the composition and temperature of which determine the gas content of the weld metal. The atmosphere of the bubble is a product of interaction of water vapour with liquid metal and slag melt. As the water vapour consists of 11.11 % H_2 and 88.89 % CO_2, it is just natural to expect that it is these gases that make up the base of the atmosphere of the vapour-gas bubble. However, analysis of its atmosphere and effluent gases shows that the dominant gas in this case is hydrogen, and that there is almost no oxygen [1–3].

The purpose of this study was to evaluate composition of the atmosphere of the vapour-gas bubble and effect of basicity of slag on residual gas content of the deposited metal through calculation of thermodynamic equilibrium of the gas–slag–metal system.

Figure 1 shows schematic of the wet underwater welding process. Assume that atmosphere of the vapour-gas bubble consists of a water vapour and its dissociation products. Passing through the arc gap, the electrode metal droplets are saturated with gases and get into the weld pool. The molten slag covering the surface of the electrode metal droplets and weld pool is an intermediate phase, which participates in the processes of interaction of the gas phase with metal. The slag melt itself can absorb and dissolve gaseous components of the bubble atmosphere, and exert a substantial impact on their transfer to the metal surface. It is very difficult to study the processes of interaction within the gas–slag–metal system, as the absorption of gases is simultaneously affected by many parameters of the welding process, and it is not always possible to control this effect. In this situation, application of the mathematical modelling methods simplifies selection of an optimal composition of the slag phase. In addition, the calculation results allow evaluation of the effect of each parameter of the welding process taken separately.

Mathematical model. Thermodynamic analysis was conducted to predict results of the interaction processes in the gas–slag–metal system by the calculation method [4] using procedure described in [5]. The used mathematical model was based on finding thermodynamic equilibrium of the system corresponding to a minimum of the total isobaric-isothermal potential (Gibbs energy). The gas phase in the analysis was assumed to be a mixture of ideal gases, and the slag and metal melts were assumed to be ideal solutions.

The major volume fraction of gases gets into metal when it is in the molten state [6]. The physical model of absorption of gases by metals is described in detail in studies [7, 8]. At the absence of defects in metal, gases are dissolved in it in the atomic state. The main source of atomic hydrogen and oxygen getting into the layer near the metal surface is dissociation of water molecules in the arc atmosphere. If the rate of chemical reactions in the atmosphere is sufficiently high, their components are in a state of equilibrium.

Water molecules are known to be characterised by high stability in heating. And only at a temperature

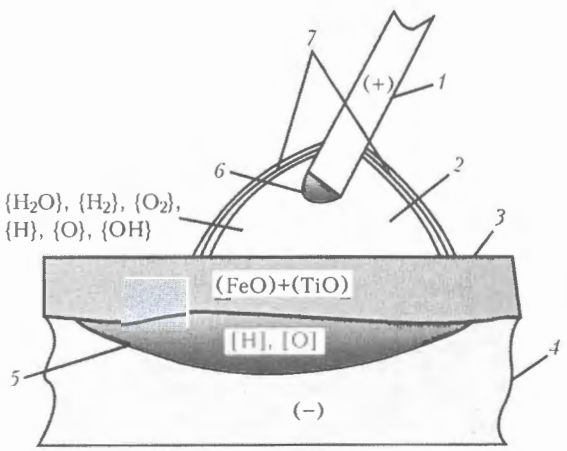

Figure 1. Schematic of wet underwater welding: *1* — electrode; *2* — vapour-gas bubble; *3* — slag; *4* — base metal; *5* — deposited metal; *6* — droplet; *7* — arc

above 1000 °C the water vapour starts dissociating into hydrogen and oxygen to absorb heat:

$$2H_2O \leftrightarrow 2H_2 + O_2 - 136.8 \text{ kcal}. \quad (1)$$

Of practical interest are the factors that determine completeness of reaction (1) and final composition of the gas phase. Composition of the atmosphere can be qualitatively evaluated on the basis of a principle of shift of equilibrium in a direction opposite to the exerted effect. Thus, increase in temperature with distance to the arc column causes an additional endothermic reaction and shift of equilibrium towards composition of the bubble atmosphere, which is rich in hydrogen and oxygen. Increase in hydrostatic pressure at a constant temperature is inevitably accompanied by increase in the quantity of gas particles in unit volume, and leads to a change in the direction of reaction (1) to the opposite one. Therefore, increase in pressure levels to a certain extent the effect of temperature. Let us evaluate the extent of the effect exerted by pressure on the degree of dissociation α of the water vapour. For this, in the expression of constant of equilibrium of reaction (1)

$$K_{eq} = \frac{P^2_{H_2O}}{P^2_{H_2} P_{O_2}} \quad (2)$$

replace partial pressures P_i by the number of moles of reacting components, n_i, total number of moles, N, and total pressure P:

$$P_i = \frac{n_i}{N} P.$$

The calculation per mole of reacting H_2O, allowing for the stoichiometric coefficients of the reaction equation, yields $(1 - \alpha)$ moles of H_2O, 0.5α moles of O_2, and α moles of H_2. Find by summing up the number of formed moles $N = 1 + 0.5\alpha$. Expressing the partial pressure of the reaction components in terms of the quantity of moles and substituting their values in expression (2) yield the quantitative expression of functional relationship of the equilibrium composition of the gas phase and total pressure

$$K_{eq} = \frac{(1-\alpha)^2(1+0.5\alpha)}{0.5\alpha^3 P} = \frac{(1-\alpha)^2(2+\alpha)}{\alpha^3 P}. \quad (3)$$

The degree of dissociation and, therefore, the composition of the equilibrium gas phase can be determined by solving the equation at assigned values of temperature, pressure and equilibrium constant. Thermal dissociation of the water vapour, as noted above, has a low value in a range of comparatively low temperatures (up to 2000 K). Therefore, at some approximation its value in the numerator of expression (3) can be neglected, compared with integer numbers. Then

$$K_{eq} \approx \frac{2}{\alpha^3 P},$$

i.e. the value of the dissociation degree varies, depending upon the pressure in the gas phase, in proportion to its cubic root. In other words, in this temperature range the pressure exerts a relatively low effect on the degree of dissociation of the water vapour and variation in composition of the equilibrium gas phase.

The above calculations allowed numerical investigations to be limited just to a fixed value of pressure. The set initial parameters included temperature of 2000–2500 K, pressure of $1 \cdot 10^5$ Pa, water vapour as initial composition of the gas phase, pure molten iron as the metal phase, and mixture of FeO and TiO_2 as the slag phase. The FeO:TiO_2 ratio was varied from 0.2 to 0.8 in order to vary basicity of the slag.

The total Gibbs energy of the system was equal to a sum of the Gibbs energy of each phase:

$$G = G^{gas} + G^{sl} + G^{met},$$

where G^{gas}, G^{sl} and G^{met} are the Gibbs energies of the gas, slag and metal phases, respectively.

The total Gibbs energy of each phase is equal to a sum of the Gibbs energies of each component of a phase. The Gibbs energy of the i-th component of the gas phase is

$$G_i^{gas} = \left(G_i^0 + RT \ln \left(\frac{P_i}{P_0} \right) \right) M_i,$$

where G_i^0 is the standard value of the Gibbs energy of the i-th component of the gas phase; P_0 is the standard pressure (normally, $1 \cdot 10^5$ Pa); M_i is the quantity of moles of the i-th component of the gas phase; T is the temperature; and R is the universal gas constant.

If we assume that the slag and metal phases are ideal solutions, the expressions derived for the Gibbs energy of components of the condensed phases will have the following form:

$$G_j^{sl} = \left(G_j^0 + RT \ln \left(\frac{M_j}{M_{sl}} \right) \right) M_j,$$

where G_j^0 is the standard value of the Gibbs energy of the j-th component of the slag phase; M_j is the quantity of moles of the j-th component of the slag phase; and M_{sl} is the quantity of moles of all components of the slag phase;

$$G_k^{met} = \left(G_k^0 + RT \ln \left(\frac{M_k}{M_{met}} \right) \right) M_k,$$

where G_k^0 is the standard value of the Gibbs energy of the k-th component of the metal phase; M_k is the quantity of moles of the k-th component of the metal phase; and M_{met} is the quantity of moles of all components of the metal phase.

However, as the tables of thermodynamic values for individual materials contain, as a rule, values for the reduced isobaric-isothermal potential per mole of material

$$F^0 = S^0 - \frac{H^0 - H_0^0}{T},$$

where S^0 is the reduced entropy; $H^0 - H_0^0$ is the standard variation in enthalpy (H_0 is the specific enthalpy, and H_0^0 is the specific standard enthalpy), it is necessary to find extremum of the reduced isobaric-isothermal potential G^* taken with an opposite sign:

$$G^* = -\frac{G}{T}.$$

The following dependence exists between G^* and F:

$$G^* = F - \frac{\Delta H_{f,0}^0}{T},$$

where F is the isobaric-isothermal potential; and $\Delta H_{f,0}^0$ is the standard enthalpy of formation of a joint.

The general expression for the reduced isobaric-isothermal potential looks as follows:

$$G^* = \sum_{i=1}^{n_g} \left[G_i^{*0} + RT \ln \left(\frac{P_i}{P_0} \right) \right] M_i + \sum_{j=1}^{n_{sl}} \left[G_i^{*0} + RT \ln \left(\frac{M_i}{M_{sl}} \right) \right] M_j + \sum_{k=1}^{n_{met}} \left[G_k^{*0} + RT \ln \left(\frac{M_k}{M_{met}} \right) \right] M_k, \quad (4)$$

where n_g, n_{sl} and m_{met} are the quantities of components of the gas, slag and metal phases, respectively; G_i^{*0}, G_j^{*0} and G_k^{*0} are the specific reduced isobaric-isothermal potentials of one mole of the i-th, j-th and k-th material, respectively.

When finding extremum G^*, it is necessary to take into account that the following conditions should also be met for the given thermodynamic system:

- gas state equation for the gas phase

$$PV = RT \sum_{i=1}^{n_g} M_i; \quad (5)$$

solution state equation for the slag and metal phases, allowing for their liquid states

$$\sum_{j=1}^{n_{sl}} M_j = M_{sl}; \quad (6)$$

$$\sum_{k=1}^{n_{met}} M_k = M_{met}; \quad (7)$$

mass of each element being retained in the system

$$[El]_q = \sum_{i=1}^{n_g} n_{qi} M_i + \sum_{j=1}^{n_{sl}} n_{qj} M_j + \sum_{k=1}^{n_{met}} n_{qk} M_k, \quad (8)$$

where $q = 1, \ldots, N$; $[EJ]_q$ is the quantity of moles of the q-th element in the system; n_{qi}, n_{qj} and n_{qk} are the stoichiometric coefficients, i.e. the number of atoms contained in a molecule; and N is the number of elements in the system.

Therefore, finding the equilibrium state of the system is reduced to finding an extremum of function (4) by meeting conditions (5) to (8), i.e. finding a conditional extremum. One of the general methods of finding the conditional extremum is the Lagrange method, according to which the conditional extremum of function $G^*(x_1, x_2, x_n)$ corresponds to an unconditional extremum of auxiliary Lagrange function:

$$L(x_1, x_2, \ldots, x_n, \lambda_1, \lambda_2, \lambda_m) = G^*(x_1, x_2, \ldots, x_n) + \sum_m \lambda_m \varphi(x_1, x_2, \ldots, x_n). \quad (9)$$

Here x_1, x_2 and x_n are the problem variables, determining function (4); $G^*(x_1, x_2, \ldots, x_n)$ and $\varphi(x_1, x_2, \ldots, x_n)$ are the equations of relationship (5) to (8); and λ_m are the undetermined Lagrange multipliers. The extremum condition of the Lagrange function is the equality of all its particular derivatives of all variables to zero. By differentiating expression (9) with respect to all variables, we obtain the system consisting of $n_g + n_{sl} + n_{met} + N + 3$ equations, which, when solved, can be used to determine the content of elements in corresponding phases.

Results and discussions. The calculations made allow evaluation of composition of the atmosphere of the vapour-gas bubble, and effect on it by the proportion of the slag components and content of gases dissolved in metal. At a constant temperature (2000 K) the major components of the atmosphere of the vapour-gas bubble are known to be a water vapour and molecular hydrogen, the content of atomic and molecular oxygen in the atmosphere of the vapour-gas bubble being not in excess of ten thousandths of percent (Figures 2 and 3). Increase in the FeO:TiO ratio in slag, i.e. its basicity, from 0.2 to 0.8 leads to increase in the water vapour content from 60 to 85 % due to decrease in the molecular hydrogen content from 40 to 15 %, the oxygen content in this case changing several times. It is shown in study [9] that the content of gases in metal is determined by the degree of their dissociation in the sub-surface Knudsen layer. Therefore, variations in the content of atomic gases in the atmosphere of the vapour-gas bubble and in metal are of a similar character (Figures 3–5). The trend of variations in the measured content of hydrogen (Figure 4) in all the cases is similar to the calculated one. However, it differs in values. This is attributable to the presence of desorption of gas from metal occurring in cooling, as well as to a more complex composition of the slag phase in actual electrode materials. Figure 5

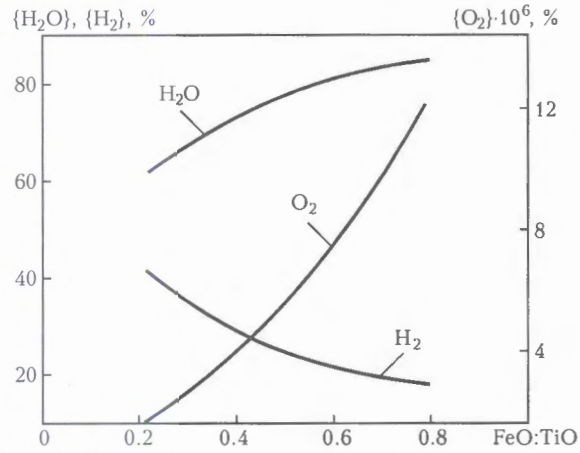

Figure 2. Effect of slag composition on partial pressure of molecular gases $\{H_2O\}$, $\{H_2\}$ and $\{O_2\}$ in atmosphere of the vapour-gas bubble at 2000 K

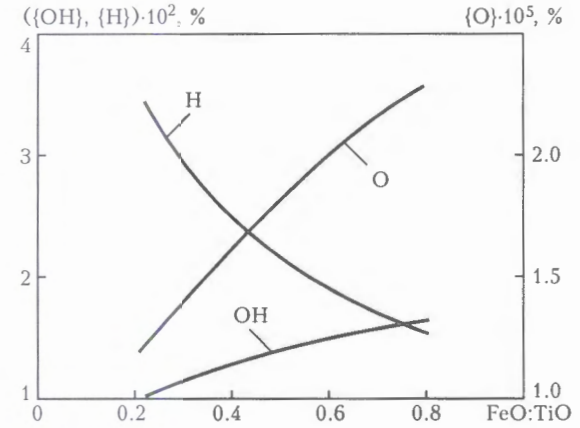

Figure 3. Effect of slag composition on the content of hydroxyl, as well as atomic hydrogen and oxygen in atmosphere of the vapour-gas bubble

shows variations in the content of oxygen in the deposited metal (experimental and calculated data) depending upon the slag composition. It can be seen

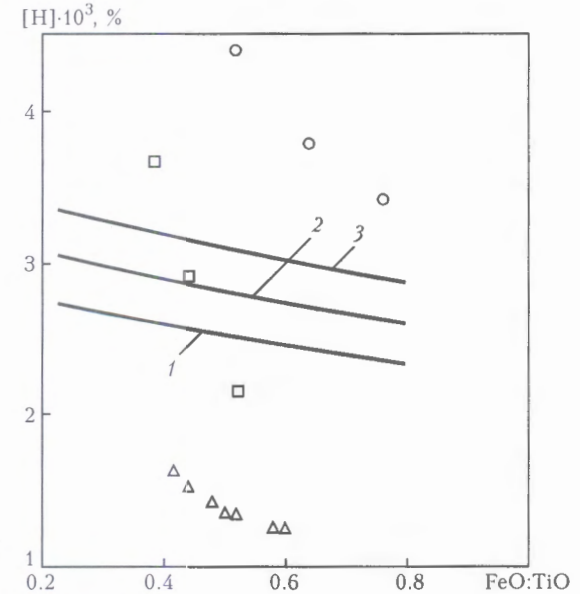

Figure 4. Effect of slag composition on the concentration of hydrogen dissolved in the weld metal at a temperature of 2000 (*1*), 2100 (*2*) and 2200 (*3*) K: Δ, ○, □ – experimental data taken from studies [10–12], respectively

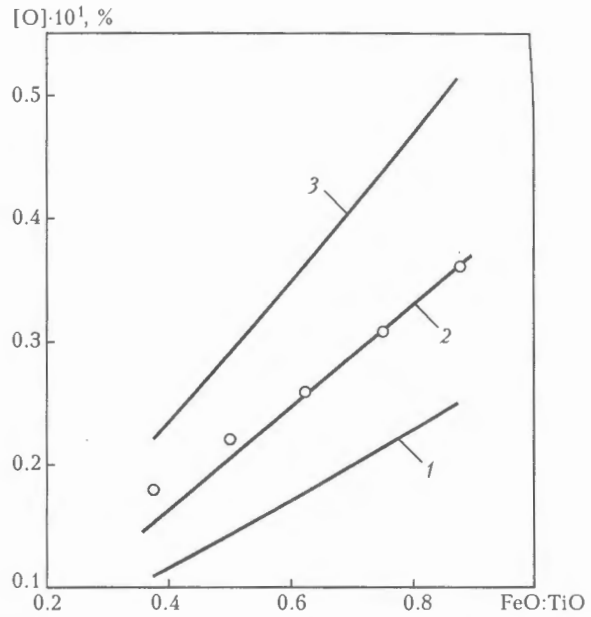

Figure 5. Dependence of the content of oxygen dissolved in the weld metal upon the temperature in the gas–slag–metal system: *1–3* – see Figure 4; ○ – experimental data

from the Figure that the best agreement of the experimental and calculated data for oxygen takes place at a metal temperature of 2100 K.

It is of interest to trace the effect of temperature of the metal surface and, hence, the entire gas–slag–metal system on the composition of the gas phase and content of gases dissolved in metal. As shown by the results obtained (Figure 6), the degree of dissociation of water increases with increase in temperature (Figure 6, *a*). This causes a corresponding increase in pressure of the molecular and atomic components of oxygen and hydrogen (Figure 6, *b*). Although increase in the concentration of water vapour dissociation products turned out to be comparatively low, such changes in the composition of the vapour-gas bubble atmosphere led to a substantial increase in the degree of saturation of molten metal with dissolved gases (Figure 7). Calculations of temperature dependencies made at the FeO:TiO = 1:1 ratio showed that within the temperature range investigated (2000–2500 K) the content of hydrogen increased from $2.5 \cdot 10^{-3}$ to $4.0 \cdot 10^{-3}$ %, and the content of oxygen – from 0.18 to 0.86 %.

Therefore, the results obtained are indicative of the fact that within the said temperature range the main components of the vapour-gas bubble are molecular hydrogen and water vapour. As the latter is characterised by a considerable oxidising ability, the possibility of occurring the following reaction exists at high temperatures:

$$H_2O + Me \leftrightarrows MeO + H_2. \qquad (10)$$

This allows a conclusion that oxidation of metal in underwater welding occurs mainly through a direct contact with water vapour (10). Hydrogen formed as a result of this reaction is partially dissolved in metal. The presence of deoxidising elements in the weld pool

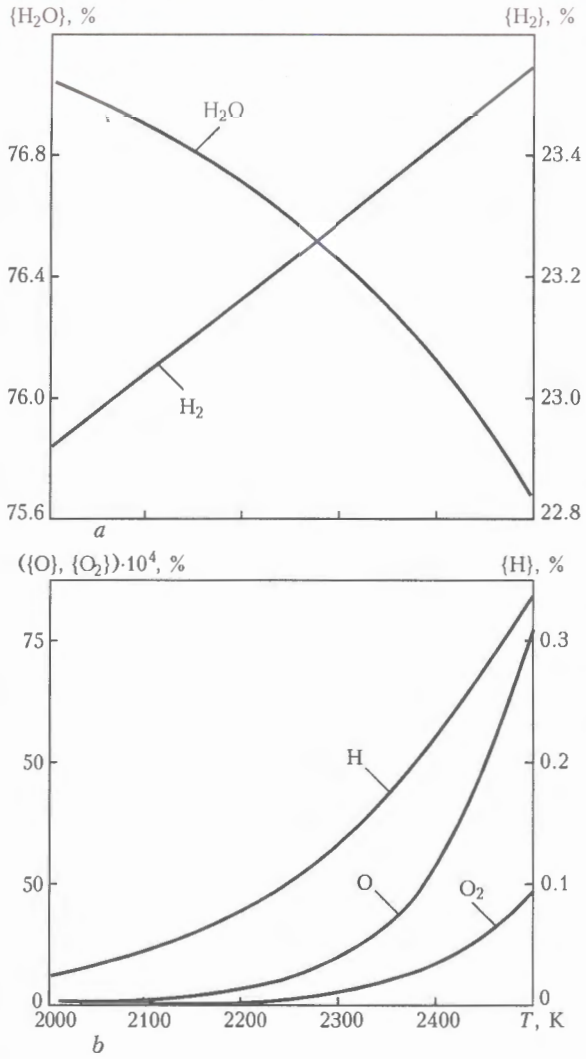

Figure 6. Temperature dependence of the content of water vapour and molecular hydrogen (*a*), as well as atomic and molecular oxygen and atomic hydrogen (*b*)

leads to a more complete accommodation of hydrogen. Because of a high chemical affinity for the slag elements and iron, oxygen is almost completely consumed for their oxidation, and in cooling it becomes chemically combined with metal. Hydrogen enters into chemical reaction less intensively. Therefore, its content is determined in many respects by the temperature dependence of dissociation of water vapour molecules. The oxidising ability of the bubble atmosphere grows with increase in basicity of the slag and temperature, which leads to increase in burning out of alloying elements and saturation of the weld metal with oxygen in the form of non-metallic inclusions.

CONCLUSIONS

1. At a temperature of 2000–2500 K, the vapour-gas bubble consists primarily of a water vapour and molecular hydrogen. Because of high reactivity of oxygen, its content in the vapour-gas bubble atmosphere is negligible.

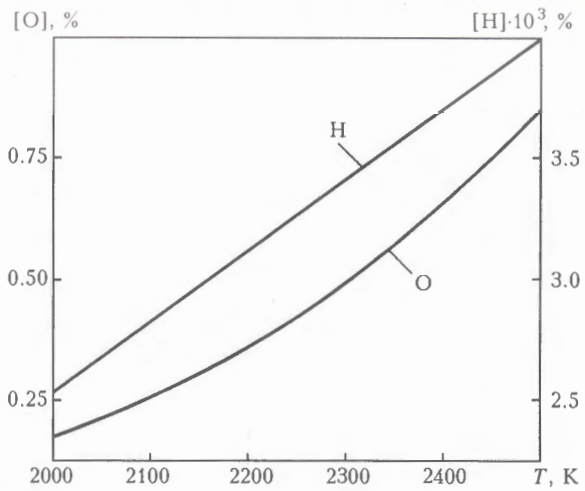

Figure 7. Temperature dependence of the content of gases dissolved in the weld metal

2. Comparison of experimental and calculated data shows that the calculation of thermodynamic equilibrium in the gas–slag–metal system allows evaluation of the effect of slag composition on the content of gases dissolved in the weld metal.

3. The mathematical modelling methods proved the possibility of regulating the content of oxygen and hydrogen in the weld metal through varying basicity of the slag.

4. Variations of the FeO:TiO ratio exert a higher effect on the content of oxygen in the weld metal than on the content of hydrogen.

1. Avilov, T.I. (1958) Study of the underwater arc welding process. *Svarochn. Proizvodstvo*, **5**, 12–14.
2. Madatov, N.M. (1965) Properties of vapour-gas bubble around arc in underwater welding. *Avtomatich. Svarka*, **12**, 25–29.
3. Ando, S., Asahina, T. (1983) A study on the metallurgical properties of steel welds with underwater gravity welding. In: *Proc. of Int. Conf. on Underwater Welding Process* (Trondheim, June 27–28, 1983). Oxford, 255–261.
4. Sinyarev, G.B., Vatolin, N.A., Trusov, B.G. et al. (1982) *Application of computer for thermodynamic calculations of metallurgical processes*. Moscow: Nauka.
5. Pokhodnya, I.K., Tsybulko, I.I., Orlov, L.N. (1993) Influence of slag composition on hydrogen content of molten metal in CO_2 welding. *Avtomatich. Svarka*, **11**, 3–5.
6. Pokhodnya, I.K. (1972) *Gases in welds*. Moscow: Mashinostroenie.
7. Morozov, A.N. (1968) *Hydrogen and nitrogen in steel*. Moscow: Mashinostroenie.
8. Linchevsky, B.V. (1986) *Thermodynamics and kinetics of interaction between gases and liquid metals*. Moscow: Metallurgiya.
9. Pokhodnya, I.K., Shvachko, V.I., Portnov, O.M. (2000) Mathematical modelling of absorption of gases by metal during welding. *The Paton Welding J.*, **7**, 11–16.
10. Kononenko, V.Ya. (1996) Metallurgical peculiarities of flux-cored wire welding in water environment. *Avtomatich. Svarka*, **9**, 22–26.
11. Surian, E. (1997) ANSI/AWS E7024 SMAW electrodes: the effect of coating magnesium additions. *Welding J.*, **76(10)**, 404–411.
12. Rissone, N., Bott, I., Jorge, J. et al. (1997) ANSI/AWS A5.1–91 E6013 rutile electrodes: the effect of Wollastonite. *Ibid.*, **11**, 498–507.

VARIATIONS IN STRUCTURE AND PROPERTIES OF HAZ METAL IN WELDED JOINTS ON STEEL 30KhGSA IN ARC TREATMENT*

V.M. KULIK and **V.G. VASILIEV**
E.O. Paton Electric Welding Institute, NASU, Kiev, Ukraine

Austenitic transformation of the HAZ metal in arc welding proceeds at increased temperature. Repeated austenising in arc treatment of hardened metal in a region of overheated HAZ occurs at an increased temperature, and its rapid heating leads to decrease in size of austenite grain. The hardening structure is restored, and properties similar to the initial ones are acquired in subsequent cooling. Heating of the hardened HAZ metal below A_{c_1} results in short-term tempering, improvement of its impact toughness and cold crack resistance. The highest efficiency of the arc effect is achieved in heating of the HAZ metal within the intercritical temperature range.

Keywords: *arc welding, arc treatment, high-strength steel, heat-affected zone, heating, cooling, thermal cycle, hardening, dilatogram, phase transformations, structure, impact toughness, delayed fracture*

Welded parts of low metal content, characterised by increased performance, are made from hardened high-strength alloyed and carbon steels of small thickness. They are sensitive to cold cracking within the HAZ in a region of a low-ductility metal hardened during welding [1]. General heat treatment of a part or local arc treatment of a welded joint allow improvement of the structure of metal, decrease of its hardness, and increase of toughness and cold crack resistance. The first treatment method is very labour-consuming, requires the use of expensive furnace equipment, and it is not always possible to apply it if a welded part is big in size. The second method is simpler and more cost-effective. However, improvement of mechanical properties of the HAZ metal in short-time low-temperature heating is not necessarily the case. Literature data on variations in the hardened HAZ metal subjected to a short-time thermal effect are scanty.

The purpose of this study was to determine peculiarities of occurrence of phase transformations in the hardened HAZ metal and variations in its structure during arc treatment within the heating temperature range that is realistic for improvement of properties of a welded joint.

The object of investigations was 3.1 mm thick high-strength steel 30KhGSA, having limited weldability, which is considered to be a good candidate for manufacture of welded car cylinders [2], especially after a substantial increase in price of steels and suspension of production of thin-sheet high-strength steels of other grades in Ukraine.

A-TIG welding using activating flux VS-2e and arc treatment were performed using machine ARK-1 and rectifier VSVU-315 [3]. Thermal cycles were recorded using thermocouple VR 20/5 with a diameter of 0.35 mm. Phase and structural transformations occurring in HAZ of welded joints were studied using a fast-response dilatometer on simulation specimens (simulation within expanded ranges of temperature and cooling rate).

The simulation specimens measuring 3 × 8 × × 75 mm with a 0.2 mm diameter chromel-alumel thermocouple welded to them were subjected to rapid one-, two- and four-fold heating with an electric current flow to a temperature of 270–1370 °C at a rate of w_h = 100–260 °C/s, and subsequent cooling at a rate of $w_{6/5}$ = 4–17 °C/s at 600–500 °C. The temperature of one-fold and first heatings (1150–1370 °C) corresponded to the temperature of formation of HAZ in welding, and the temperature of repeated heatings corresponded to the thermal effects on the already formed HAZ regions located at different distances from the heat source in arc treatment. The temperature of structural transformations and proportion of structural components were determined from the dilatometric curves recorded on the temperature–elongation coordinates by the method of segments. Critical points of phase transformation, A_{c_1} and A_{c_3}, were found using the Chevenard dilatometer.

Cold crack resistance of HAZ was evaluated, according to [4], from the time of delayed fracture of a flat specimen with a section of 3 × 15 mm after application of an initial load equal to $\sigma_i = 0.9\sigma_{0.2}$ of base metal.

Macro- and microstructure of the treated specimens was examined, grain size was determined according to GOST 5639–82 (CMEA Standard 1959–79), and impact toughness of specimens with a round notch was evaluated.

Figure 1 shows typical dilatograms of steel 30KhGSA, and Tables 1–3 give generalised data on phase and structural transformations in simulation specimens, as well as properties of the simulated HAZ metal. Table 4 gives data on delayed fracture resis-

*The study was performed with participation by V.A. Krasnoshchekova and V.V. Butsky.

tance of HAZ of the joints after welding and arc treatment.

Critical transformation points A_{c_1} and A_{c_3} in furnace heating of steel 30KhGSA are equal to 735 and 850 °C, respectively, and interval between A_{c_1} and A_{c_3} is 115 °C. Rapid heating at a rate characteristic of welding and arc treatment causes increase in the austenite formation temperature (curve *1'* in Figure 1). A_{c_1} and A_{c_3} increase to 790–845 and 900–945 °C, respectively, and an interval between A_{c_1} and A_{c_3} narrows to 80–110 °C at w_h = 107–230 °C/s. The transformation temperatures grow within the above ranges with increase in the heating rate. Therefore, austenising of the steel welded begins at an increased heating temperature, compared with furnace heating, while increase in the heating rate during welding causes decrease in width of the HAZ region, the metal of which undergoes austenising both because of increase in temperature gradient from the base metal to the weld pool, and because of decrease in the $A_{c_3} - T_S$ range (here T_S is the solidus temperature).

This increase in the phase transformation temperatures is reported in studies [5, 6]. The so called «homogeneous austenite» is formed at a temperature that is 90–100 °C higher than A_{c_3} in steel with 0.37 % C heated at a rate of w_h = 100–300 °C/s [5]. It can be assumed that it is formed in welding of steel 30KhGSA at a temperature of 1000–1050 °C or higher, and that the major part (about 80 %) of the HAZ metal being austenised is subjected to homogenisation. Welding heating of chrome-silicon-manganese steel to 1280–1370 °C causes collective re-crystallisation of austenite

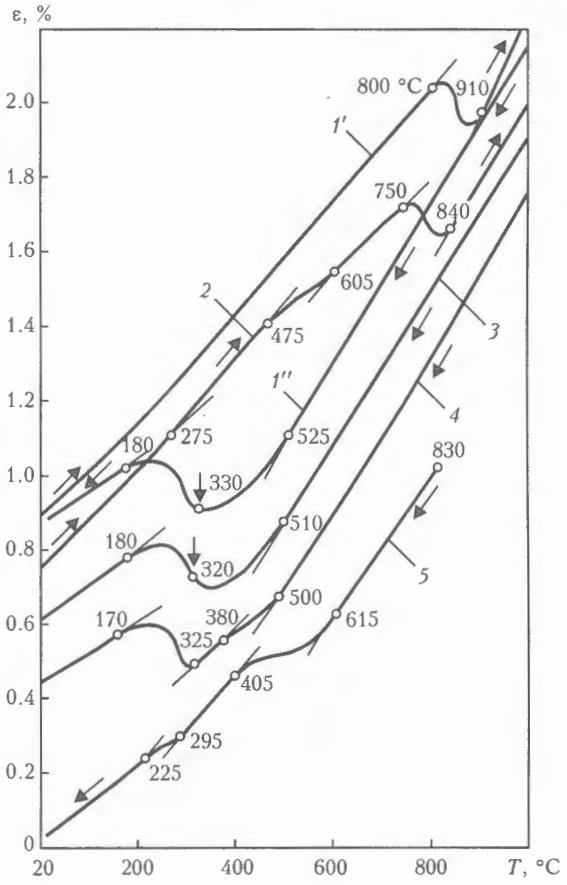

Figure 1. Dilatograms of steel 30KhGSA: *1* — heating to 1350 °C (*1'*) and subsequent cooling (*1''*) (formation of the overheated region in HAZ); *2* — heating to 1350 °C of hardened metal in the overheated region of HAZ; *3–5* — cooling of metal heated to 1350, 1050 and 830 °C, respectively, in the overheated region of HAZ; ε — elongation of specimen; heating and cooling are shown by arrows

Table 1. Effect of temperature of rapid repeated heating above A_{c_3} and cooling rate on structure and properties of repeatedly hardened metal in HAZ of the steel 30KhGSA welded joint

No.	T_h, °C	$T_h - A_{c_3}$, °C	$w_{6/5}$, °C/s	Critical phase transformation points, °C				Structure composition, vol.%		Grain index	*HV*	a_n, J/cm²
				B_s	B_e	M_s	M_e	B	M			
1	1340	490	11	510	325	325	170	55/59	44/41	3–4	509	29.1
2	1250	400	13	515	325	325	170	53/53	47/47	5–6	410	35.7
3	1230	390	9	530	320	320	170	64/37	36/63	4–5	410	29.4
4	1225	380	7	580	405	325	185	41/25	59/75	4–5	443	32.3
5	1225	355	4	605	405	315	190	86/54	14/46	–	354	48.8
6	1145	290	12	530	325	325	170	38/41	62/59	4–5	560	26.8
7	1050	210	12	630	380	325	170	20/54	80/46	5–6	412	32.4
8	980	150	14	490	315	315	170	41/54	59/46	5–6	455	33.2
9	895	75	13	500	320	320	170	33/45	67/55	3–4	507	21.6
10	1150	290	–	600	350	350	225	45/51	55/49	–	–	–
	1150	295	–	620	355	355	220	46	54	–	–	–
	1150	285	–	605	350	350	225	44	56	–	–	–
11	1150	290	–	635	335	335	200	46/71	54/29	–	–	–
	1150	285	–	610	335	335	210	45	55	–	–	–
	1150	295	–	615	340	340	190	45	55	–	–	–

Notes. 1. Temperature of first heating for HAZ formation — 1350 (Nos. 1–10) and 1150 °C (No. 11), w_h = 200 °C/s. 2. Data after first heating of HAZ are given in denominator, and data after subsequent heatings are given in numerator.

Table 2. Effect of heating on phase and structural transformations and properties of repeatedly hardened HAZ metal

T_h, °C	A, vol.%	Critical phase transformation points, °C						Final structure composition, vol.%				*HV*	a_n, J/cm²
		F_s	F_e	B_s	B_e	M_s	M_e	B	M	F_{tr}	F_{tem}		
830	100	–	–	615	405	295	225	~82	~18	0	0	280	43.3
835	35	710	630	490	410	260	< 20	~12	~18	3–5	67–65	331	59.8
810	55	700	650	580	370	170	< 20	45	5	5	45	390	82.2
780	40	750	630	55	360	140	< 20	25	10	5	60	275	85.5

Notes. 1. $w_{6/5}$ = 10–11 °C/s. 2. Initial structure of hardened metal — 46–53 vol.% B and 37–54 vol.% M. 3. A — austenite formed in repeated heating.

and growth of grain to index 3–4. The grain index decreases within the given range with increase in temperature of the heating cycle. The revealed coarse grain is indicative of the fact that these processes occur in welding at temperatures of up to 1250 °C.

In cooling at a rate of $w_{6/5}$ = 7–14 °C/s, the steel heated to 1150–1370 °C undergoes bainitic (at 655–320 °C) and martensitic (at 350–170 °C) transformations (curve *1″* in Figure 1), leading to formation of 40–70 vol.% B and 30–60 vol.% M (Figure 2, *a*) in its structure. Decrease in the heating temperature and cooling rate promotes an early beginning of austenite transformation and decrease in the martensite content.

A similar effect of the cooling rate on the bainitic and martensitic transformation temperatures occurs in welding of high-strength steel 14KhG2SAFD [7]. The largest amount of martensite is formed in the overheated region of HAZ adjoining the weld. High (up to *HV* 520) hardness and coarse grain (index 3–4) of the steel treated following the welding cycle is a cause of low (23.4–28.1 J/cm²) impact toughness of the HAZ metal. The martensite content of metal, critical (50 vol.%) for formation of cold cracks or higher, is formed in the HAZ regions heated to 1330 °C or higher. In the case of heating them to lower temperatures, the martensite content of metal does not reach a critical value. Formation of cold cracks in HAZ of this steel with T_S = 1460 °C is most probable in a region 0.4–0.5 mm wide, adjoining the weld (at a temperature gradient of about 300 °C/mm).

The overheated hardened HAZ metal in rapid heating at a rate of 200 °C has A_{c_1} = 720–760 °C, A_{c_3} = = 820–870 °C, and $A_{c_1} - A_{c_3}$ = 80–100 °C (e.g. curve *2* in Figure 1 with A_{c_1} = 750 and A_{c_3} = 840 °C). Compared with a non-hardened steel, the hardened HAZ metal is characterised by the austenite formation temperatures decreased by 55–105 °C, which are close to the values of temperatures in furnace heating of steel, the austenising temperature range $A_{c_1} - A_{c_3}$ = 80–100 °C remaining almost unchanged. Homogenisation during the first heating of the hardened HAZ metal causes decrease in the «homogeneous austenite» formation temperature during a repeated heating. Increase in the time during which metal remains in the state of homogeneous austenite and a 2–3 times increase in diffusivity of carbon in austenite of the metal experiencing hardening (Figure 3) lead to decrease in chemical heterogeneity and increase in stability of the newly formed austenite. Occurrence of the diffusion processes in rapid heating is evidenced by tempering transformations taking place at 220–360, 435–505 and 580–630 °C, and revealed from the corresponding changes in slopes of the dilatometric curves.

Short-time heating a bit above A_{c_3} is accompanied by restoration of coarse grain of the hardened metal in the overheated region of HAZ. Insignificant decrease in size of the austenite grain from index 3 to index 4 takes place in heating to 895 and 1340 °C (overheating of 150 and 490 °C), whereas a substantial

Table 3. Effect of short-time tempering temperature on properties of overheated hardened steel 30KhGSA

T_h, °C	*HV**	a_n, J/cm²	T_h, °C	*HV**	a_n, J/cm²
–	495	28.1	535	406	37.8
270	416	16.9	625	380	55.8
360	472	44.8	700	258	57.6
410	–	30.0	700**	–	53.2

*Values of hardness are averaged over 6 measurements. **Values of $w_{6/5}$ are reduced 3 times.

Table 4. Thermal effect on HAZ of the joints in chrome-silicon-manganese steel in arc treatment on delayed fracture resistance

Specimen No.	T_h, °C	$w_{6/5}$, °C/s	τ_f, min
1.1	N/D	N/D	40
1.2	830	40	80
1.3	1240	30	270
1.4	1360	60	29
2.1	N/D	N/D	5
2.2	380	Same	1
2.3	840	30	2
2.4	510; 700	N/D	50
2.5	460; 980	N/D; 7	87
2.6	930; 810	4, 5	No fracture

Notes. 1. $w_{6/5}$ = 9–14 and 15–20 °C/s in welding of specimens 1.1–1.4 and 2.1–2.6, respectively. 2. τ_f — time of fracture. 3 – Specimens 2.4 and 2.5 — two-phase effect.

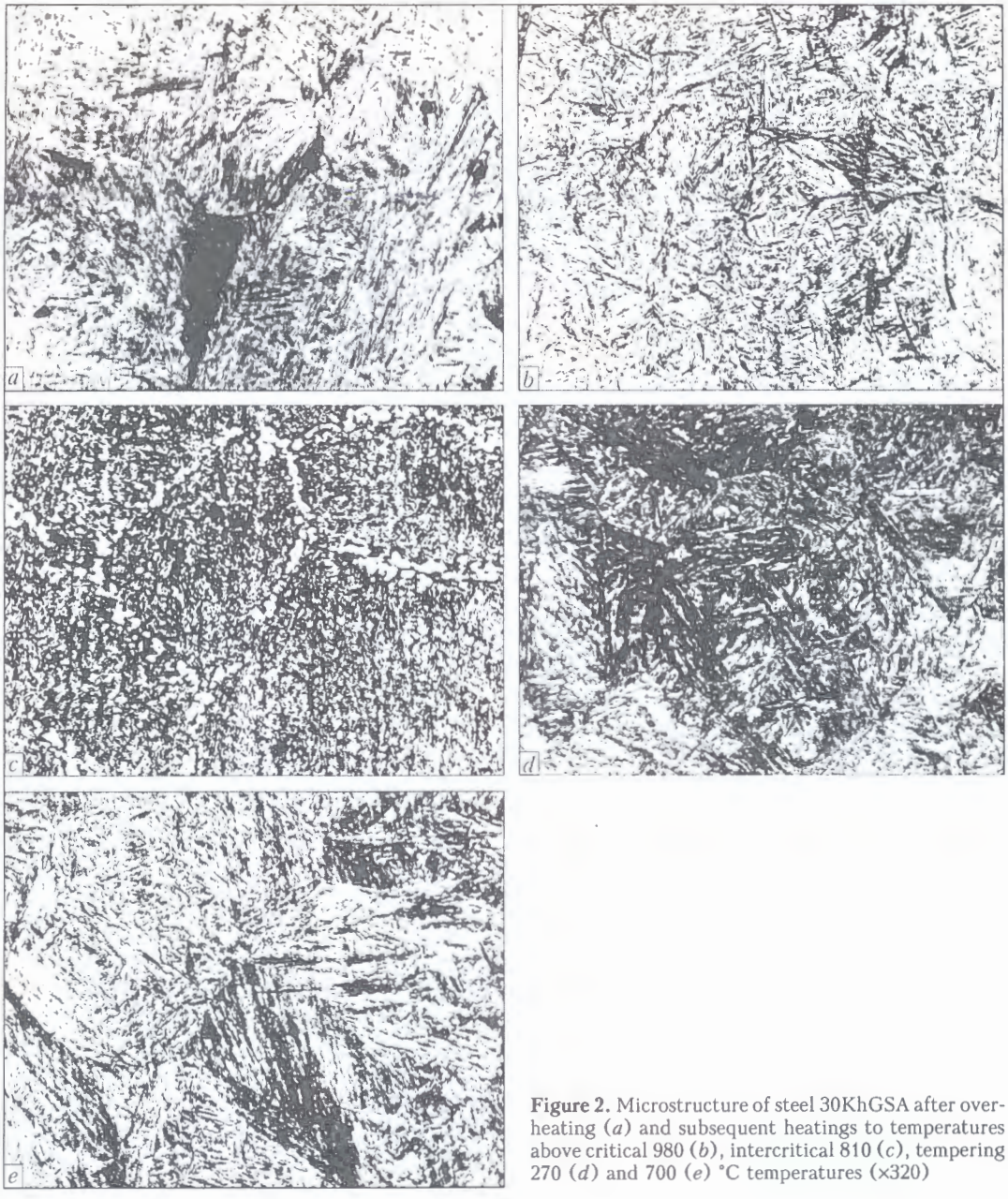

Figure 2. Microstructure of steel 30KhGSA after overheating (*a*) and subsequent heatings to temperatures above critical 980 (*b*), intercritical 810 (*c*), tempering 270 (*d*) and 700 (*e*) °C temperatures (×320)

decrease in grain size to index 5–6 is achieved in heating to 980–1250 °C. The process of subsequent cooling of this metal causes bainitic and martenisitic transformations of austenite (curves *3* and *4* in Figure 1), like in steel not subjected to hardening, with persistence in general of $B_e = M_s = 315–325$ °C, $M_e = 170$ °C, and restoration of the martensitic-bainitic structure. In this case B_s may vary within 490–630 °C, depending upon the heating temperature and cooling rate (see Table 1). Decrease in the latter leads to increase in the austenite transformation temperature, including the temperatures of the end of martensitic transformation.

The identical phase and structural transformations to form approximately equal amounts of martensite and bainite (see Nos. 10 and 11 in Table 1) take place at the identical parameters of heating and cooling of the HAZ metal with different formation temperatures and, accordingly, different proportions of structural components. Repeated heating to 1200 °C or higher, and cooling of steel cause increase in the martensite component content of the HAZ metal structure to 44–80 vol.%, while decrease in the cooling rate results in a substantial decrease in the volume content of martensite, as well as increase in the completeness and time of its self-tempering (see Nos. 2, 3 and 5 in Table 1). The quantity of repeated heatings has hardly any effect on B_s, B_e and M_s, and the contents of the formed martensite and bainite — on M_e of the overheated metal. Increase in the quantity of heatings of the non-overheated HAZ metal is accompanied by decrease in the volume content of M_e.

After repeated heatings to the austenising temperature, persistence of the hardening structure (Figure 2, *b*) and possible increase of the volume content of the martensitic component in it cause growth of metal hardness to *HV* 410–560, while exceeding a critical content of martensite causes deterioration of cold

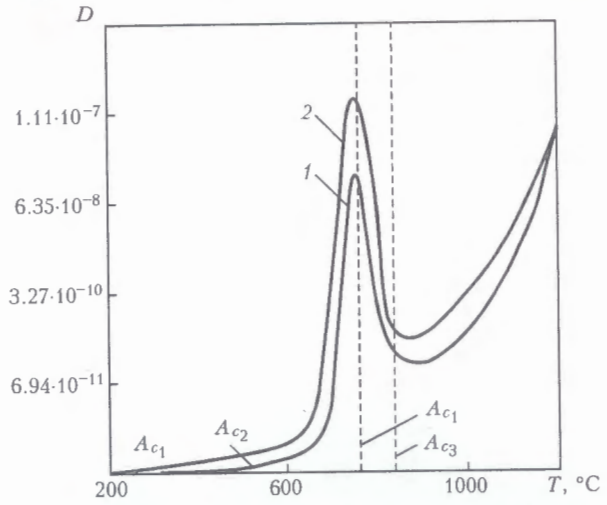

Figure 3. Temperature dependence of diffusion coefficient D of carbon in steel 35KhGSA in the initial state (*1*) and after hardening (*2*) [8]

crack resistance. Refining of the earlier overheated austenite grain to index 5–6 in short-time heating to 980–1250 °C results in an insignificant increase in impact toughness (to 33.2–35.7 J/cm^2). Persistence of the coarse (index 3–4) grain after heating to 895 and 1340 °C with insignificant and high overheating above A_{c_3} (75 and over 400 °C) results in the fact that impact toughness remains low (29.1 and 21.6 J/cm^2). A 3 times decrease in the cooling rate allows an approximately 1.5 times decrease in hardness and approximately 1.7 times increase in impact toughness of the overheated steel.

Rapid heating to the intercritical range temperatures is accompanied by complication of the HAZ metal structure. Heating to these temperatures causes partial $\alpha \rightarrow \gamma$ transformation with increase in the content of the formed austenite at increase in the heating temperature from A_{c_1} to A_{c_3} (see Table 2). Deviation of its volume content from the expected one can be explained by instability of phase transformation critical points. At the stages of heating from A_{c_1} to T_h and subsequent cooling to the austenite transformation beginning the metal remains in the two-phase $\alpha + \gamma$ condition. Part of the α-phase that remains non-transformed is subjected to short-time tempering at the heating (below and above A_{c_1}) and cooling (from the heating temperature) stages to form carbides.

At the temperatures close to A_{c_1}, carbon in steel is characterised by high diffusivity, which is several orders of magnitude higher than at the temperatures close to A_{c_3}. Increase in temperature of metal in the two-phase condition is accompanied by a dramatic decrease in the diffusion coefficient of carbon (see Figure 3) [8]. This decrease in diffusivity of carbon is attributable to decrease in the volume content of the ferritic component of the HAZ metal structure in favour of the austenitic component. Extrapolation of values of the diffusion coefficients of carbon in ferrite to A_{c_3}, and in austenite to A_{c_1}, allowing for dependence $D = D_0 \exp(-Q/RT)$ (here Q is the diffusion activation energy, and R is the universal gas constant), suggests that the ratio of the diffusion coefficients of carbon in the ferritic and austenitic components of the two-phase metal structure amounts to 3–4 or more orders of magnitude.

Low solubility and high diffusivity of carbon in ferrite in a pre-transformation condition (see Figure 3), as well as in a two-phase condition of steel, cause decarburisation of ferrite. Low-carbon austenite formed during the $\alpha \rightarrow \gamma$ transformation process is carburised due to dissolution of carbides and ingress of carbon from ferrite under the effect of difference in chemical potentials, or difference in solubility between structural components. However, a low diffusivity of carbon in the γ-phase and a short-time stay of metal in the two-phase condition cause persistence of a decreased weight volume of carbon in regions located far from the inter-phase surfaces. The inter-phase re-distribution of carbon causes extra decarburisation of the ferritic component. Thus, rapid heating within the intercritical temperature range generates chemical heterogeneity in metal both between the ferritic and austenitic components, and in the austenitic component proper. Austenite with a low carbon content is characterised by a decreased stability, and carburised austenite — by an increased stability. The cooling process is accompanied by the ferritic transformation at 790–615 °C, bainitic transformation at 615–360 °C, and martensitic transformation at temperatures from 295 °C to a room temperature (curve *4* in Figure 1, and Table 2). The range of temperatures of the noted transformations strongly depends upon the heating temperature in a range of $A_{c_1} - A_{c_3}$ (see Table 2). A three-phase structure consisting of ferrite, bainite and martensite is formed in steel. The ferrite phase is composed of super-high tempering ferrite F_{tem} heated above A_{c_1} with a low carbon content, and transformation ferrite F_{tr} with a higher carbon content. Austenite is decomposed into bainite and martensite, which are characterised by a decreased and increased carbon content, respectively, as well as carbide dissolved in austenite. The HAZ metal with such a structure features decreased hardness (*HV* 275–390). The composition of its structure (see Figure 2, *c*), characterised by alternation of fine components of a differing hardness and strength, leads to a 3–3.5 times increase in impact toughness.

Only tempering transformations II, III and IV, related, respectively, to decomposition of retained austenite (220–360 °C), carbide transformations (435–505 °C), coagulation of carbides and re-crystallisation of the ferritic matrix (500–680 °C), are fixed in welding heating of the hardened metal. The above temperatures of tempering transformations are higher than in furnace tempering (230–280, 350–400 and 500–680 °C, respectively). This increase in temperature ranges of the tempering effects is observed in rapid tempering of steels U12, ShKh6 and ShKh15

[9]. In arc tempering of the HAZ metal it is possible to set a higher heating temperature than in furnace tempering.

Rapid heating of the hardened overheated metal to 270 °C causes short-time low-temperature tempering of martensite and transformation of retained austenite into martensite with an increased carbon content. This leads to decrease in hardness (see Table 3) and improves etchability of acicular structure (see Figure 2, *d*). Heating to 360 °C intensifies tempering of initial martensite and causes decomposition of retained austenite to form a bainite-like component. Tempering troostite, in addition to initial bainite, is formed in a metal structure subjected to tempering at a temperature of 410–535 °C. The ferrite-carbide mixture in the metal heated to 625 and 700 °C has no time to coarsen during tempering, and the acicular structure persists (see Figure 2, *e*). Nor does it disappear with decrease in the cooling rate and increase in the cooling time. Increase in the short-time tempering temperature causes, in general, a decrease in hardness and increase in impact toughness of the HAZ metal. Decrease in the cooling rate has hardly any effect on growth of impact toughness.

Refining of austenite grain and martensite cluster is accompanied by growth of tensile strength, yield stress and brittle strength of hardened-tempered steel 12KhN3MFA [10]. In our case it correlates with increase in delayed fracture resistance of a welded joint in steel 30KhGSA subjected to repeated austenising with grain refining and hardening in arc treatment. An up to 6.7 times increase in delayed fracture time τ_f occurs in short-time heating to a temperature of 980–1240 °C, where the highest austenite grain refining takes place, whereas heating to temperatures close to A_{c_1} and T_S, at which a coarse austenite grain is restored, causes almost no increase in delayed fracture resistance (see Table 4). Naturally, the delayed fracture resistance grows with decrease in the rate of cooling of the austenised HAZ metal. Its ten-fold increase is achieved in arc heating to a high tempering temperature. The highest resistance to delayed fracture, up to its prevention, is provided by heating the HAZ metal within the intercritical temperature range, this causing decrease in the martensite content of the HAZ metal structure below the critical point (30 vol.%). The results of tests of the HAZ metal to delayed fracture are in agreement with the data on its impact toughness and hardness.

The investigations conducted reveal relationship between parameters of the thermal cycles of welding and arc treatment, formed structures and properties of the hardened HAZ metal in high-strength steel.

CONCLUSIONS

1. Arc treatment provides improvement of structure and properties of the HAZ metal of a joint in steel 30KhGSA hardened during welding. At $A_{c_1} < T_h < A_{c_3}$, a 1.5–3.5 times increase in impact toughness and prevention of delayed fracture are achieved owing to decrease in the total content of hardening structure components. At $T_h < A_{c_1}$, an up to 2.5 times increase in impact toughness (depending upon the heating temperature) and multiple increase in delayed fracture resistance occur due to tempering. Heating to $T_h = A_{c_3} + (150–400)$ °C causes a substantial increase in delayed fracture resistance of the HAZ metal with an insignificant (up to 1.3 times) increase in impact toughness of the repeatedly hardened metal due to austenite grain refining. Regulation of structure and mechanical properties of the HAZ metal through the heating and cooling rates in arc treatment is less efficient than through the heating temperature.

2. Austenitic transformation of metal in formation of HAZ under the arc welding conditions takes place at an increased temperature. The hardened HAZ metal is characterised by a decrease in the austenite formation temperature, compared with base metal. During the process of arc treatment its transformation in tempering occurs at higher temperatures than in the case of furnace tempering.

1. (1974) *Technology of fusion electric welding of metals and alloys*. Ed. by B.E. Paton. Moscow: Mashinostroenie.
2. Paton, B.E., Savitsky, M.M., Kuzmenko, G.B. (1994) Prospects of application of high-strength medium-alloy steels in welded high-pressure cylinders for motor transport. *Avtomatich. Svarka*, **3**, 4–9.
3. Kulik, V.M., Savitsky, M.M., Novikova, D.P. et al. (2004) Features of argon-arc treatment with insipient melting of welded joint on quenching steel. *The Paton Welding J.*, **3**, 15–20.
4. Kulik, V.M., Savitsky, M.M., Bursky, G.V. (2005) Evaluation of delayed fracture resistance of HAZ metal of high-strength steel with modelling of stress relaxation. *Ibid.*, **4**, 17–22.
5. (1983) *Metals science and heat treatment of steel*: Refer. Book. Vol. 3: Principles of heat treatment. Ed. by M.L. Bernshtein, A.G. Rakhshtadt. Moscow: Metallurgiya.
6. Savitsky, A.M., Vasiliev, V.G., Savitsky, M.M. et al. (2005) Influence of the heating stage on structure formation of welded joints on hardening steels. *The Paton Welding J.*, **1**, 15–17.
7. Lobanov, L.M., Mikhoduj, L.I., Vasiliev, V.G. et al. (1999) Features of thermodeformational processes during arc welding of high-strength steels. *Ibid.*, **3**, 3–11.
8. Sazonov, B.G. (1990) Extreme diffusion activity in steel at the state of pre-transformation. *Metallovedenie i Term. Obrab. Metallov*, **7**, 13–15.
9. Gridnev, V.N., Meshkov, Yu.Ya., Oshkaderov, S.P. et al. (1973) *Physical principles of electric thermal hardening*. Kiev: Naukova Dumka.
10. Kotrechko, S.A., Meshkov, Yu.Ya., Telovich, R.V. (2004) Parameters of microstructure which control the brittle strength of low-alloy steels with tempered martensite structure. *Metallofizika i Nov. Tekhnologii*, 26(**4**), 435–456.

ALUMINOCERAMIC PLASMA COATINGS

Yu.S. BORISOV[1], V.F. GOLNIK[1], Z.G. IPATOVA[1], I.V. MITS[1], A.G. SAAKOV[2] and V.A. SAAKOV[2]
[1]E.O. Paton Electric Welding Institute, NASU, Kiev, Ukraine
[2]Research and Production Company TOPAS, Kiev, Ukraine

Aluminoceramic plasma coatings produced by spraying composite powders (mixture of aluminium and iron titanium) were developed. The plasma spraying process was proved to provide coatings containing intermetallic inclusions with microhardness of about 11000 MPa. Aluminoceramic coatings of composite powders with 35–45 wt.% $FeO{\cdot}TiO_2$ have a maximal adhesion strength (45–50 MPa), and those with 25 wt.% $FeO{\cdot}TiO_2$ have the highest resistance to gas-abrasive wear (at all attack angles). Corrosion current density of the coatings of composite powders with 45 wt.% $FeO{\cdot}TiO_2$ in sea water is minimal ($4.0{\cdot}10^{-7}$ A/cm^2). Wear in sliding friction is 10 times lower for a friction pair (steel 30KhGSA + coating) with 45 wt.% $FeO{\cdot}TiO_2$.

Keywords: *plasma spraying, aluminoceramic coatings, composite powders, exothermic interaction, differential thermal analysis, structure of coatings, adhesion strength, gas-abrasive wear, corrosion resistance, wear resistance, protection of pipelines*

Thermal spray coatings based on aluminium and its alloys have received wide acceptance in the last years. Application of aluminium and its alloys for deposition of corrosion-resistant coatings is attributed to low melting point of aluminium, resistance to different aggressive environments, and lower electrochemical potential compared with steel [1]. High corrosion-resistant properties of aluminium coatings ensure their sustained resistance to the atmosphere of industrial cities and towns, sea water, reinforced concrete structures, etc. [2]. However, such coatings feature low wear resistance. Study [3] describes the use of the aluminium and alumina mixture to improve wear resistance.

The study described in this article was conducted to investigate aluminium and $FeO{\cdot}TiO_2$ composite powders (CP), optimise the plasma technology for their spraying, and examine properties of the coatings (adhesion strength, gas-abrasive wear, corrosion resistance in sea water, and wear resistance in sliding friction) compared with properties of plasma coatings of pure aluminium.

Composite powders of aluminium with 10, 15, 25, 35 and 45 wt.% $FeO{\cdot}TiO_2$ were chosen as spraying materials. The choice of $FeO{\cdot}TiO_2$ is based on the fact that reaction of its interaction with aluminium is accompanied by heat release. The reaction may occur in the mode of self-propagating high-temperature synthesis. Release of this extra heat during the coating formation process is a positive factor affecting density of the coatings and strength of their adhesion to the substrate.

Interaction of aluminium with $FeO{\cdot}TiO_2$ may result in formation of intermetallics, according to the constitutional diagram of the Fe–Al, Fe–Ti and Ti–Al systems.

The constitutional diagram of the Fe–Al system showed the presence of the following intermetallics: Fe_3Al, FeAl, $FeAl_2$, Fe_2Al_5 and $FeAl_3$; the constitutional diagram of the Al–Ti system – the presence of Ti_3Al, TiAl and $TiAl_3$ intermetallics; and that of the Fe–Ti system – the presence of Fe_2Ti and FeTi intermetallics [4].

Thermodynamic analysis was conducted to compare CP of interaction products in the Al–$FeO{\cdot}TiO_2$ system with a spray coating of pure aluminium. The main objective of this analysis was to evaluate adiabatic rise in temperature as a result of the exothermic effect of the interaction process. Given that such mixtures contain excessive aluminium at the initial concentrations of $FeO{\cdot}TiO_2$, the following reaction was chosen as the basic one:

$$FeO{\cdot}TiO_2 + Al \rightarrow Al_2O_3 + FeAl_3 + TiAl_3 + Al, \quad (1)$$

or, at a stoichiometric ratio of $Fe{\cdot}TiO_2$ and Al:

$$FeO{\cdot}TiO_2 + 8Al = Al_2O_3 + FeAl_3 + TiAl_3. \quad (2)$$

The balance proportion of the weight content of initial components and reaction products follows from weight ratios of the components according to reaction (2):

$$1 \text{ g } FeO{\cdot}TiO_2 + 1.42 \text{ g Al} = 0.67 \text{ g } Al_2O_3 + 0.9 \text{ g } FeAl_3 + 0.85 \text{ g } TiAl_3. \quad (3)$$

Figure 1 shows variations in composition of this interaction product depending upon the content of $FeO{\cdot}TiO_2$ in the initial mixture. Residual aluminium in the reaction product disappears upon reaching a concentration of 41.3 wt.% $FeO{\cdot}TiO_2$.

The following values of compound formation heat, kJ/mol, were used to calculate exothermicity of the reaction [5]:

$$FeO{\cdot}TiO_2 - 1237.3; \quad Al_2O_3 - 1575.5;$$
$$FeAl_3 - 11.5; \quad TiAl_3 - 142.$$

Based on these data, the exothermic effect of reaction (2) is as follows:

$$Q_{ex} = 1575.5 + 111.5 + 142 - 1237.3 = 591.7 \frac{\text{kJ}}{\text{mol } FeOTiO_2} \text{ or } 3.9{\cdot}10^3 \frac{\text{kJ}}{\text{kg } FeO{\cdot}TiO_2}. \quad (4)$$

The adiabatic rise in temperature, ΔT_{ad}, was evaluated by using Kelly approximation [6] as heat capacity

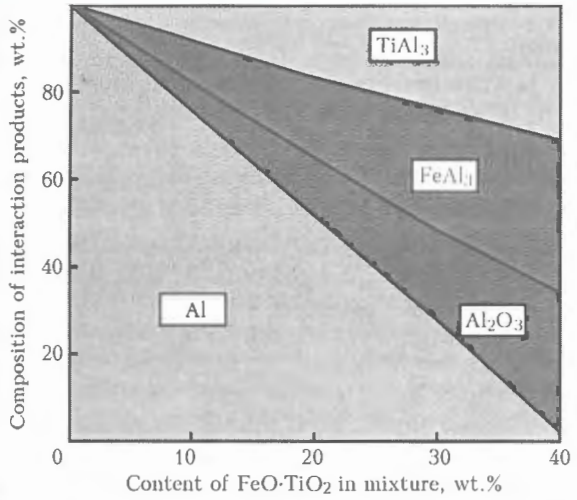

Figure 1. Composition of interaction products for the Al + $FeO \cdot TiO_2$ mixture

C_p, i.e. $26.5n$ J/(mol·K), where n is the number of atoms in a molecule. On this basis, heat capacity of individual reaction products (kJ/(kg·K) is 0.981 for Al, 1.299 for Al_2O_3, 0.775 for $FeAl_3$, and 0.822 for $TiAl_3$.

The weight proportions of components in the interaction products being taken into account, we have, according to (3), that adding 10 g $FeO \cdot TiO_2$ to the mixture results in formation of 24.2 g of the reaction products with the following heat capacity:

$$C_p = 6.7 \cdot 1.299 + 9 \cdot 0.775 + 8.5 \cdot 0.822 = 22.66 \text{ kJ/(kg·K)}. \quad (5)$$

$100 - 2.42m$ of residual aluminium (where m is the content of $FeO \cdot TiO_2$ in the mixture, wt.%) has the following heat capacity:

$$C_p = 0.981 \cdot (100 - 2.42m) \text{ kJ/(kg·K)}. \quad (6)$$

Then, heat capacity of the reaction products is

$$C_p = 2.266m + 0.981 \cdot (100 - 2.42m) = 98.1 - 0.108 \text{ kJ/(kg·K)}. \quad (7)$$

Proceeding from expressions derived for Q_{ex} and C_p of the reaction products, the value of adiabatic rise in temperature as a result of the interaction process is

$$\Delta T_{ad} = \frac{Q_{ex}}{C_p} = \frac{3.9m \cdot 10^3}{98.1 - 0.108m} \text{ (K)}, \quad (8)$$

or

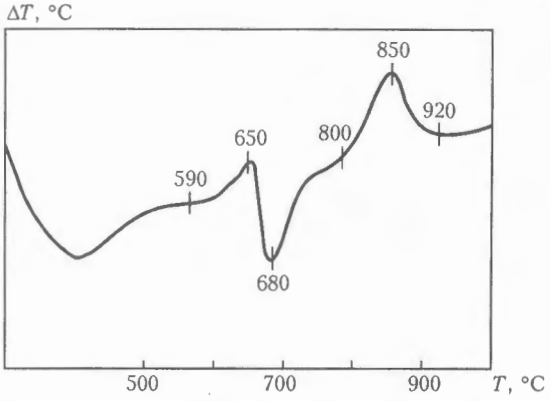

Figure 2. Thermogram of the Al + 45 wt.% $FeO \cdot TiO_2$ mixture

$$\Delta T_{ad} = 40 \text{ wt.\% } FeO \cdot TiO_2 \text{ (K)}. \quad (9)$$

The interaction process was studied by differential thermal analysis (DTA) of three compositions of the mixture of aluminium with 10, 25 and 45 wt.% $FeO \cdot TiO_2$ by using the VDTA-8A unit in helium at a constant heating (cooling) rate of 80 °C/min. Results of DTA for the composition with 45 wt.% $FeO \cdot TiO_2$ are shown in Figure 2. With the content of $FeO \cdot TiO_2$ increased to 45 wt.%, the intensive exothermic reaction in the mixture begins at 800 °C. Composite powders were made in the SM-1 mechanical screw mixer, and zapon of the NTs-62 grade was used as a binder.

The coatings were sprayed with the plasma spraying machine «Kiev-7», by using air and a mixture of air with 5 % of propane-butane as a plasma gas. The technological process was optimised on the basis of the material utilisation factor (MUF) by varying the following parameters: plasma gas flow rate, spraying distance, and plasma arc power.

Spraying with a mixture of air with 5 % of propane-butane, compared with air, was found to provide more homogeneous coatings, which results from smoothing of the temperature profile in a radial section of the plasma jet. Optimal parameters of the process of plasma spraying of CP Al + $FeO \cdot TiO_2$ by using the air + 5 % of propane-butane mixture are given in Table 1. Structure of the coatings was examined using the optical microscope «Neophot-32», and microhardness was measured under a load of 0.49 MPa using the PMT-3 instrument. Etching with an alcoholic solution of hydrofluoric acid reveals boundaries of grains of the metallic matrix. The grains are mainly lamella-like in shape, and most fine grains have a round shape. The average value of microhardness of the metallic matrix is about 420 MPa, that of $FeO \cdot TiO_2$ is

Table 1. Technological parameters of spraying of coatings

CP composition	Current, A	Voltage, V	Spraying distance, mm	Gas flow rate, m^3/h	Powder consumption, kg/h	MUF
Al + 10 % $FeO \cdot TiO_2$	150	200	160	6.0	10.0	0.75
Al + 15 % $FeO \cdot TiO_2$	152	200	165	6.2	10.2	0.80
Al + 25 % $FeO \cdot TiO_2$	155	205	180	6.5	11.0	0.80
Al + 35 % $FeO \cdot TiO_2$	160	205	190	7.0	11.0	0.77
Al + 45 % $FeO \cdot TiO_2$	160	210	200	7.0	11.0	0.80

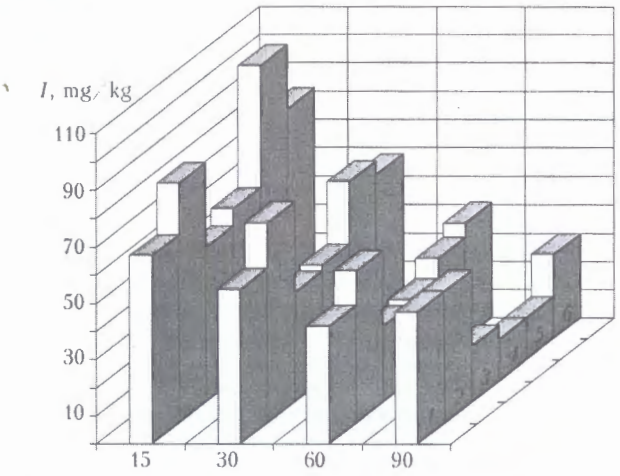

Figure 3. Dependence of mass wear I of aluminoceramic plasma coatings upon the abrasive attack angle: *1* — 100 % Al; *2* — Al + 10 % $FeO{\cdot}TiO_2$; *3* — Al + 15 % $FeO{\cdot}TiO_2$; *4* — Al + 25 % $FeO{\cdot}TiO_2$; *5* — Al + 35 % $FeO{\cdot}TiO_2$; *6* — Al + 45 % $FeO{\cdot}TiO_2$

5800 MPa, and that of dark-grey intermetallic particles is 11000 MPa. Intermetallic detected by metallography must be $FeAl_3$, the microhardness of which is close to the above value [7].

Strength of adhesion of plasma coatings to the substrate of steel 45 was evaluated by the tapered pin breakoff method [8]. The evaluation results are given in Table 2. To compare, the Table also gives results on the adhesion strength of coatings produced from the mechanical mixture of a similar composition. The coating of CP containing 35–45 wt.% $FeO{\cdot}TiO_2$ has a maximal strength of adhesion to the substrate material. This is attributable to the fact that during the spraying process the exothermic reaction of reduction of $FeO{\cdot}TiO_2$ with aluminium occurs in a larger volume with increase in the $FeO{\cdot}TiO_2$ content of the initial charge, which leads to increase in temperature of the particles and, hence, intensifies the process of their interaction with the substrate [9]. Also, it should be noted that all of the examined coatings are 2 or more times superior in their adhesion strength to an aluminium coating. Moreover, as follows from the Table data, coatings of a mechanical mixture are much inferior in their adhesion strength to the coatings of CP of the same composition.

Tests of the coatings to gas-abrasive wear resistance were conducted using the centrifugal accelerator TsUK-3M at a disk rotation speed of 6000 rpm. Quartz sand with particles less than 1 mm in size was used as an abrasive. The study of wear resistance was performed at attack angles of 15, 30, 60 and 90°. Wear was determined from the loss of weight of a coating. To compare, wear resistance of plasma aluminium coatings was also determined. The test results, as well as wear of the coatings per 1 kg of the abrasive, are shown in Figure 3.

The best wear resistance at all attack angles was exhibited by the coating of CP containing 25 wt.% $FeO{\cdot}TiO_2$. Wear of this coating at different attack angles was 1.5–2 times lower than that of the aluminium coating. Wear of all coatings investigated decreased with increase in the abrasive attack angle (see Figure 3). This is attributable to the fact that coatings are ductile, and no spalling of particles results from the front collision of an abrasive with the coating. Increased wear resistance of the coating of CP with 25 wt.% $FeO{\cdot}TiO_2$ may be related to the fact that its structure contains dark-grey particles with microhardness of about 11000 MPa. The presence of non-reacted particles was proved by the results of metallographic analysis, which revealed aluminium and $FeO{\cdot}TiO_2$ particles.

Table 2. Strength of adhesion of plasma coatings to the steel 45 substrate

CP composition	Adhesion strength, MPa	
	CP	Mechanical mixture
100 % Al	20–25	–
Al + 10 % $FeO{\cdot}TiO_2$	20–25	15–20
Al + 15 % $FeO{\cdot}TiO_2$	30–35	20–25
Al + 25 % $FeO{\cdot}TiO_2$	35–40	20–25
Al + 35 % $FeO{\cdot}TiO_2$	45–50	–
Al + 45 % $FeO{\cdot}TiO_2$	45–50	–

The potentiostatic method [10] was chosen to investigate electrochemical behaviour and corrosion resistance of the coatings. The investigations were conducted at room temperature using the electron potentiostate P-5827M. The chlorine-silver electrode was used for comparison. Prior to the measurements, a sample with a coating was held in sea water for an hour to achieve the constant value of corrosion potential, which was measured with no polarisation of the coating. Corrosion rate in the units of current and corrosion potential [11] of each type of the coatings were determined from the polarisation curves by the graphic method through extrapolation of the Taffel regions of the cathode and anode polarisation curves up to their intersection. Electrochemical characteristics of the coatings in sea water are given in Table 3.

Corrosion rate of the coatings of CP with 35 and 45 wt.% $FeO{\cdot}TiO_2$ in sea water is lowest, and a coating of CP with 45 wt.% $FeO{\cdot}TiO_2$ is 1.6 time superior in corrosion resistance to that of aluminium. In addition, the coating of CP with 35 wt.% $FeO{\cdot}TiO_2$ has a more electronegative potential in sea water than the St.3 substrate material (see Table 3), and this coating acts as a protector with respect to the latter, i.e. it provides electrochemical protection of steel from corrosion.

Investigations of wear resistance of the coatings under sliding friction conditions were carried out using the friction machine UMT-1 by the plane–plane method within a load range of 2–4 MPa and sliding rates of 0.1–1.0 m/s. Length of the friction path at a fixed load and friction rate was 500 m. Steel 30KhGSA was used as a mating body. Sea water was fed to the friction zone by the drop method (30 drops per minute). Mass wear of the coating and mating body was measured every 500 m. Antifriction properties of the coatings were evaluated by the friction coefficient of the friction pair. The tests showed that

increase in the specific load and linear rate with increase in percentage of $FeO{\cdot}TiO_2$ in a coating was accompanied by stabilisation of the intensity of mass wear of the sample and decrease in the intensity of mass wear of the mating body. The coating of aluminium CP with 45 wt.% $FeO{\cdot}TiO_2$ has a maximal wear resistance within the load and rate ranges under investigations. The friction coefficient of the friction pair is in a range of 0.3–0.5.

Therefore, as found on the basis of the investigations, the aluminoceramic coatings of CP with 25–45 wt.% $FeO{\cdot}TiO_2$ are superior in their performance to the aluminium ones. Such coatings can be recommended as a substitute for the aluminium ones, which will allow improvement of performance and reduction of costs of the coatings through forming a corrosion-resistant cermet coating and partially replacing aluminium by inexpensive and readily available $FeO{\cdot}TiO_2$. In turn, this will extend the life of structures, components, units and mechanisms with the aluminoceramic plasma coatings operating under different conditions. Thus, the aluminoceramic coatings are intended for wear and corrosion protection of different-application ferrous metal structures operating in aggressive environments with pH 2–12 and salt solutions, pipelines, tanks, ship bodies, bridges, trestles, port and other hydraulic structures, oil platforms, etc. The aluminoceramic coatings protect welds from corrosion and improve their resistance to initiation of corrosion-fatigue cracks [12].

TOPAS Company accumulated practical experience in application of the aluminoceramic coating technology at Open Joint Stock Company AKOR (Ulianovsk, Russia). 57–820 mm diameter pipes with the aluminoceramic coatings and corresponding fittings are designed for construction of heat networks, engineering service lines and other pipelines, and they require no extra cathode protection. The estimated service life of pipelines with the aluminoceramic coatings is not less than 30 years.

CONCLUSIONS

1. Interaction between aluminium and $FeO{\cdot}TiO_2$ is accompanied by release of heat in proportion to the content of $FeO{\cdot}TiO_2$. The interaction process may occur in the mode of self-propagating high-temperature synthesis.

2. As found by metallographic and microdurometric analysis, the coating consists of an aluminium matrix with microhardness of 420 MPa, $FeO{\cdot}TiO_2$ with microhardness of about 5800 MPa, and, most probably, intermetallics $FeAl_3$ with microhardness of 11000 MPa.

3. Investigations of the coating to substrate material adhesion strength showed that aluminium coatings of CP containing 35–45 wt.% $FeO{\cdot}TiO_2$ had maximal adhesion strength (45–50 MPa), which was 2–2.5 times higher than that of the aluminium coatings.

4. As shown by the gas-abrasive wear tests, the best wear resistance at all abrasive attack angles was exhibited by the coating of CP with 25 wt.% $FeO{\cdot}TiO_2$. Wear of this coating was 1.3–2 times lower than that of the aluminium one.

Table 3. Electrochemical characteristics of coatings in sea water

CP composition	Corrosion potential, V	Corrosion rate, A/cm^2
100 % Al	–0.46	$6.3{\cdot}10^{-7}$
Al + 10 % $FeO{\cdot}TiO_2$	–0.48	$6.6{\cdot}10^{-7}$
Al + 15 % $FeO{\cdot}TiO_2$	–0.49	$6.3{\cdot}10^{-7}$
Al + 25 % $FeO{\cdot}TiO_2$	–0.48	$6.3{\cdot}10^{-7}$
Al + 35 % $FeO{\cdot}TiO_2$	–0.54	$5.9{\cdot}10^{-7}$
Al + 45 % $FeO{\cdot}TiO_2$	–0.49	$4.0{\cdot}10^{-7}$
St.3 (substrate material)	–0.50	$2.5{\cdot}10^{-6}$

5. Investigations of electrochemical characteristics of the coatings in sea water showed that coatings of aluminium CP with 45 wt.% $FeO{\cdot}TiO_2$ had the corrosion rate of $4.0{\cdot}10^{-7}$ A/cm^2, which was 1.6 times lower than that of the aluminium ones. Moreover, the coating of CP with 35 wt.% $FeO{\cdot}TiO_2$ was more electronegative than the steel 3 substrate material. It can electrochemically protect steel from corrosion in this environment.

6. Wear tests of the plasma coatings under sliding friction conditions showed that the lowest wear within the load and rate ranges under consideration was exhibited by the friction pair «coating + steel 30KhGSA», when using CP with 45 wt.% $FeO{\cdot}TiO_2$ for spraying. Wear resistance of this pair was 10 times higher than that of the aluminium coating.

7. The aluminoceramic coating produced by spraying CP with 25–45 wt.% $FeO{\cdot}TiO_2$ was shown to have the best combination of properties.

8. Aluminoceramic coatings can be utilised under conditions of the joint effect by corrosion and wear, e.g. for wear and corrosion protection of different-application pipelines, as well as hydraulic structures, bridges, oil platforms and other facilities.

1. Borisov, Yu.S., Kharmalov, Yu.A., Sidorenko, S.L. et al. (1987) *Powder thermal coatings*: Refer. Book. Kiev: Naukova Dumka.
2. *GOST 9.304–87 (ST CMEA 4202–83)*: Thermal coatings. General requirements and testing methods.
3. Hasui, A., Morigaki, O. (1985) *Surfacing and spraying*. Moscow: Mashinostroenie.
4. Hansen, M., Anderko, K. (1962) *Structures of binary alloys*. Moscow: Chorn. i Tsv. Metallurgia.
5. Veryatin, U.D., Mashirev, V.P., Ryabtsev, I.G. et al. (1965) *Thermodynamic properties of inorganic materials*: Refer. Book. Moscow: Atomizdat.
6. Kubashevsky, O., Evans, E. (1954) *Thermochemistry in metallurgy*. Moscow: Inostr. Literatura.
7. Sinelnikova, V.S., Podergin, V.A., Rechkin, V.N. (1965) *Aluminides*. Kiev: Naukova Dumka.
8. Zverev, A.I., Sharivker, S.Yu., Astakhov, E.A. (1979) *Detonation spraying of coatings*. Leningrad: Sudostroenie.
9. Kulik, A.Ya., Borisov, Yu.S., Mnukhin, A.S. et al. (1985) *Thermal spraying of composite powders*. Leningrad: Mashinostroenie.
10. Frejman, L.I., Makarov, V.A., Bryksin, I.E. (1972) *Potentiostatic methods in corrosion investigations and electrochemical protection*. Leningrad: Khimiya.
11. Rejngeverts, M.D., Semenyuk, Z.Ya. (1982) Computer processing of polarization curves for determination of corrosion rate. *Zashchita Metallov*, 18(5), 807–809.
12. Petrov, S.V., Saakov, A.G., Sirotinsky, A.A. et al. (2000) Aluminoceramics protects ferrous metals. *Metally*, **9**, 34–36.

INFLUENCE OF ELECTRIC ARC METALLIZING MODES AND COMPOSITIONS OF APPLIED FLUX-CORED WIRES ON STRUCTURE AND ABRASIVE WEAR RESISTANCE OF COATINGS

V.I. POKHMURSKY[1], M.M. STUDENT[1], I.A. RYABTSEV[2], I.I. SIDORAK[1], Yu.V. DZIOBA[1], V.M. DOVGUNYK[1] and B. FORMANEK[3]

[1]Physical-Mechanical Institute, NASU, Lvov, Ukraine
[2]E.O. Paton Electric Welding Institute, NASU, Kiev, Ukraine
[4]Polytechnica Shlenska, Glivice, Poland

Studied is the influence of electric arc metallizing modes using flux-cored wire FMI-2 on the microstructure and abrasive wear resistance of the coatings. It is shown that among the many factors the compressed air pressure, current and spraying distance have the greatest influence on these characteristics. Wear resistance of coatings, deposited using flux-cored wire with the charge based on ferrochromium-boron, is higher than that of hardened steel. The highest wear resistance is found in coatings deposited at a high pressure of compressed air, which are characterized by finely dispersed structure and containing a large amount of the oxide phase on the interphases.

Keywords: *electric arc metallizing, flux-cored wire, microstructure, abrasive wear*

Electric arc metallizing by flux-cored wires (FCW) is successfully used for restoration of worn-out machine parts that work under the conditions of boundary friction, as well as for their protection from abrasive wear. Industrial experience and experimental studies show that wear resistance of coatings, obtained by this method, depends on their composition, hardness and structure [1]. The aim of this research is to study the influence of the main indices of metallizing modes on the structure and performance of coatings. The possibility of improving the wear resistance of coatings, obtained by electric arc metallizing using flux-cored wire FMI-2 by changing the charge composition, was studied.

When studying the influence of metallizing on wear resistance of obtained coatings, special attention was paid to three main indices: compressed air pressure, on which the degree of FCW melt dispersion in the arc and the speed of formed drop transportation to the spraying surface depend; current, with the increase of which, the efficiency of coating deposition increases; spraying distance that influences the coefficient of sprayed material loss and strength of coating adhesion with the base metal.

Experimental procedure. Coatings were applied by arc spraying pistol ME-2 designed by Company «Gazotermik» at Physical-Mechanical Institute (FMI) of the NAS of Ukraine. FMI-2 FCW of 1.8 mm diameter was used as the basic one. When studying the influence of coating compositions on their wear resistance, the component ratio in the charge of FMI-2 FCW was changed or new components were added. Metallizing modes in the experiments were changed in the limits providing a coating without cracks or delaminations: arc current of 150–300 A; arc voltage of 32–33 V; compressed air pressure of 0.3–0.6 MPa; and spraying distance of 30–100 mm. Metallographic studies of coatings were carried out in «Neophot-2» microscope with a built-in color digital video camera. A mixture of nitric and picric acids was used to determine the microstructure. Testing of abrasive wear resistance of coatings was done by two procedures: standard – Brinell–Hauort (by unfixed abrasive), and by abrasive, wheel – with fixed abrasive (by the procedure developed at FMI of NASU).

When testing by the Brinell–Hauort procedure, a new portion of abrasive is continuously fed into the contact zone between the rubber disk and the studied sample by the dozing device. A feature of this procedure consists in that changing of the force of rubber disk pressing to the sample surface changes the degree of abrasive particles fixing, and is the main parameter that distinguishes this type of wear from the wear by a fixed abrasive. The level of pressing determines if the abrasive particle is firmly held by the rubber disk, performing micro cutting and plastic deformation of the surface, or if it rolls between rubber disk and wear surface, leading to fatigue failure of the latter. Testing mode by the Brinell–Hauort procedure is as follows: loading P = 2.4 MPa, disk diameter – 50 mm, width – 12 mm, rotation speed – 160 rpm, testing time – 15 min. Quartz sand with grain size of up to 200 μm and humidity not higher than 0.16 % was used as an abrasive. Before testing the rubber disk was ground on abrasive paper of type 2 (GOST 6456–75) with graininess # 8P (GOST 3647–71) fixed on flat plate, which was followed by the roller washing in spirit. Sample from steel U8 with hardness *HRC* 60 was used as a standard.

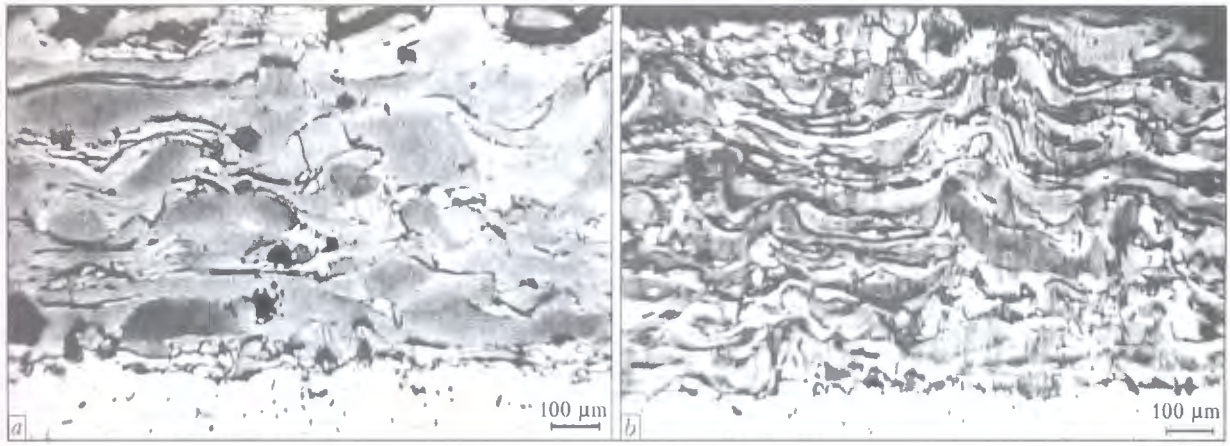

Figure 1. Microstructure of a coating produced by arc metallizing using FMI-2 FCW at U = 32 V, I = 150 A, L = 100 mm and compressed air pressure of 0.3 (*a*) and 0.6 (*b*) MPa

Special device, assembled on small-sized milling machine, was manufactured for wear resistance testing by a fixed abrasive. Instead of a mill, an abrasive wheel from SM-2 electric corundum of medium hardness was fixed on ceramic bond 7K15 of 150 mm diameter and 6 mm width. Electric corundum graininess made 250–315 μm. Samples were fixed on one lever arm and on the other — a load of 0.55 kg weight. The ratio of arms was 2.5:1, abrasive wheel rotation speed was 120 rpm/min, testing time was 120 min.

Plate shaped samples of 40 × 40 × 80 mm size were used for testing by both the procedures. Before coating deposition the sample surface of 40 × 40 mm area was subjected to shot-blasting treatment, and a coating approximately 1 mm thick was deposited in several passes using flux-cored wires of the respective compositions.

Studies of spraying conditions influence on coating structure. *Influence of compressed air pressure*. When conducting experiments, the pressure of compressed air was changed in the range of 0.3–0.6 MPa. At low values (0.3 MPa) its dispersing influence is negligible, and FCW melt drops have a rather big size — about 500 μm. The flight velocity of such particles is low and is equal to about 20 m/s. When encountering the spraying surface, such drops are insignificantly deformed, forming a coarsely dispersed and heterogeneous coating (Figure 1, *a*) with porosity of 5–7 %. Due to a high heat energy of drops their partial micro welding takes place during solidification. Micro cracks are found in some parts of the coating with micro hardness reaching HV 6000 MPa, which are caused by tensile stresses appearing in the process of metallizing.

When compressed air pressure rises up to 0.6 MPa, the size of liquid metal drops decreases up to 80 μm [2], and their velocity simultaneously increases up to 100 m/s, that is favorable for coating structure refinement (Figure 1, *b*). Metal melt drops hit the spraying surface with a great force, being strongly flattened and forming lamellas, for which the length-to-width ratio varies from 3:2 at the compressed air pressure of 0.3 MPa up to 5:1 at 0.6 MPa. The coating that was formed from fine drops, is more heterogeneous and has more interfaces — oxide films. According to the data of phase analysis, these films basically consist of Al_2O_3, Cr_2O_3 and Fe_2O_3 oxides. Irrespective of the compressed air pressure, the main phases of the coating are a solid solution of aluminium and chromium in α-Fe with dispersed precipitates of Fe_2B boride [3].

Influence of current. In arc metallizing with FCW of 1.8 mm diameter, the minimal current is I_{min} = 150, maximum is I_{max} = 300 A. As the drops that form coating, have higher initial temperature, and the coating is formed more compact and with a lower content of oxides (Figure 2), when the current increases from

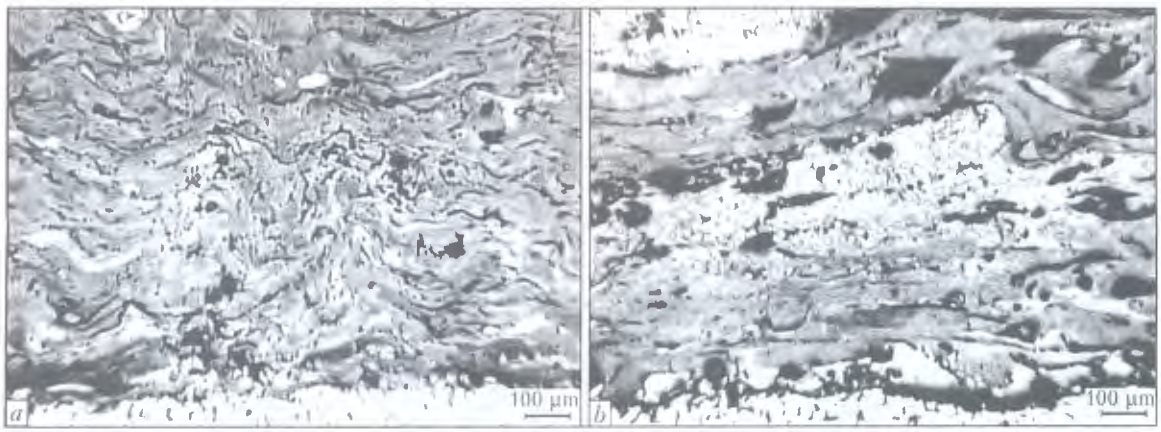

Figure 2. Microstructure of a coating produced by arc metallizing using FMI-2 FCW at U = 32 V, P = 0.6 MPa: *a* — I = 300 A, L = = 100 mm; *b* — I = 150 A, L = 30 mm

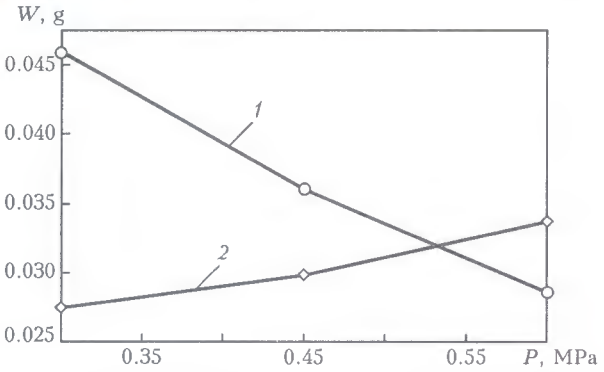

Figure 3. Influence of compressed air pressure on coating wear resistance when testing by fixed (*1*) and unfixed (*2*) abrasive

150 to 300 A, the heterogeneity of the coating deceases. Nevertheless, coating deposition at higher current values can lead to overheating of parts and, as a result, can promote intensive oxidation and spallation of the coating.

Influence of spraying distance. In arc metallizing the bundle of spraying drops has the shape of a cone with divergence angle of 15–20°. Shortening of spraying distance is favorable for increasing of the concentration of molten particles that drop and solidify on the spraying surface, lowering the rate of their solidification and further cooling. The size of forming borides Fe_2B is much larger than when spraying from a shorter distance (see Figure 2, *b*).

Studies of spraying condition influence on abrasive wear resistance of coatings. *Influence of compressed air pressure*. When studying wear with fixed abrasive, it was determined that increase of compressed air pressure from 0.3 to 0.6 MPa is favorable for wear resistance increase of coatings by 1.6 times (Figure 3, curve *1*). It can be explained by that at high pressure of compressed air the coating has more dispersed structure and contains higher amount of chromium and aluminium oxides, as well as more dispersed precipitates of borides in lamellas. All together this provides a higher micro hardness of the coating, and as in this case wear mainly occurs as a result of micro cutting, wear resistance of the coating increases.

When testing by the Brinell–Hauort method, wear resistance of coatings decreases, on the contrary (Figure 3, curve *2*). This is due to realization of another wear mechanism — coating fails mainly as a result of multiple plastic deformation by abrasive particles and partially due to cutting. In this case coatings with a higher ductility margin will have a higher wear resistance. Spraying of coatings at a low pressure of compressed air (0.3 MPa) leads to an increase of the size of metal melt drops, which while solidifying are cooling longer than fine particles and, as a result, tensile residual stresses are much lower in the coarse-grained coating. At multiple loading of the coating by abrasive particles, it is more difficult for micro cracks to initiate in them, and wear resistance of such coatings is higher when testing with unfixed abrasive.

Metallographic examination revealed that after testing with fixed abrasive the worn-out surfaces of sample showed traces of micro cutting by abrasive particles. Furthermore, pores are opened as a result of micro cutting, they being coarser in coatings formed at a low pressure of compressed air (Figure 4, *b, d*).

The appearance of friction surfaces of samples after wear by unfixed abrasive is different (Figure 4, *c, d*)

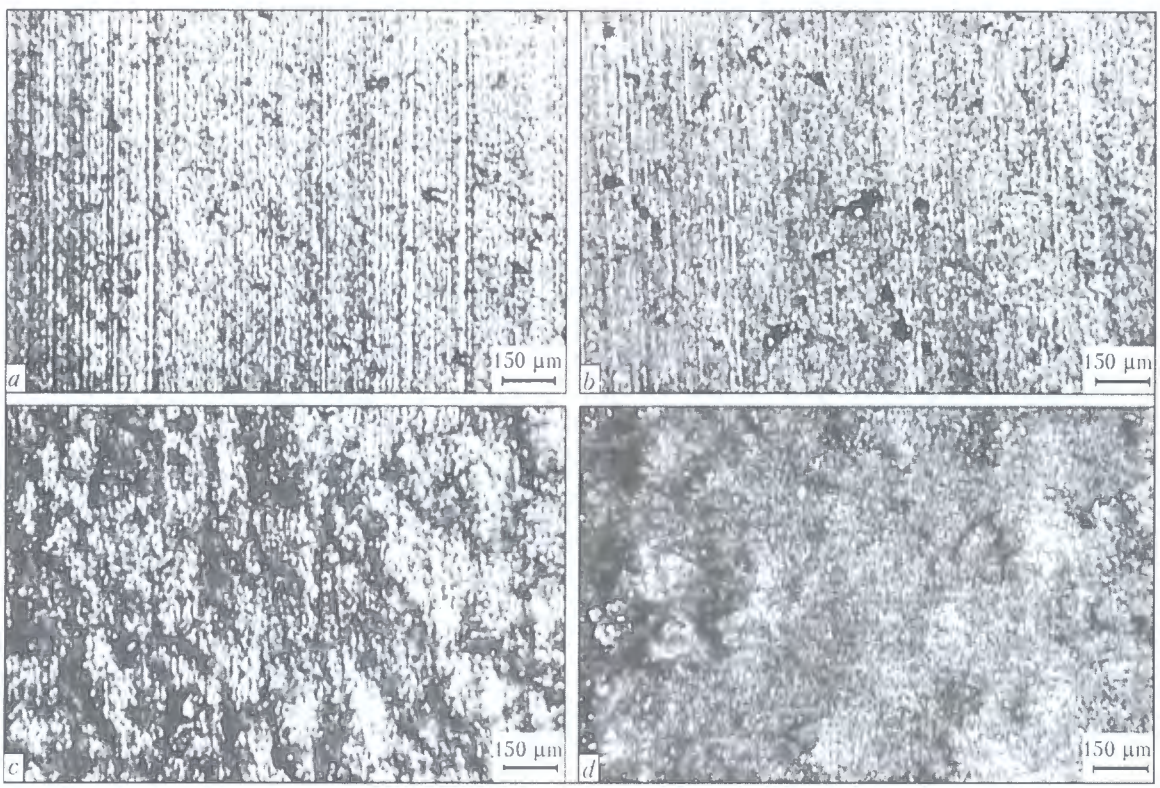

Figure 4. Friction surfaces topography after testing by fixed (*a, b*) and unfixed (*c, d*) abrasive. Metallizing conditions: U = 32 V, I = = 150 A, L = 100 mm, P = 0.6 (*a, c*) and 0.3 (*b, d*) MPa

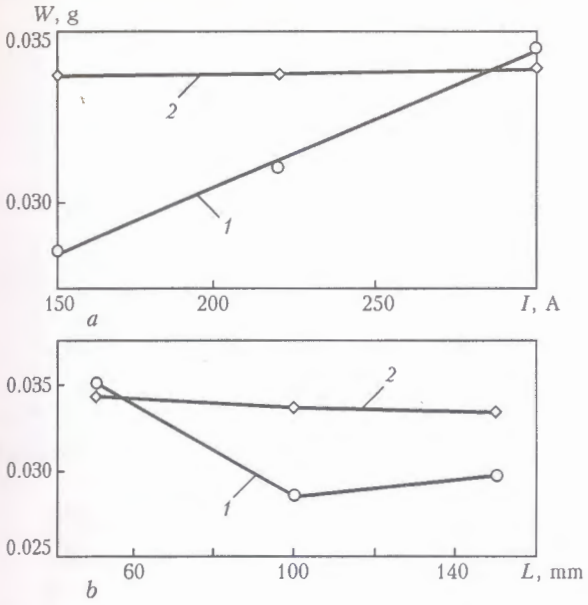

Figure 5. Influence of current (*a*) and spraying distance (*b*) on coating wear when testing by fixed (*1*) and unfixed (*2*) abrasive: *a* — U = 32 V, L = 100 mm, P = 0.6 MPa; *b* — U = 32 V, I = = 150 A, P = 0.6 MPa

that confirms another mechanism of wear by this testing procedure — there are practically no traces of micro cutting by abrasive particles on the worn surface. Fracture runs mainly on lamella interfaces in the fine-grained coating (Figure 4, *c*) and is more uniform in the coarse-grained coating (Figure 4, *d*).

Influence of current. As was noted above (see Figure 2, *a*), increase of current at spraying, reduces the amount of interphases between the structural components in the coating, having an adverse influence on wear resistance when testing by a fixed abrasive (Figure 5, *a*, curve *1*). When testing by the Brinell–Hauort procedure, wear resistance of the coatings practically does not depend on current (Figure 5, *a*, curve *2*).

Influence of spraying distance. When studying the influence of spraying distance on abrasive wear resistance of coatings it was established that minimum wear was found in coatings at spraying distance of 100 mm, when testing by fixed abrasive (Figure 5, *b*, curve *1*). With its increase the particles, forming the coating, stay in air atmosphere longer, and as a result the thickness of oxide films on their surfaces and in the coating, respectively, increases. This is favorable for increasing the coating wear resistance. Wear resistance does not depend from spraying distance when wearing by unfixed abrasive (Figure 5, *b*, curve *2*) and is determined by lamellas size, the size of which does not depend on the spraying distance.

In order to study the possibility of increasing the wear resistance of coatings produced using FMI-2 FCW, B_4C boron carbide was added to its charge composition. It was found that increase of boride content in the coating structure is favorable for hardness increase from *HRC* 40 to 54 (Figure 6, curve *1*). However cohesion strength of the coating in this case

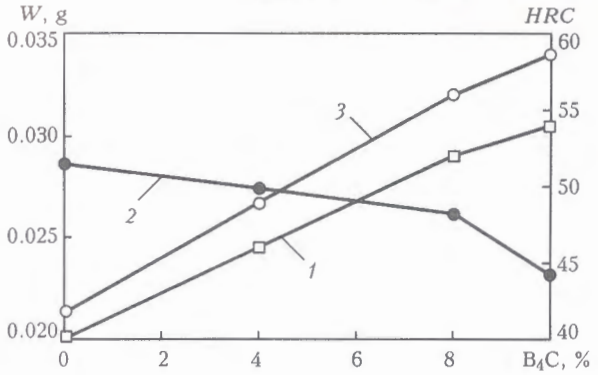

Figure 6. Influence of boron carbide content in FCW charge on hardness (*1*) and wear resistance of coating when testing by fixed (*2*) and unfixed (*3*) abrasive

decreases from 130 to 90 MPa as a result of micro cracks initiation during the layer formation. Wear resistance testing of coatings by fixed abrasive showed that despite an essential increase of hardness, its wear resistance increases only by 25 %, and when testing by unfixed abrasive, on the contrary, it decreases by 30 % (Figure 6, curves *2*, *3*), as surface cracks appear in coating at grinding, which promote predominantly intergranular fracture, as indicated by surface relief (Figure 7).

To study the influence of aluminium content in FCW charge (50 % of ferrochromium-boron + 8 % B_4C + 42 % Cr) on abrasive wear resistance of the coating, chromium was partially replaced by aluminium. It was determined that when the amount of aluminium is changed in FCW charge, coating hardness does not change, and wear resistance (when testing by two methods) increases only by 30 % when chromium is completely replaced by aluminium (Figure 8).

Abrasive wear resistance of coatings of Fe–Cr–B–Al system was compared with wear resistance of hardened steel U8 (*HRC* 60) at similar testing conditions. It was found that wear of hardened steel is 1.5 times higher than that of the coating (Figure 9). Moreover, traces of abrasive disk wear are more homogeneous for steel than for the coating (Figure 10).

In such a way, the conducted tests showed that higher wear resistance is found in coatings produced

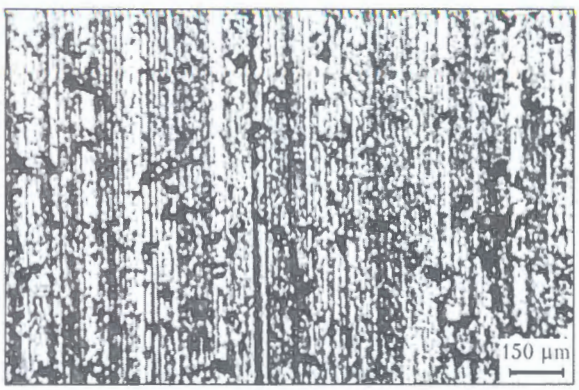

Figure 7. Coating friction surface topography after testing by unfixed abrasive. Spraying conditions: U = 32 V, I = 150 A, P = = 0.6 MPa, L = 100 mm

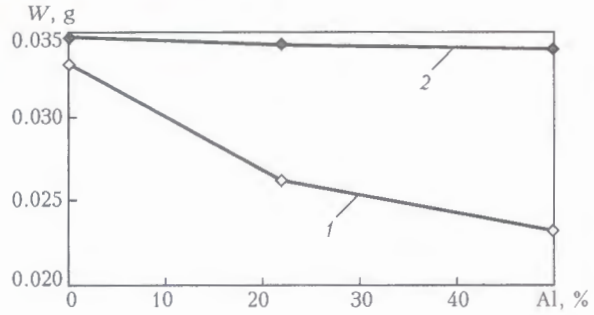

Figure 8. Influence of aluminium content in FCW charge (50 % FCrB + 8 % B_4C + Cr) on coatings wear resistance when testing for wear by fixed (*1*) and unfixed (*2*) abrasive

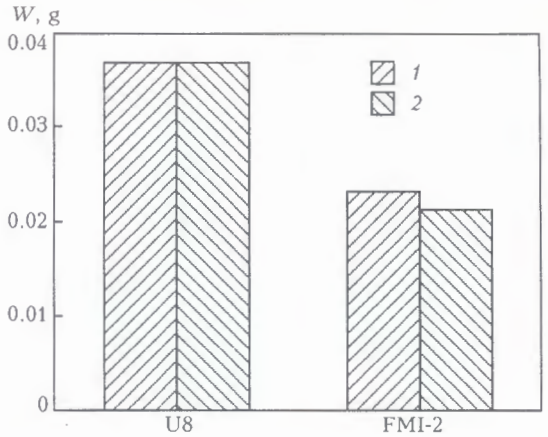

Figure 9. Wear resistance of U8 steel and coating from FMI-2 FCW when testing by fixed (*1*) and unfixed (*2*) abrasive

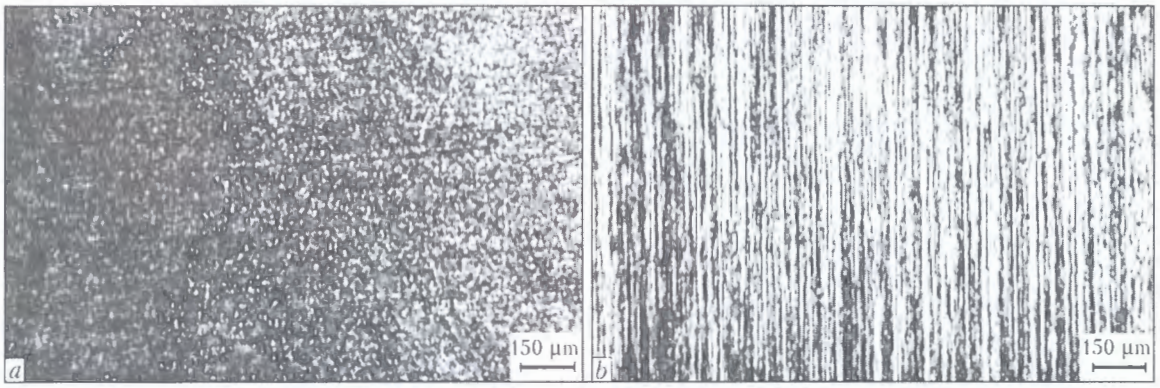

Figure 10. Topography of U8 hardened steel friction surfaces after testing by unfixed (*a*) and fixed (*b*) abrasive

at higher pressure of compressed air and characterized by a more finely dispersed structure. Wear resistance of coatings formed from FCW with the charge on the base of ferrochromium-boron, is 50 % higher than that of hardened steel U8 (*HRC* 60). Addition of boron carbide to the FCW charge increases coating hardness, but decreases its ductility. When testing by fixed abrasive, wear resistance of coatings increases, and with unfixed abrasive it decreases.

1. Dallaraire, S. (2000) Hard arc-sprayed coating with enhanced erosion and abrasion wear resistance. In: *Proc. of ITSC'2000* (Montreal, Canada, May 8–11, 2000). ASM Int.
2. Pokhmursky, V.I., Student, M.M., Dovgunyk, V.M. et al. (2002) Flux-cored wires of FeCrB + Al and FeCr + Al + C systems for electric arc metallizing. *The Paton Welding J.*, **3**, 28–31.
3. Pokhmurska, A., Dovhunyk, V., Student, M. et al. (2002) Tribological properties of arc sprayed coatings obtained from FeCrB and FeCr based powder wires. *Surface & Coating Technol.*, **151/152**, 490–494.

APPLICATION OF HIGH-POWER FIBRE LASERS IN LASER AND LASER-MIG HYBRID WELDING

C. THOMY, H. KOHN and F. VOLLERTSEN
Bremen Institute of Applied Beam Technologies GmbH, Bremen, Germany

Latest developments in laser physics have enabled the production of high-power fibre lasers with beam powers up to 10 kW at excellent beam quality. Adding to these properties their high energetic efficiency, their considerable estimated lifetime and their compact size, they might well be considered to be a viable alternative to both conventional lamp- or diode-pumped Nd:YAG- as well as to CO_2-lasers. However, due to the novelty of the system, very few experiences on their usability for materials processing and in special for welding of steel and aluminium sheet material are existing. To help this situation, both a 7 kW and a 10 kW high-power fibre laser system have been tested by the Bremen Institute of Applied Beam Technologies (BIAS), and their potentials for welding steel and aluminium sheets have been assessed. By the help of these results for pure laser and laser-GMA hybrid welding, of which a selection is presented here, it could indeed be demonstrated that it is possible to remarkably enhance process limitations considering welding speed and sheet thickness previously regarded to be inevitable when welding with solid-state lasers.

Keywords: *laser welding, hybrid welding, steel, aluminium, sheet material, welding speed, thickness, outlook*

New developments in laser physics have recently enabled the construction of novel type laser sources such as the disc laser or the high-power fibre laser. The high-power fibre laser in special has undergone a rapid development in the past 3 years and could (not least due to its modular structure) be scaled from a few hundred Watts up to 10 kW and more [1]. Currently, it is commercially available with beam powers up to 10 kW, thus possessing a sufficient beam power for the vast majority of applications in laser materials processing. However, these systems still have to be qualified, e.g. for laser and laser-GMA hybrid welding processes [2].

The fibre laser just like the Nd:YAG-laser belongs to the large group of solid-state lasers. The laser-active medium normally consists of a glass fibre doped with ytterbium and optically pumped by diodes at the ends and through the clad shell surface by bragg grating. The wavelength is 1070 ± 5 nm.

This novel type laser has various advantages. Its efficiency (up to 25 %) exceeds the efficiency nowadays achievable with lamp- or diode-pumped Nd:YAG-lasers. Due to the improved beam quality (2003: BPP 17.5 mm·mrad for a 10 kW system, 8.5 mm·mrad for a 5 kW system; 2004: 12.5 mm·mrad for a 10 kW system, 5 mm·mrad for a 5 kW system; source: IPG) compared to lamp-pumped systems (BPP typically around 25 mm·mrad at 4 kW) smaller fibre diameters can be used, thus enabling increased power densities in the focal spot. Moreover, the beam source is extraordinarily compact taking into account its beam power and (due to robust construction, low power supply as well as the long fibre lengths up to 200 m) is fit for flexible and potentially mobile use especially for those fields of application currently not accessible to laser technology. In view of operating costs, the lifetime of the pumping diodes is of crucial importance. It is expected to be significantly longer than for other diode-pumped beam sources.

Beam source properties. In the Table, a comparison of some basic beam parameters of the high-power fibre lasers YLR 7000 and YLR 10000 with those of the diode-pumped Nd:YAG-laser Trumpf HL 4006D, the diode-pumped Nd:YAG-laser Rofin DY044 and the CO_2-lasers Trumpf TLF 6000 and TLF 15000 at

Comparison of basic beam parameters for various laser systems

Beam parameter	YLR 7000	YLR 10000	HL 4006D	DY 044	TLF 6000	TLF 15000
Maximum beam power at workpiece, kW	6.9	10.0	4.0	4.2	5.5	13.6
Fibre core diameter, μm	300	200	600	400	–	–
Focal length (typical), mm	200	200	150	200	350	300
Beam diameter (focus), μm	510	360	430	434	262	512
BPP, mm·mrad	18.5	11.6	23.9	15.7	6.7	15.3

*This paper was presented at the Second International Conference on Laser Technologies in Welding and Materials Processing (Katsiveli, Crimea, Ukraine, May 23–27, 2005) and was published in the Proceedings of this Conference (Kiev: PWI, 2005, pp. 46–48).

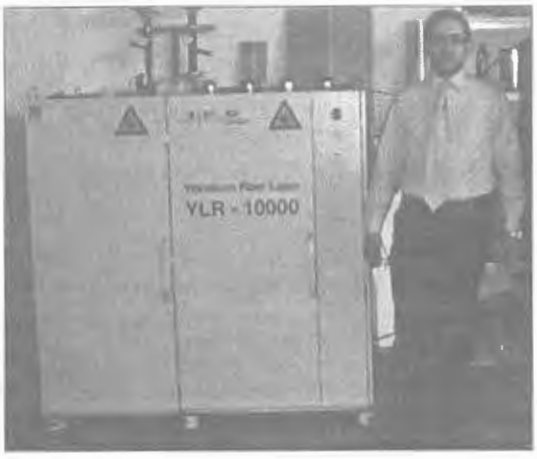

Figure 1. High-power fibre laser IPG YLR 10000

their respective maximum beam powers is given. All measurements have been carried out by BIAS.

The YLR 10000 fibre laser (Figure 1), less than one year after the YLR 7000 system, comes with a significantly improved performance in terms of both output power and beam quality. It delivers 10 kW to the workpiece through a 200 μm fibre and is typically focused by a set of 125 and 200 mm optics for collimation and focusing, respectively to a beam diameter of 360 μm. The beam parameter product is as low as 11.6 mm·mrad. Moreover, due to a compact design this laser has a very small footprint. The wall plug efficiency is 25% (source: IPG).

It may be concluded from the Table that the high-power fibre lasers have beam properties comparable or superior to those of the diode-pumped Nd:YAG-laser. The BPP of both fibre lasers is still higher than that of the CO_2-laser with 6 kW maximum beam power. However, both fibre lasers have surpassed the YAG-laser systems in terms of both power and beam quality, and that they are now approaching the performance of CO_2-lasers in this respect.

Welding performance in steel and aluminium. To assess the potentials of both fibre laser systems, bead-on-plate welds have been performed for various steel (mild steel S235 JR, pipeline steel X70, austenitic stainless steel 1.4404) and aluminium materials

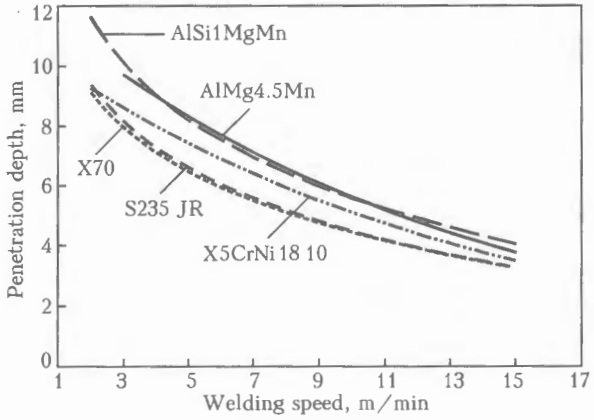

Figure 2. Penetration curves for variety of materials (YLR 10000, focal position z = 0, P_L = 10 kW, Precitec YW50, f = 200 mm, coaxial shielding gas supply (Ar) of 20 l/min)

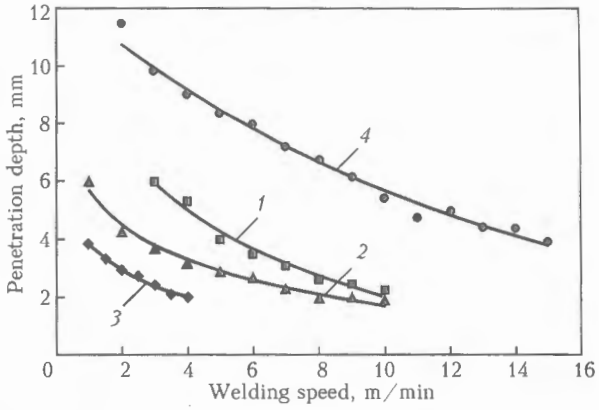

Figure 3. Penetration for various laser systems in aluminium (6XXX) (P_L = max, z = 0, f = 200 mm): *1* — 6.9 kW high-power fibre laser YLR 7000; *2* — 4 kW diode-pumped Nd:YAG-laser DY 044; *3* — 4 kW lamp-pumped Nd:YAG-laser HL 4006D; *4* — 10 kW high-power fibre laser YLR 1000

(AA5083, AA6056 and AA6082). Shielding gas for all welds was argon.

It is evident from Figure 2 that both mild steel grades yield a similar penetration depth at a given welding speed. Roughly, a penetration of 8, 6 and 4 mm was achieved at 3, 6, and 11 m/min. For the stainless steel grade, the attainable welding speed was significantly (up to 50 %) higher compared to the mild steel grades. The most noticeable observation, however, is the penetration depth in the two aluminium materials which is by far superior in particular

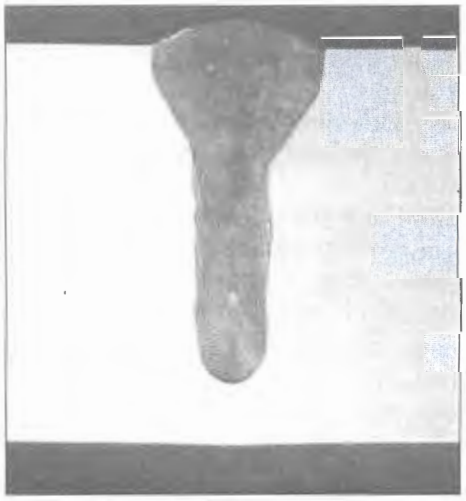

Figure 4. Bead-on-plate weld on AA6082 (t = 12 mm, P_L = 10 kW, v_w = 3 m/min)

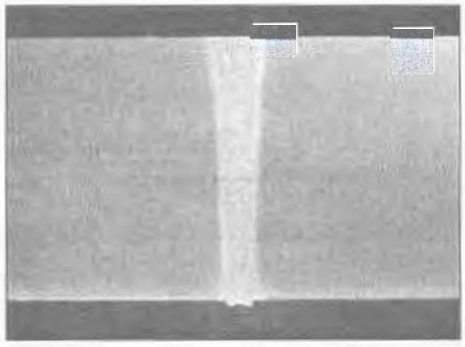

Figure 5. Butt weld of X70 steel (t = 11.2 mm, P_L = 10 kW, v_w = = 2.2 m/min)

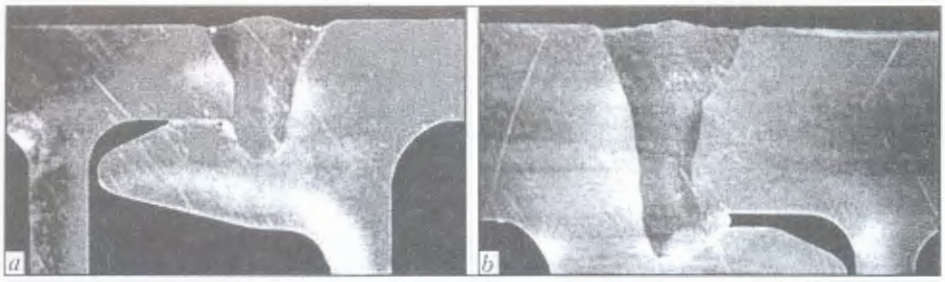

Figure 6. First fibre laser GMA-hybrid welds (EN-AW 6008, t = 4 (*a*) and 8 (*b*) mm)

with respect to the mild steel grades. For aluminium, a depth of 8, 6 and 4 mm was exceeded at speeds of 5, 9 and 14 m/min, respectively.

From Figure 3 it can be concluded in comparison with other solid-state lasers (see the Table) that with respect to penetration the 10 kW fibre laser offers a tremendous performance, in particular for aluminium, which can be attributed to the unique combination of laser power and beam quality at a near infrared wavelength, and which to the best of our knowledge outclasses the performance of any other common laser systems.

A typical bead-on-plate weld on aluminium AA 6082 (Figure 4) obtained during the first tests of the IPG YLR 10000 shows a penetration of 10 mm at a welding speed of 3 m/min, which is about 2.5 times the penetration achievable with today's diode-pumped Nd:YAG-lasers of the 4 kW class. The weld is extremely narrow with parallel fusion lines and features a nail-head shape at the top. Moreover, the microstructural integrity of the weld is noticeable. In particular, the level of porosity is comparatively low. This coincides with the observation of a remarkably calm and smooth welding process. Despite of using a monofocus beam with a comparatively small waist diameter of 360 μm, instabilities which are frequently observed in highly dynamic laser welding processes of aluminium were not detected here.

Another aspect is the sensitivity to variations in focal position, e.g. due to positioning tolerances. It was concluded that especially for aluminium for a focal position from $z = -5$ to $z = +1$ mm the effect on the penetration depth is rather low. During these tests, which have been performed for both steel and aluminium with perpendicular beam incidence angle, the fibre laser unexpectedly proved to be insensitive considering backreflection problems.

Fibre laser applications for welding of steel and aluminium. An example of butt welding of X70 steel is given in Figure 5. At a welding speed of 2.2 m/min, full penetration was comfortably achieved in 11.2 mm material. The weld seam is narrow, and there is only a small reinforcement on both the crown and the root side. No cracks occurred. Currently, BIAS is developing an all-position welding process for this type of material in various thicknesses for pipe laying applications in the field.

For welding of aluminium extruded profiles for the railway industries, the IPG fibre laser YLR 10000 was applied to hybrid welding, too. Figure 6 shows two first results obtained on EN AW 6008 (wall thickness of 4 and 8 mm, respectively) with filler wire AlSi5. Welding speed was 6 m/min in all cases with laser powers up to 10.5 kW for the 8 mm material. The process was very stable and weld quality was acceptable. Further optimisation might result in even higher welding speeds, especially for a wall thickness about 4 mm.

These results have been rated so promising that further tests to pre-qualify fibre laser GMA-hybrid welding for joining railway structures are scheduled.

Conclusions and outlook. The experimental studies on welding with both high-power fibre lasers performed by BIAS showed very promising results for all materials investigated. Especially in comparison with lamp- or diode-pumped Nd:YAG-lasers, a significant enlargement of the process window towards higher welding speeds and thicker materials could be realized due to the higher beam power at competitive beam quality of the fibre laser. With this highly promising laser, BIAS, aside from other applications, intends in cooperation with their partners from industry to open those applications for laser welding which up to now have not or not successfully used laser sources only due to their properties disadvantageous for their applications.

Acknowledgements. *The authors are particularly grateful to the Deutsche Forschungsgemeinschaft for funding considerable parts of the study in the framework of the Gottfried-Wilhelm-Leibniz-Programm (VO530/7).*

1. Grupp, M., Sepold, G. (2004) Laser system technology. In: *Laser physics and laser applications*. Vol. 1. Part C. Berlin-Heidelberg-New York: Springer.
2. Thomy, C., Grupp, M., Seefeld, T. et al. (2004) Schweiben mit dem Hochleistungs-Faserlaser. In: *Strahltechnik*: Vortraege der 6. Konferenz «Strahltechnik» (Halle, Deutschland, April 26–28, 2004).

PROPERTIES OF CO_2-LASER WELDED JOINTS OF DISSIMILAR MAGNESIUM ALLOYS*

W. KALITA[1], P. KOLODZIEJCZAK[2], L. KWIATKOWSKI[3], M. GROBELNY[3] and J. HOFFMAN[1]
[1]Institute of Fundamental Technological Research, PAS, Warsaw, Poland
[2]Warsaw Technical University, Warsaw, Poland
[3]Institute of Precision Mechanics, Warsaw, Poland

This paper provides the results of investigation that has been carried out on the keyhole laser beam welding of dissimilar magnesium alloys. Welding of workpieces of alloys of MgAlZn (brittle) and MgAlMn (ductile) groups has been performed with the CO_2-laser of maximum power of 2.5 kW. With the chosen flow rate of helium shielding and the beam focal position set on the metal surface the welds with no defects and with nearly parallel boundaries were obtained. The analysis of microstructures of the joints, measurements of hardness distributions and the elemental distributions in the weld cross-sections allowed finding the changes due to beam action and recrystallization. The static tensile strength tests have permitted to determine the conditions when the joints of satisfactory mechanical properties could be acquired. The corrosion immersion tests are also reported.

Keywords: *laser welding, CO_2-laser, magnesium alloys, dissimilar joints, microstructure, mechanical properties, corrosion resistance*

Increasing interest of automotive and aeronautic industries in magnesium alloys is mainly due to their much lower density with respect to traditional materials like steel and aluminum alloys. Development of new magnesium alloys with mechanical properties comparable with traditional materials [1] gave the way to their applications as die-casting parts [2]. That resulted in appropriate fulfilling the sharpening requirements for enviromental protection [3] and transportation safety [4] through the mass reduction and fuel savings. However, the production and processing of sheet elements and modular lightweight structures are still in progress. In this matter the special concern is given to welding, particularly to laser beam welding of magnesium alloys [5–18]. Most of the studies done so far is related to welding of similar alloys. But the extending application of tailored blanks gave attention to laser welding of dissimilar alloys [5].

Experimental. Two cast magnesium alloys AM50 and AZ91, with the chemical composition given in the Table, were machined from the bars to the plates with thicknesses of 4.5 mm, widths of 50 mm and the lengths of welding edges of 100 mm.

Chemical composition of alloys to be welded

Alloy	Alloying elements, wt.%		
–	Al	Mn	Zn
AM50	5	0.3	0.2
AZ91	9	0.17	0.7

The butt welding of plates of similar and dissimilar alloys has been performed with fast axial flow (FAF) CO_2-laser with the beam of the mode close to TEM_{10} focused to the diameter of 0.25 mm by the ZnSe lens of 5". No filler metal has been used. After some attempts to find the optimal conditions of welding, the laser power has been set at 2 kW, the speed of welding at 4 m/min and, after evaluation of the influence of the focal point position (with respect to material surface) on the shape of the seam, the focal position of the beam has been chosen on facing surface of plates. The helium shielding of the facing surfaces was provided from the nozzle of 4 mm in diameter with the flow rate of 15 l/min, and the bottom surfaces were shielded by the blow of argon.

The microstructure and the hardness profiles have been evaluated on the cross-sections perpendicular to the direction of beam scanning as well as on the cross-sections done parallelly to the facing surface along the seam. In order to find any changes due to the action of laser beam (e.g. evaporation of material and convection) the analysis of elemental distribution of basic elements has been performed with X-ray microprobe. The mechanical properties of the joints have been revealed by the tests on the Instron stand for static tensile strength. After the fracture of workpieces the SEM images of fractures were obtained to compare with fractures of the parent material. Welded samples were also exposed to neutral 0.15 M NaCl for a 22 days and periodically inspected by a naked eye. After 3 days of exposure pH of solutions has changed to approximately 11 and was stable to the end of experiment.

Results. The macrostructures of the butt-welded joints for similar and dissimilar alloys are presented in Figure 1. The boundaries of the fusion zones are nearly parallel and the aspect ratios of welds (thick-

*This paper was presented at the Second International Conference on Laser Technologies in Welding and Materials Processing (Katsiveli, Crimea, Ukraine, May 23–27, 2005) and was published in the Proceedings of this Conference (Kiev: PWI, 2005, pp. 182–185).

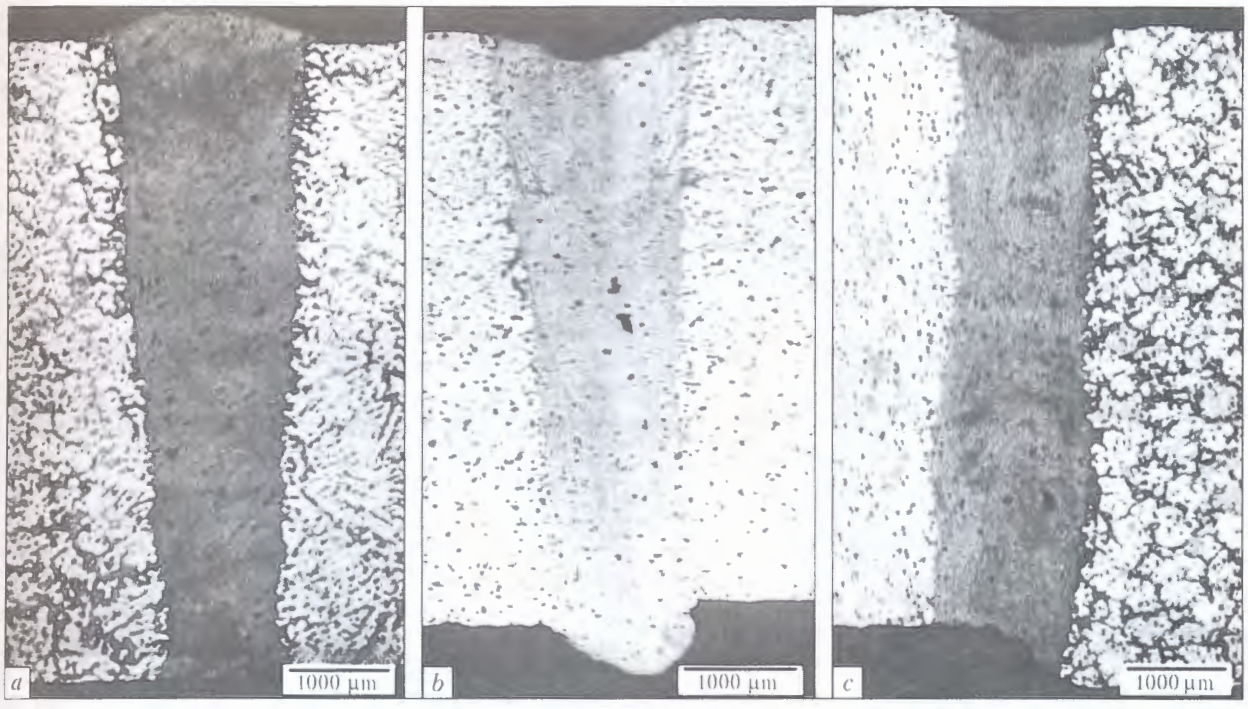

Figure 1. Macrostructure of butt-welded joints: *a* — AZ91–AZ91; *b* — AM50–AM50; *c* — AM50–AZ91

ness of a plate to mean width of the fusion zone) are of high value indicating that the keyhole effect of beam penetration was responsible for the joining. The parent materials contained no pores and after welding the fusion zones are practically free of them. Also, no cracks are observed.

Due to the short time of irradiation (determined approximately as the ratio of beam diameter to welding speed of less than 4 ms) and fast solidification the fusion zones are characterized by significant grain refinement (Figure 2). The sharp transitions from the base metal to the fusion zone with no distingusihed direction of solidification at boundaries of these zones may indicate that there is no heat-affected zone that, on contrary, may easily be found, e.g. for joints of steel or titanium alloys.

The measurements of hardness distributions in the cross sections of welds (perpendicular to the direction of welding) have shown significant increase of hardness in the fusion zones in comparison to the base material. These results (Figure 3) may be associated not only with the high grain refinement in the weld but also with the increase of precipitations at the grain boundaries and appearance of intermetallic compounds. A share of these factors need further investigations.

For the determination of the changes in the chemical composition of materials caused by the influence of beam action the measurements of elemental distributions have been performed by means of X-ray microprobe. It was found that due to the very low boiling point of magnesium in comparison with that of aluminum, the percentage share of magnesium in the joints of similar alloys has been slightly decrased by evaporation of this element.

The static tensile tests of samples of parent alloys and the welds have been performed on the Instron stand. The stress versus strain curves for joints of similar alloys and the base metals are presented in Figure 4. It has been observed that the fracture of welded samples for all alloys appeared far from the fusion zone boundaries, namely in the region of base

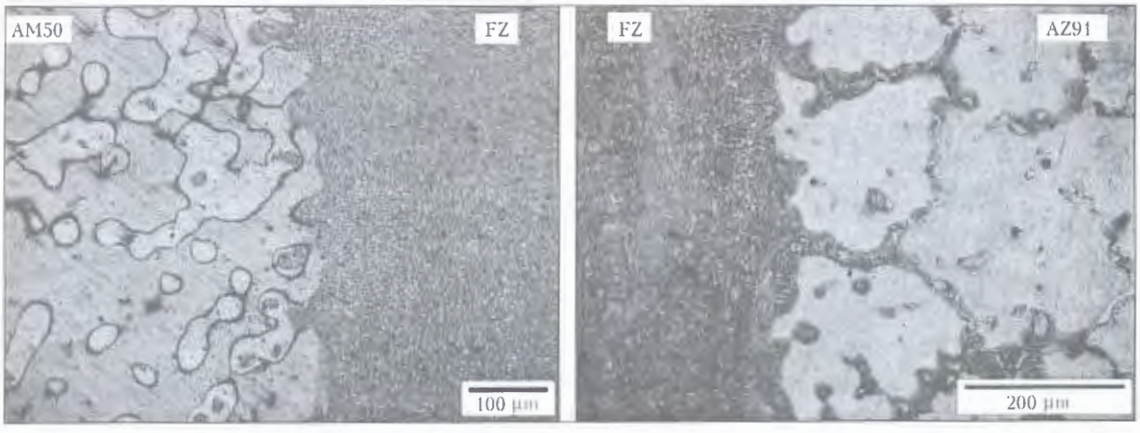

Figure 2. Microstructure of the transition area from fusion zones (FZ) to base matal in the AM50–AZ91 alloy disssimilar joint

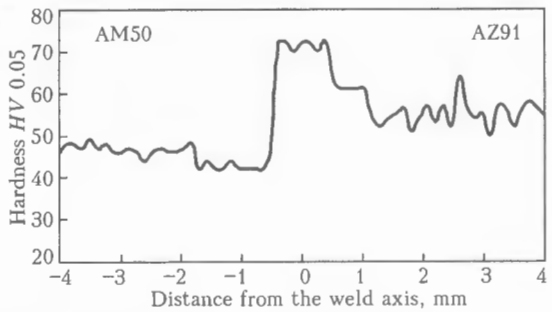

Figure 3. Hardness profile across the weld on dissimilar alloys measured at 1.5 mm from the facing surface

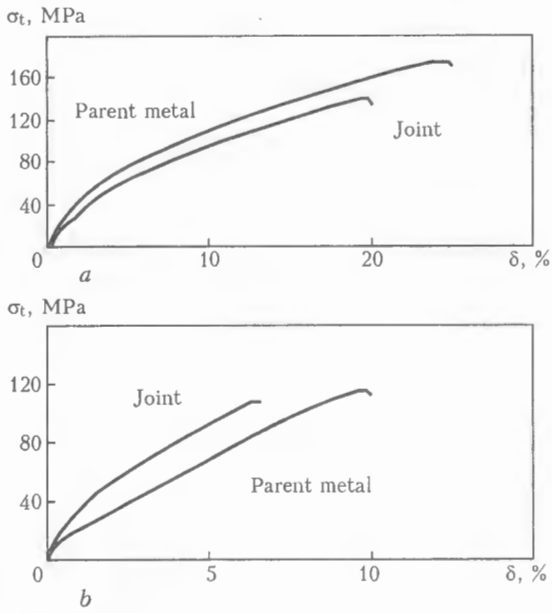

Figure 4. Stress-strain diagrams for the joints of similar alloys: *a* — AM50; *b* — AZ91

metal. As it could be expected the joints of similar alloys have smaller elongation at fracture than the parent materials, however there are differences for tensile stress: for AM50–AM50 joint the stress at fracture is lower and for AZ91–AZ91 higher than those for base metal samples.

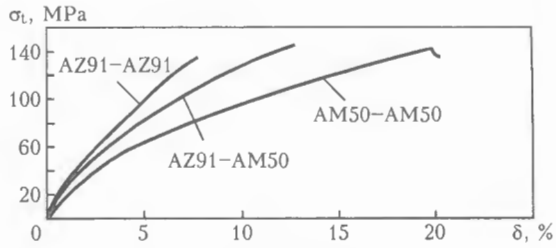

Figure 5. Stress-strain diagram for the joints of similar and dissimilar alloys

For the joints of dissimilar alloys the workpieces broke at the AZ91 side, also far from the fusion zone. The comparison of stress-strain curves for all welded joints is given in Figure 5. According to anticipations the elongation at fracture for dissimilar joints has the value between those of the joints of brittle alloy AZ91 and the ductile alloy AM50.

Since the fracture of the welded samples occurred far from the fusion zones the SEM images of fracture surfaces of the workpieces made of parent materials and samples with the joints displayed no differences.

For the corrosion behavior of welded samples the corrosion immersion tests have been performed. The results of 22 days of samples immersion in 0.15 M NaCl is shown in Figure 6. The changes on surfaces for both sides of the samples (front, rear) are very similar, therefore only the front view is given. It is seen that galvanic couple is being formed between dissimilar alloys. It is worthy to note that AZ91 in this galvanic couple is protected and exhibits much better properties than AZ91–AZ91 couple, while AM50 works as sacrificial electrode. It is also important to underline that a welded joint in AZ91–AM50 couple plays insignificant role in corrosion process. More corrosion effects is seen on a joint for AZ91–AZ91 couple. This very interesting example is being studied in order to clarify observed behavior since

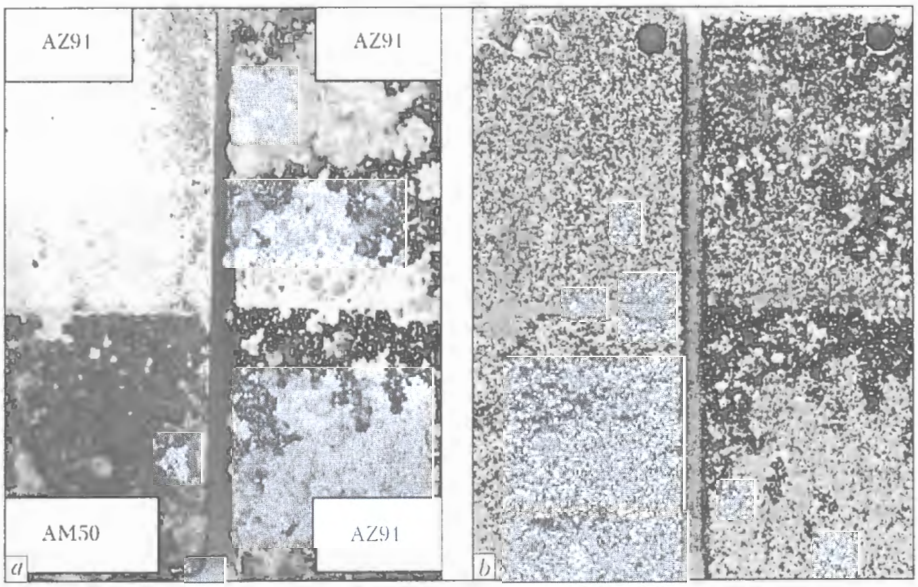

Figure 6. Images of corroded surfaces after 22 days of immersion in 0.15 M NaCl: *a* — just after withdrawing from the solution; *b* — after removal of precipitates due to pickling in H_2SO_4

differences in electrode potentials are not very large. From our previous studies [18] the following results were obtained:

- for AZ91 $E_{cor} = -1.5473$ *V* versus *SCE*;
- for AM50 $E_{cor} = -1.5826$ *V* versus *SCE*.

Therefore, a difference is approximately 35 mV which is not extremely high for the occurrence of galvanic corrosion. Usually 50 mV is considered as a limit. Detailed explanation will be given after collection of additional results.

CONCLUSIONS

The following remarks can be made regarding the CO_2-laser welding of similar and dissimilar magnesium alloys:

1. Welding of similar and dissimilar alloys in the same conditions (for plate thicknesses equal to 4.5 mm with 2 kW laser power at speed of 4 m/min, helium shielding, focal position at facing surface) resulted in nearly the same high aspect ratios of the fusion zone, with practically no porosity and without cracks. No heat-affected zone may be observed and no distinguished direction of solidification can be noticed at fusion zones boundaries.

2. In all cases, the high grain refinement and increased precipitations in the fusion zones may be observed that heightened the hardness in these regions.

3. In the static tensile tests the fractures occurred far from the weld (in the base metal), i.e. dissimilar weld on the side of brittle alloy AZ91. The plastic properties of samples with welds are lower than those for the parent materials.

4. The results of corrosion immersion tests performed in 0.15 M NaCl showed that welding of dissimilar magnesium alloys, in this case AZ91–AM50, increases a susceptibility to galvanic corrosion even if the difference between electrode potential values are not apart each other. However, an influence of a weld is rather negligible. An exact interpretation requires further studies.

Acknowledgements. *This work was done within the framework of research project No. 4 T08C 009 25 supported by the National Committee for Scientific Research in 2003–2005.*

1. Friedrich, H., Schumann, S. (2001) Research for a «new age of magnesium» in the automotive industry. *J. Mat. Processing Technol.*, **117**, 276–281.
2. Longworth, S.J.P. (2001) *The bolting of magnesium components in car engines*: Dis. for the degree of Master of Ph. to the University of Cambridge.
3. Aghion, E., Bronfin, B., Eliezer, D. (2001) The role of the magnesium industry in protecting the environment. *J. Mat. Processing Techn.*, **117**, 381–385.
4. Mordike, B.L., Ebert, T. (2001) Magnesium. Properties-applications-potential. *Material Sci. and Eng.*, **A302**, 37–45.
5. Weishait, A., Galun, R., Mordike, L. (1998) CO_2-laser beam welding of magnesium-based alloys. *Welding J.*, **4**(77), 149–154.
6. Draugelates, U., Schram, A., Kettler, C. (1999) Joining of magnesium alloys. *Materialwissenschaft und Werkstofftechnik*, **10**(30), 623–627.
7. Dhahri, M., Masse, J.E., Mathieu, J.F. et al. (2000) CO_2-laser welding of magnesium alloys. In: *SPIE*, **3888**, 725–732.
8. Dhahri, M., Masse, J.E., Mathieu, J.F. et al. (2001) Laser weldability of WE43 magnesium alloy for aeronautic industry. In: *Proc. of LANE* (Erlangen, Germany, Aug. 28–31, 2001).
9. Zhao, H., DebRoy, T. (2001) Pore formation during laser beam welding of die-cast magnesium alloy AM60B – mechanism and remedy. In: *Welding res. suppl.*, 204–210.
10. Sun, Z., Wei, J., Pan, D. et al. (2001) A comparative evaluation on microstructures in TIG and laser welded AZ31 magnesium alloy. In: *SIMTech techn. rep. PT/01/008/JT*, 1–8.
11. Haferkamp, H., Goede, M., Bormann, A. et al. (2001) Laser beam welding of magnesium alloys – new possibilities using filler wire and arc welding. In: *Proc. of LANE* (Erlangen, Germany, Aug. 28–31, 2001), 333–338.
12. Lathabai, S., Barton, K.J., Harris, D. et al. (2003) Welding and weldability of AZ31B by gas tungsten arc and laser beam. In: *Proc. of Magnesium Technology Conf.* (San Diego, USA, March 2–6, 2003), 157–162.
13. Watkins, K.G. (2003) Laser welding of magnesium alloys. *Ibid.*, 153–156.
14. Stern, A., Munitz, A., Koln, G. (2003) Application of welding technologies for joining of Mg alloys. Microstructure and mechanical properties. *Ibid.*, 163–170.
15. Kalita, W., Kolodziejczak, P., Pokhmurska, H. (2003) Welding of Mg-based alloy AM20 by CO_2-laser beam. In: *Proc. of Int. Conf. on Laser Technologies in Welding and Materials Processing* (Katsiveli, Ukraine, May 19–23, 2003), 214–216.
16. Dasgupta, A.K., Mazumder, J. (2004) Laser welding of AM60 magnesium alloy. In: *Proc. of Magnesium Technology Conf.* (Charlotte, USA, March 14–18, 2004), 43–48.
17. Kolodziejczak, P., Kalita, W., Hoffman, J. et al. (2004) Laser welding of magnesium-based alloys of MgAlZn group. *Advances in Manufacturing Sci. and Techn.*, **4**(28), 45–53.
18. Kalita, W., Kolodziejczak, P., Kwiatkowski, L. et al. (2004) Properties of the butt-welded joints of CO_2-laser welded Mg alloys. In: *Proc. of LANE* (Erlangen, Germany, Sept. 21–24, 2004), **1**, 317–328.

GLASS JOINING TECHNOLOGIES AND EXAMPLES OF THEIR APPLICATION

G. KOEHLER, G. MUELLER, U. BASLER, St. DAHMS, R. LUHN, S. KASCH and S. WAECHTER
Institute of Joining Technology and Materials Testing, Jena, Meuselwitz, Germany

The Institute of Joining Technology and Materials Testing is active in studies of different joining methods (diffusion bonding, brazing, soldering, adhesive bonding, laser welding, etc.) aimed at producing permanent joints in different materials with low residual strains. They include optical and technical glasses (silicon glass, infrared materials, borosilicate glass, VK7), glass ceramics with low thermal expansion (CERAN, CERODUR), crystals (sapphire, CaF_2, MgF_2), high-temperature ceramics (Al_2O_3, SiC), and metals (unalloyed and alloyed steels, precious metals, magnesium and titanium alloys, non-ferrous metals).

Keywords: *technologies of permanent joining, diffusion bonding, soldering, brazing, laser welding, glass, glass ceramics, ceramics, crystals, metals*

In recent years inorganic nonmetallic materials became widely used in various branches of industry and economics. Among them the most popular are glass and glass ceramics, which meet the most stringent requirements in terms of thermal, chemical and mechanical properties. They are widely used in aerospace industry, instrument engineering, analytical and measuring devices, electrical engineering and electronics, medicine, as well as in micro- and nanotechnologies. Glass and glass ceramics thanks to such properties as stability at high temperatures, corrosion- and wear resistance, chemical stability and biological compatibility, in many cases are a successful substitution of metallic materials.

In parallel with developments in the field of inorganic nonmetallic materials, ever more new requirements to production technologies are put forward, which in its turn leads to the necessity to permanently improve them, for instance, the technology of joining said materials.

Diffusion bonding of glass and crystals. In connection with the existence of a great number of different combinations of the base materials, diffusion bonding has become a necessary addition to the existing joining technologies. It is used, in particular, where traditional joining methods are becoming unsound on technological and economical grounds. This concerns in the first place soldering, brazing and adhesive bonding, since filler materials can adversely affect the joint (gas emission, resistance to ageing, atmospheric durability). Weak point also is that for a number of silicate glasses joints, respective solders have not been developed. Besides, soldering, brazing and adhesive bonding appeared unfit for glass ceramics and optical glasses, since they adversely affect optical properties (light transmission, refraction, etc.) of the base material.

Diffusion bonding is applied in various technologies (Figure 1). Thanks to diffusion processes taking

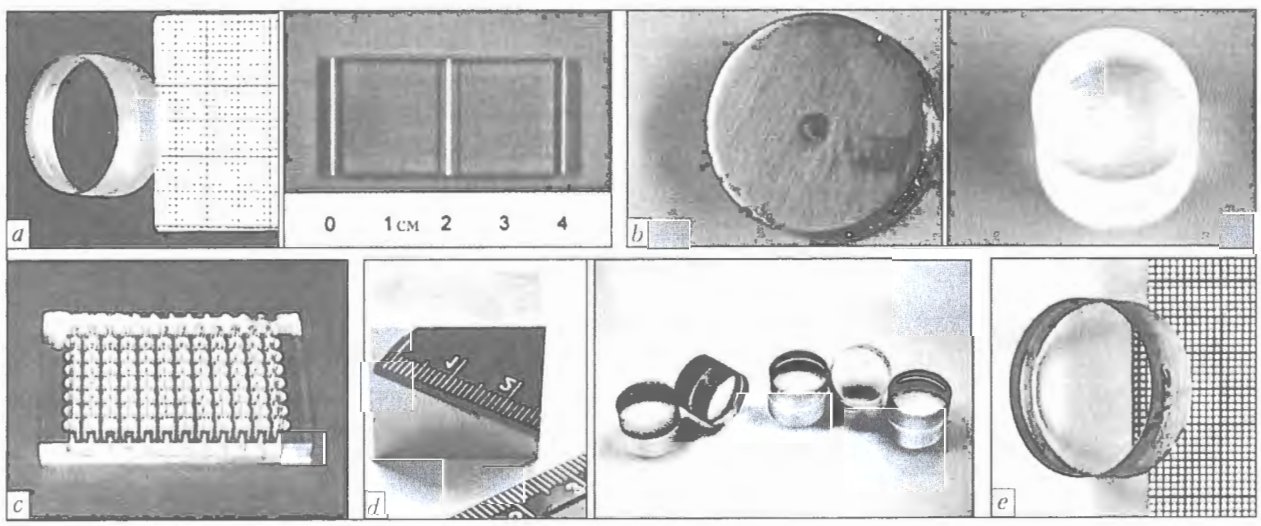

Figure 1. Examples of using diffusion bonding in optics and measuring instruments making technologies: *a* — optical components; *b* — glass ceramics CERAN and CERODUR for measuring instruments components; *c* — titration borosilicate glass plates; *d* — optical parts from infrared glasses and VK7 glass for aerospace industry; *e* — crystals (calcium- and magnesium phtoride, sapphire, Nd:YAG) for microlithography and laser equipment

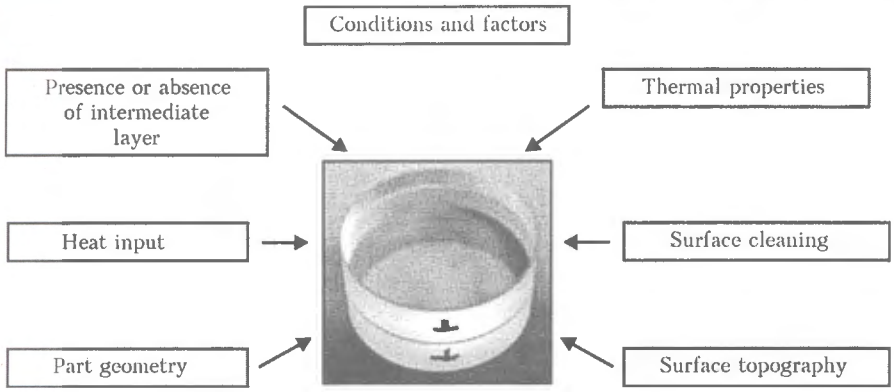

Figure 2. Conditions and factors influencing quality of diffusion-welded joints

place in bonding, in the contact plane, permanent joints between similar and dissimilar materials in solid state at elevated temperatures can be obtained. As a result, in the joint plane there develops a diffusion zone, whose properties define carrying capacity of the latter. To initiate diffusion processes, distance between atoms of materials being joined must be reduced to interatomic one; for their exchange a sufficient thermal energy is required. This implies preparation of the joint surfaces (their cleaning, protection against oxidation in welding), changing their geometry by applying pressure, as well as input of sufficient thermal energy. Diffusion welded joints, along with plane, can also be cone-shaped or cylindrical ones.

Theoretically, using diffusion bonding, any materials can be joined. Depending on their thermal, physical and chemical properties, different joining methods are used. Figure 2 shows conditions and factors influencing the diffusion bonding process. In an optimum case the adjoining surfaces get raised, forming a high-strength monolith structure.

Diffusion bonding of crystals, metals and ceramics is carried out at their below-melting temperatures. Contact surfaces at atomic level are produced by machining of joined surfaces, for instance by polishing. Thanks to the effect of temperature and pressure within a certain time interval, as well as presence of imperfections and dislocations of atomic lattice, process of atom transfer and/or exchange take place; in joining glass materials, for example silicon glass, similar joining mechanisms occur. Besides, this process is affected by conversion temperature T_g, meaning that diffusion bonding process occurs at T_g, comprising 50–60 % of melting temperature. As this takes place, in connection with the beginning of softening, of importance becomes stability of glass piece shape, as plastic deformations in the micro range may also contribute to the process of joint formation.

Consider a practical example of manufacturing elements from infrared glasses. Welded together were chalcogenide glasses IG3 and IG5, featuring high light transmission in the near and medium infrared wavebands. This material is suitable for making lenses and windows as has good characteristics in 3–5 and 8–12 μm waveband. Because of the different character of dispersion in joining these materials with each other and with other infrared materials, it is possible to obtain color correction and geometrical aberration of optical systems in the infrared waveband. With regard for the thermophysical properties (thermal expansion) of chalcogenide glasses IG3 and IG5, diffusion bonding is accomplished in the conversion temperature T_g range. Applied pressure has been chosen in accordance with geometrical features:

$$\Delta\alpha(20\text{–}100)\ ^\circ\text{C}/\text{IG3} - \text{IG5} = 0.6\cdot10^{-6}\ \text{K}^{-1};$$
$$\Delta\alpha(20\text{–}100)\ ^\circ\text{C}/\text{IG3} - \text{IG5} = 0.7\cdot10^{-6}\ \text{K}^{-1};$$
$$T_g/\text{IG3} = 275\ ^\circ\text{C};$$
$$T_g/\text{IG5} = 285\ ^\circ\text{C}.$$

On the basis of thermal and physical properties of the materials, for each combination welding conditions parameters were varied: temperature, welding time and pressure.

Diffusion bonding (Figure 3) was carried out in a vacuum furnace or furnace filled with shielding gas. Using SPS-control, various welding programs can be applied, with permanent computer-assisted process monitoring. Heating and cooling rates, depending on limiting permissible thermal load of the material, were 2–10 K/min, welding time was several hours.

Results of investigations, conducted using raster electron microscope, have proved that joint zone (Figure 4) is indistinguishable, i.e. compact joint of the materials has been obtained. Its optical properties from the point of view of light transmission were studied. Within 3–5 μm waveband losses due to dissipation and reflection were not detected.

Joints obtained using the above technique have the following advantages: sustain high limiting permissible thermal load, exhibit high mechanical strength and high cyclical thermal limiting permissible loading; retain their optical properties, for instance, ultra-violet permeability; are distinguished for their ageing resistance; there is a possibility to obtain joints without an intermediate layer (no introduction of impurities) and joints with large surface area (plane or irregular shaped).

Laser welding-soldering of glass. As opposed to quartz glasses, borosilicate glasses could not be reliably laser-welded up till now. The reason lied in different properties of the materials used (their expansion

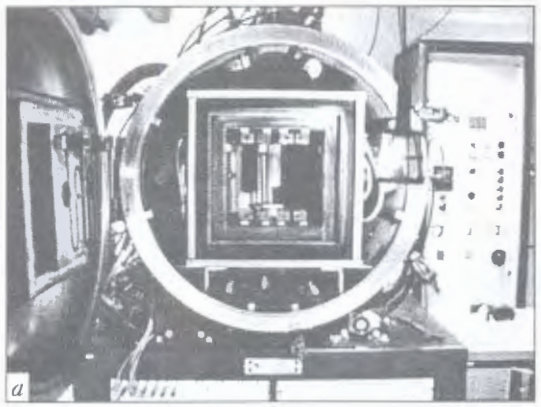

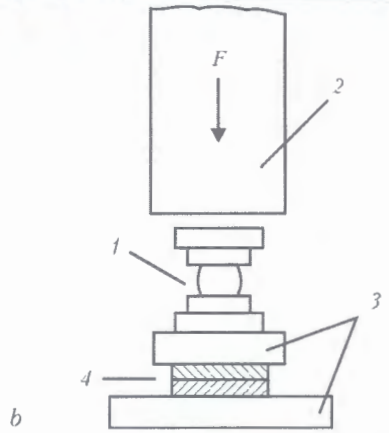

Figure 3. Appearance (*a*) and scheme of installation (*b*) for diffusion bonding: *1* — ball joint; *2* — punch; *3* — base plate; *4* — workpiece

coefficients). The task was set to accomplish a non-stressed joint of plane borosilicate glasses. New technological solution is based on a hybrid process, combining radiant and thermal energy and providing quasi non-stressed state of the glass joint. A substantial advantage of laser technology, compared to conventional methods of joining, is high quality of the weld. This method of joining glasses, used in various industries, deserves special consideration. To counteract high-temperature gradient occurring along the weld, a quickly travelling (up to 3 m/s) laser beam action is applied, so that thermal conductivity effects produce only a minor effect on the steady-temperature condition. After completion of the technological process, the joint can be subject to cooling, which almost completely eliminates the stresses.

Figure 5 shows a typical joint of two plane borosilicate glasses with coefficient of expansion $\alpha = 3.3 \cdot 10^{-6}$ K^{-1}. Length of the weld is 100 mm, width is 2 mm. A slight reinforcement of the face and root of the weld ensures its high strength features.

At the beginning, welds maximum 1500 mm long could be obtained. Length of quasi-parts is not limited, i.e. strips of unlimited length can be welded together. Thermostatically controlled chambers of large volume enable welding glass articles of different shapes. Moreover, controlling welding temperature, different silicate materials can be joined.

Another example of this technology application is laser soldering of silicon with glass, as when encapsulating micro-sensors on a substrate, using glass solder. To obtain a tight joint between silicon and glass, paste solder is squeezed through a template onto the

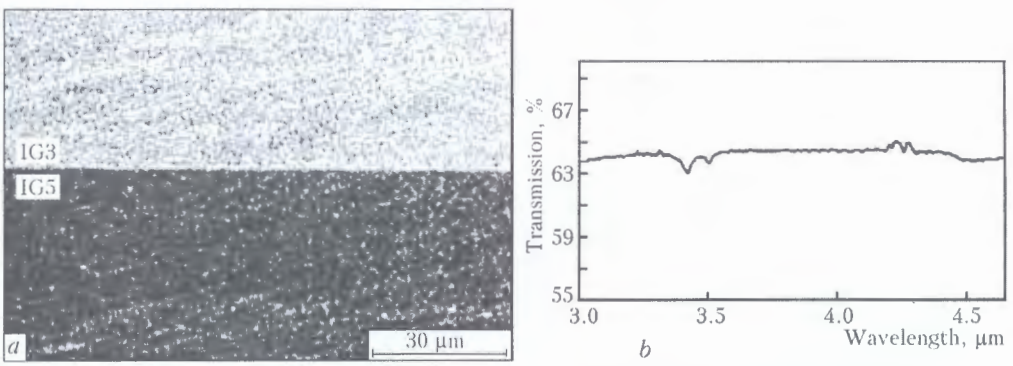

Figure 4. Microsection of the chalcogenide glass joint zone, obtained using raster electron microscope (*a*), and optical properties of the joint (*b*)

Figure 5. Schematic representation of butt joining process of plane glass (*a*) and its view under raster electron microscope (*b*)

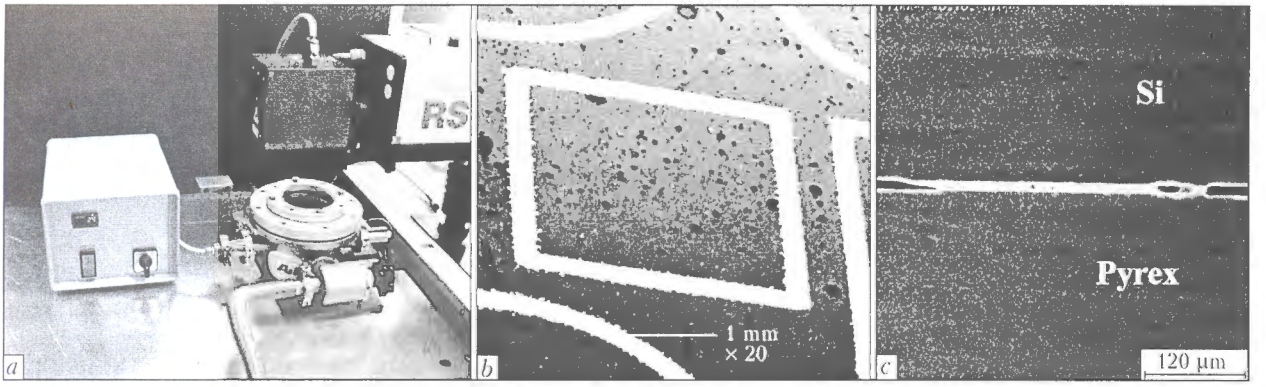

Figure 6. Nd:YAG laser scanner: *a* — vacuum chamber with controlled heating substrate; *b* — frame-like structure (3 × 3 mm), obtained using raster electron microscope; *c* — microsection of the laser-soldered joint

substrate, where at reaching some temperature it melts. After that, the glass solder layer is made level. After placing the silicon crystal and the substrate on the heating table, the joint is heated to below paste-melting temperature. Initial, required for phase transition and wetting energy, is supplied by the laser to isolated areas. Laser beam penetrates the glass, which transmits radiation of the required wavelength, and then it is absorbed by the glass solder. Due to their heat conductivity, silicon and glass in the joint zone experience indirect heating. The purpose of this joining technology is to minimize heat load on the entire system. Using this technique, one can obtain vacuum-tight low-stressed joints, in doing so, temperature load on semiconductor boards is essentially lower than glass solder melting temperature. Technology of glazing and levelling of template structures and their application onto the glass boards (Figure 6), ensuring contact of glass soldered joints with substrates all over their surfaces, with regard for the choice of the glass solder and design of the tested structures, has been certified.

Laser soldering is performed in a portable vacuum chamber, containing shielding gas and ceramic heating plate. To obtain low-stressed joint without pores, it is heated up to 330 °C, i.e. glass solder phase transition temperature. After multiple speedy passes of Nd:YAG laser scanning beam, each confined printed-on glass solder structure is heated up in a quasi-synchronous way. As an alternative, a diode laser with focus of specific contour, for instance linear one, can be used. In this case irradiation is carried out in a stationary device. In doing so, quality vacuum-tight soldered joint of upper glass plate to glass solder to substrate, is obtained. Investigations, aimed at qualitative and quantitative evaluation of the joints obtained, are not completed yet. At present, sample joints undergo optical and mechanical tests, their tightness and levels of stresses are being evaluated.

Adhesive joining of glass articles. Glass is a material, whose adhesive joining technology can be implemented meeting specific requirements. In oxide and silicate solids, such as glass, oxygen ions are the most reactive constituent, interacting with water molecules of the atmosphere. As a result, the so-called gel layer, consisting of permanent and temporary water shells, is formed. Thickness of the gel layer depends on the gas type and the environment conditions. Cleaning with solvents can only temporarily reduce the water shell, therefore new methods, providing stability of adhesive joints to climatic effects not affecting glass body strength, are required. Properties of glass surfaces, determined essentially by their chemical composition, greatly influence strength and long-term stability of adhesive joints (Figure 7). In this connection intensive search for methods of modifying glass surface is conducted. As an alternative, confined SiO_2 layers applied by Pyrosil method and different plasma-assisted joining methods, are used.

Adhesive joining is widely used in making composite glass items. Manufacturing optical devices is impossible without adhesive joining. Examples of this can also be manufacturing composite glass disks, multilayer non-splittering glass, automotive and railway car glasses. Ever wider, glues are used in manufacturing furniture and bath tubs. For this, new adhesive substances with improved properties, fit for continuous production, hardening under the effect of ultraviolet radiation and sunlight, yellowing (color-reversing), stable to temperature and humidity effects, exhibiting high strength, are being developed. By cementing glass to glass or other materials, it is possible, for instance, to manufacture composite acrylate glass articles, having reliable and strong UV-cured joints. Cementing together parts, subject to the effect of humidity, is rather costly, and as for now is possible only using silicon-based glues, whose strength is quite low. At present new glues, exhibiting both high

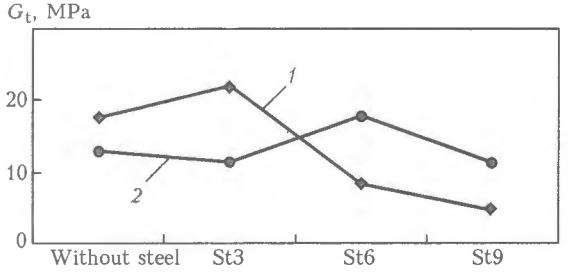

Figure 7. Dependence of strength of typical adhesive joints of alkaline silicate glass on the surface treatment type with atmospheric pressure plasma at different energy levels: *1* — UV-cured epoxy; *2* — UV-cured acrylate

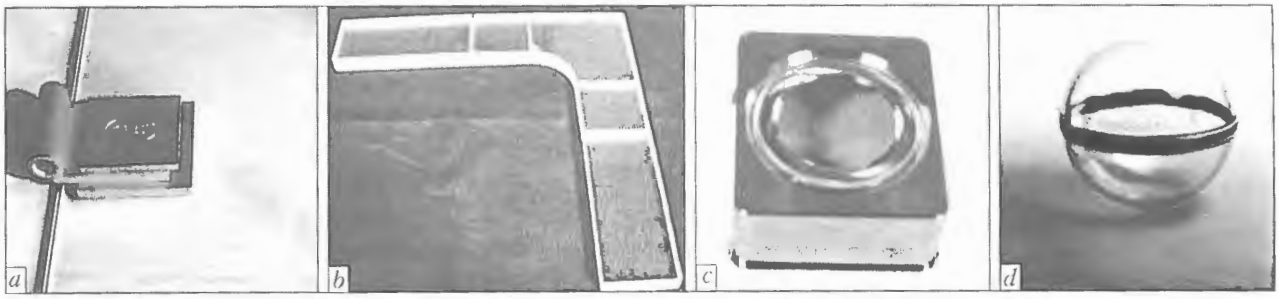

Figure 8. Samples of adhesive joints: *a* — glass door with aluminum framing; *b* — glass angle (section of glass structure); *c* — chamber body; *d* — ball for immersion into water during experiments in the sea

strength of existing structural and stability of silicon glues, are being developed. Adhesive and sealing substances on the basis of MS-polymers (liquid-crystalline or of medium softness), including those reinforced with epoxies, exhibit ultimate tensile and shear strength in non-aged state of up to 7 MPa. The wider the array of available adhesive substances, the more difficult it is to make the right choice of the optimum method of joining in each particular case. Therefore, in order to be able to use the advantages, various products adhesive technologies offer, more experiments have to be run. Implementation of a specific adhesive technology is sometimes quite difficult. It involves selecting proper adhesive substance, adhesive properties and technique for the industrial production process (long-term stability), and utilization method. For this, all-round investigations, based on the gained experience, are required. Figure 8 shows specimens of different adhesive joints.

Thus, the developments conducted at the Institute of Joining Technology and Materials Testing since 1991, are prerequisites for creating new products and novel methods of joining in glass, metalware and ceramic subindustries.

EBW OF ALUMINIUM ALLOY RIBBED HEAT EXCHANGERS (RADIATORS)

Environmentally clean and waste-free technology for high-efficiency manufacture of heat exchangers from aluminium and its alloys using electron beam welding was developed. This allows a 3–4 times decrease in weight characteristics of radiators, compared with the conventional ones made from copper or brass, and 40–60 % increase in their thermotechnical characteristics, while the use of electron beam welding for joining ribbed tubular elements to tube sheets provides the full-strength welded joints with base metal, almost absolute absence of distortions and retention of initial stiffness of the thin-walled ribs.

Basic operations of the developed technology are easy to automate and mechanise.

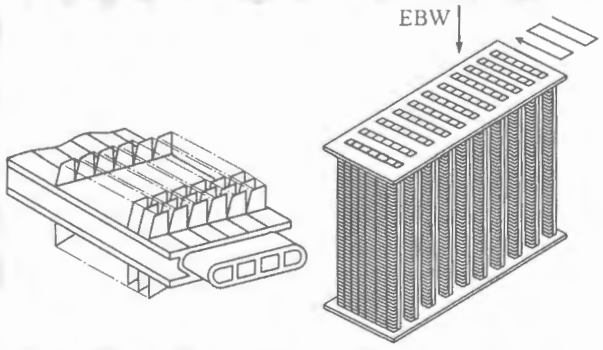

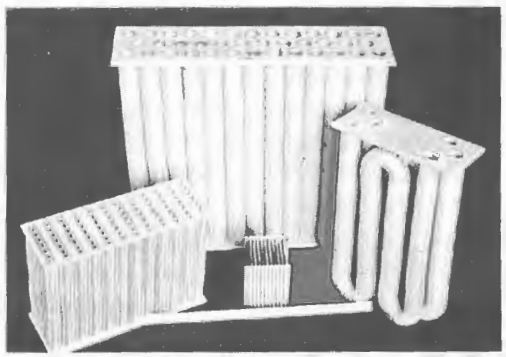

Application. Welded aluminium heat exchangers (radiators) can be applied in motor car and tractor construction, aircraft engineering, manufacture refrigerating facilities and compressor plants, manufacture of air conditioning devices, etc.

Proposals for co-operation. Development of technical documents, selling of know-how, technical consultations and engineering services in mastering of the technology and arrangement of production.

Prof. Ishchenko A.Ya.
E-mail: abondarev@gala.net; a_bondarev@ukr.net

POWER SOURCES WITH IMPROVED PERFORMANCE FOR AC ARC WELDING

I.I. ZARUBA, V.V. DYMENKO, V.V. ANDREEV and A.F. SHATAN
E.O. Paton Electric Welding Institute, NASU, Kiev, Ukraine

Considered are the features of operation of AC power sources with thyristor control, providing a high stability of the process and quality of welded joint formation. Data are given on AC welding, including root welds of pipe butt joints.

Keywords: *arc welding, alternating current, coated electrodes, welding transformer, thyristor regulation, magnetic blow, welding process stability, pipeline, root weld, butt joint, testing*

Manual welding of critical joints is usually performed with electrodes of the type of UONI-13/45, VI-10-6 and other, providing the required quality and sufficiently high stability of the welding process only at direct current. However, the latter is characterized by such a negative phenomenon as magnetic blow, which results from interaction of the magnetic field of the arc proper and welding circuit field. The arc runs in an unstable manner, randomly moving from edge to edge, despite all kinds of manipulations performed even by a qualified welder, this leading to an unsatisfactory formation of the weld metal. Particular difficulties are encountered during performance of the first weld of a butt joint (with edge preparation or into a narrow gap). Electromagnetic force acting on the arc, is proportional to the square of welding current and depends on the geometrical dimensions of the parts being welded and position of the current supply relative to the welding arc. Magnetic blow limits the application of highly efficient modes in direct current welding.

The simplest and most reliable means of eliminating magnetic blow in welding is application of alternating current. In this case the electromagnetic force acting on the welding arc, is determined by the resultant magnetic flow, equal to the geometric sum of magnetic flows of welding and eddy currents induced in the base metal bulk. As the components of these flows are almost in antiphase, their resultant value is small, so that manifestation of magnetic blow is much weaker compared to direct current. It becomes unnoticeable even at very high welding currents (up to 2000 A). Thus, more efficient welding modes can be used if alternating current is applied. Other advantages of alternating current are also known. For instance, welding in this case is much more cost-effective in terms of power consumption: efficiency of welding transformers is, as a rule, higher than that of direct current power sources. The design of welding transformers is simple, they require minimum maintenance or current repairs, so that the cost of their operation and maintenance is low.

In terms of technological impact on the pool, alternating current is similar to modulated current of 50 Hz frequency. Weld metal structure is more fine-grained, weld quality at alternating current is higher than in DC welding with electrodes of the same grade. In AC welding of aluminium and its alloys by a nonconsumable tungsten electrode in inert gases and their mixtures the process of removing the oxide films from the item to be welded is also very important. Therefore, nonconsumable-electrode argon-arc welding of aluminium is performed only at alternating current. However, despite certain advantages of the latter, its application in the current welding practice is not sufficiently extensive, particularly when making critical welded joints, including those requiring deposition of root and other types of welds. This is associated with a low stability of an AC arc running because of polarity reversal, arc extinguishing and striking (100 times per second at 50 Hz frequency), as well as negative influence of metal transfer under these conditions.

Investigations performed at the E.O. Paton Electric Welding Institute and the developed special device for arcing stabilization (DAS) [1] allow overcoming this disadvantage. Due to the use of currently available semi-conductor components, DAS are inexpensive small-sized devices, easily fitting into the casing of any welding transformer [2]. New types of transformers with DAS have been developed [3, 4], which, using all the qualities of an AC power source, are not inferior to welding rectifiers by their welding-technological capabilities, and ensure welding with practically any electrodes designed both for alternating and direct current.

As shown by experiments [5, 6], at arc powering by alternating current with DAS connection the welding transformer open-circuit voltage $U_{o.c}$ can be reduced right down to 37 V. However, the amplitude value of open-circuit voltage and rate of its rise to the ignition voltage decrease in this case, this being unfavourable in terms of ensuring a reliable re-ignition of the arc and process stability. Moreover, in the most widely accepted simple transformers with mechanical adjustment of welding current (moving magnetic shunt or movable windings) at $U_{o.c}$ lowering, the external volt-ampere characteristic of the source becomes flatter, short-circuiting current rises and metal spatter increases, accordingly, phase shift angle between voltage $U_{o.c}$ (t) and current $i_w(t)$ decreases, this being

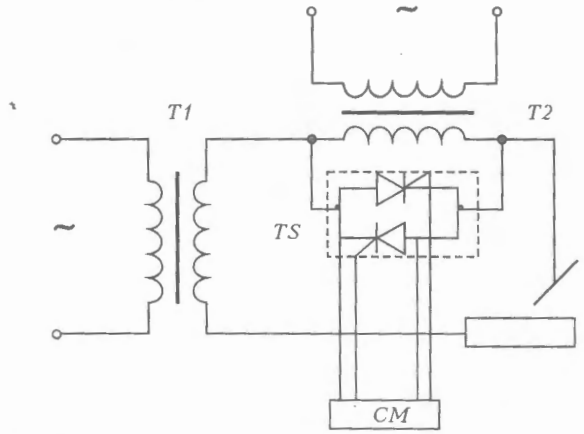

Figure 1. Block-diagram of thyristor-controlled AC power source (for designations see the text)

also undesirable in terms of process stability [7]. Therefore, $U_{o.c}$ lowering below 45 V is not rational in transformers designed for up to 300 A rated current. At $U_{o.c}$ = 45 V the consumption of active materials used in transformer manufacture noticeably decreases, weight and overall dimensions are reduced, and efficiency is increased [2].

Batch-produced transformers with mechanical adjustment of the welding mode usually have two ranges of welding current, generated by switching the coil pairs of the primary and secondary windings. In the range of small currents the coils are connected in series, and in the high current range they are connected in parallel. In the first case the value of magnetic induction in the transformer core is practically 2 times lower than in the second, i.e. in the small-current range the transformer magnet core turns out to be underloaded. Switches of welding current ranges installed in the transformers, often fail lowering the equipment reliability. Mechanical adjustment does not allow performing such manipulations of operating modes, as, for instance, welding current modulation, «hot» or «cold» starts, etc. Therefore, improvement of welding transformers is related primarily to transition from mechanical to electronic adjustment, which provides the required welding current in one range at an unchanged value of magnetic induction in the transformer core. One of the most important advantages of such adjustment is its fast response, which enables an essential expansion of the technological capabilities of the transformer by dosing the energy coming to the arc, also at transient processes caused by metal transfer.

The first welding transformers with devices for thyristor adjustment of current were introduced in 1980s [8]. Two thyristors in inverse-parallel connection were connected into the transformer primary or secondary windings for current adjustment. Compared to amplitude regulation thyristor transformers did not provide a continuous current in the secondary circuit, which is undesirable in terms of process stability. In submerged-arc welding with powerful closed arcs, the molten metal pool isolated from the environment, has a high thermal inertia, so that a quite stable process can be ensured at powering the arc from TDFZh-1002, TDFZh-2002 transformers with thyristor control in the primary circuit.

In welding with less powerful open arcs (for instance, with coated electrodes or in shielding gases) it is practically impossible to obtain a stable process. In this case, the so-called method of active «feeding» of the arc from an auxiliary low-power current source or other variants of maintaining the arc discharge are used [8]. To maintain a stable arcing in coated-electrode manual arc welding it is sufficient for the «feeding» current to be in the range of 10–35 A (depending on electrode diameter and welding mode).

Two circuits of thyristor-controlled welding transformers were proposed and studied at the E.O. Paton Electric Welding Institute. In the first of them the power and auxiliary transformers are made as individual assemblies (Figure 1). The second circuit is based on a common transformer having power and auxiliary windings.

The power source (see Figure 1) consists of the main (power) transformer *T1* designed for the rated load, and auxiliary transformer *T2*, which is made with developed dissipation and can operate for a long time in the short-circuit mode. An important component of the source is thyristor switch *TS* with the control module *CM*. External volt-ampere characteristics of such a combined power source have two branches. One corresponds to the main power transformer and is characterized by a comparatively low open-circuit voltage ($U_{o.c}$ = 40–45 V) and quite high short-circuiting current ($I_{sh.c} = 1.5–1.8I_{rat}$). The second (steeply-falling) corresponds to operation of the auxiliary power source ($U_{o.c}$ = 35–40 V, $I_{sh.c}$ = 25–30 A). Thus, the total open-circuit voltage of both the branches is in the range of 80 V. The source operates as follows. During welding when the current goes through zero the thyristor switch closes. A voltage surge appears in the discharge gap, which promotes a reliable re-ignition of the arc. When the control module generates a control pulse, thyristor switch is activated, and welding current rises, as the arc is now powered by the main source with the flat characteristic, low open-circuit voltage and considerable short-circuiting current. A smooth change of the mode in a broad range is achieved by adjustment of the angle of thyristor activation.

Figure 2, *a* gives the phase trajectory, which is the dependence of the rate of welding current variation di_w/dt on the value of this current. External branches of the phase trajectory correspond to arcing in the operation mode, inner branches — to arcing at the closed switch. Sections with low $di_w/dt = f(i_w)$ values correspond to a closed *TS* condition. With its opening the internal resistance of the entire source drops abruptly, and current, and, hence, di_w/dt, increase abruptly. For comparison, Figure 2, *b* gives $di_w/dt = f(i_w)$ phase trajectory obtained in welding with a regular welding transformer.

At a closed *TS* the total inductance of the welding circuit and phase shift between arc current and power

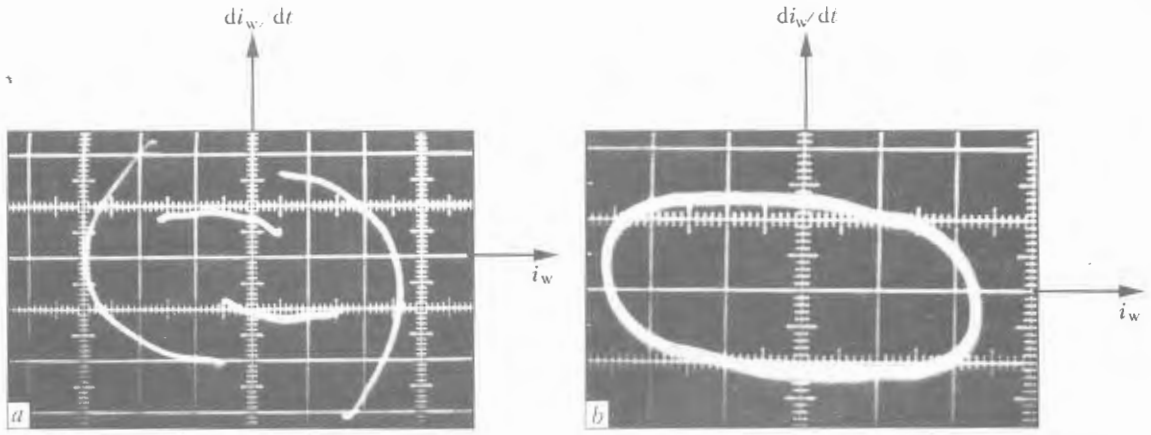

Figure 2. Phase trajectories $di_w/dt = f(i_w)$ obtained from thyristor-controlled AC power source (*a*) and from traditional welding transformer (*b*)

source open-circuit voltage rise, the voltage having a quite high amplitude value. All this promotes a reliable re-ignition of the arc and an increase of the coefficient of its stable arcing [7].

Adjusting the short-circuiting resistance of main *T1* and auxiliary *T2* transformers, it is possible to form the static and dynamic characteristics of the power source in a broad range. Calculations show that it is rational to manufacture such power sources for up to 500 A rated current.

Similar to the case of DAS application, use of «feeding» allows lowering the open-circuit voltage of the main welding transformer. However, it is necessary to take into account the fact that disturbance of the welding process stability at alternating current power supply [7, 9] is related to the change of polarity and to the nature of metal transfer, as well as the moment of drop separation during the half-cycle. Particularly dangerous are the coarse drops, separating from the electrode during the falloff of the welding current sinusoid half-cycle. They can de-ionize the arc column so much that after the polarity reversal, the arc will not reignite and the welding process will be interrupted. High-speed filming of the welding process and synchronous oscillography showed that the coarse drops move into the molten metal pool mostly at the end of the half-cycle during falloff of the current sinusoid, when the electromagnetic forces drop to a minimum, and the action of the gravity force together with the surface tension forces prevails. Under the impact of these forces the drop is sagging along the electrode axis, and the pool is leveled and flows under the electrode with the drop. Therefore, metal transfer is quite often accompanied by short-circuiting of the arc gap [10], which is extremely unfavourable for thyristor-controlled transformers. If switching on of the thyristor key at the change of polarity and power source transition to the working mode coincides with short-circuiting of the arc gap, a current surge runs in the circuit, which causes a rupture of the bridge between the drop and molten metal pool and drop ejection beyond the weld. Metal losses rise abruptly, and its spatter may exceed 30–35 %, which is absolutely inadmissible for technological reasons. In this case, it is necessary to ensure as small a current as possible at breaking up of the bridge. At short circuiting due to metal transfer, the arcing mode of the auxiliary (low-ampere) arc is to be extended, and switching into the working mode (high current) should be performed only after breaking up of the liquid bridge. Such an algorithm should be incorporated into the control circuit of the thyristor switch.

Thus, at development of thyristor transformers with DAS two mandatory requirements are applied, which should be satisfied by the control circuit:

- energy pulse generated by DAS for arc re-ignition should be applied to the discharge gap not only at polarity reversal, but also at any breaking of the arc during welding;
- at short circuiting caused by metal transfer by coarse drops at the falloff of the current sinusoid, thyristor switching on in the next half-cycle should be delayed up to the moment of rupture of the bridge between the electrode and molten metal pool in the arc «feeding» mode.

Figure 3 shows the block-diagram of thyristor-controlled welding transformer developed at the E.O. Paton Electric Welding Institute, which is a modification of the above power source, in which two transformers are practically combined. A common magnet core carries the primary *I* and four sections of the secondary winding (*II, III* — auxiliary and main one, respectively; *IV* — DAS feeding winding; *V* — feeding winding of thyristor control module). Welding current adjustment is performed using power thyristors *VS1*, *VS2*, which in the unblanked state range, shunt section *II* and choke *L1*. With completely unblanked thyristors, the welding current is maximum, and with blanked thyristors it is minimum. Current value is determined by leakage inductance of windings *III* and *II* and parameters of chokes *L1, L2*. Choke *L2* is introduced into the welding circuit only in the case, if leakage inductance of the transformer power winding is insufficient to obtain the required value of short-circuiting current.

Control of thyristor operation enables adjustment of current in transient processes caused by metal transfer both at the initial stage of the arc gap closing, and

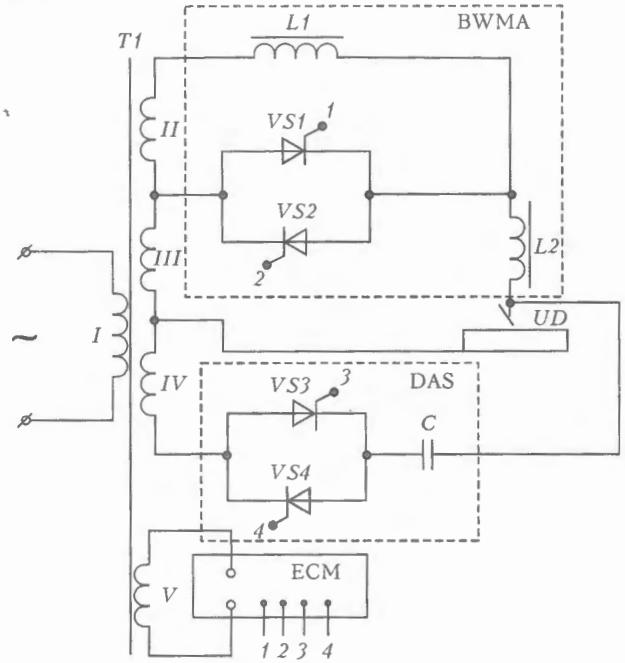

Figure 3. Block-diagram of TDT-251U2 power source (BWMA is the block of welding mode adjustment; for other designations see the text)

at the moment of rupture of the liquid bridge, this promoting a lowering of electrode metal spattering and improvement of weld formation.

Coated-electrode welding in all positions, except for the downhand position, is performed with a kind of modulation of current due to periodical electrode manipulation performed by the welder. At electrode displacement its tip is removed from the pool for a certain time, the arc becomes longer, current drops, and molten metal does not spread over the vertical or inclined surface. In this case, however, part of the arc energy is wasted in metal heating in the near-weld zone, and the molten metal of the pool periodically remains unprotected, thus impairing the weld quality. In the case of welding current modulation, performed by thyristor control, the arc stays continuously over the molten metal pool, providing its protection also during weld metal cooling, when the welding current drops. Welding current modulation provides an essential improvement of weld quality, even though it requires the welder to have certain skills, which are acquired in a very short time. As shown by experiments, in coated-electrode welding the modulation frequency should be selected in the range of 0.5–5.0 Hz, current pulse – 100–275 A, pause current – 50 A.

Figure 4. TDT-251U2 appearance

In the considered source the modes of the «hot» and «cold» start are envisaged. A reliable initial striking of the arc and the required penetration of the weld root are provided by applying the «hot» start, namely current increase at the moment of the electrode touching the item at the beginning of welding. It is achieved by a complete unblanking of the thyristors for 5–10 half-cycles of current. To avoid the item burn-through and electrode damage in nonconsumable electrode welding, the «cold» start is used, namely current lowering to a minimum value (of about 50 A) at arc striking by the contact method. It is performed by thyristor blanking for 5–10 half-cycles with subsequent transition to the specified welding current.

Technological testing of the designed thyristor transformer was conducted to GOST 25616–83 with additional assessment of arcing stability. Two grades of coated electrodes were mainly used: UONI-13/45 – electrodes with fluoride-calcium coating (for direct current), and MR-3 – with a rutile coating (for alternating current). Other electrodes, for instance VI-10-6, OZL-8, etc., were also used. Comparison in the same modes was conducted in welding using PSO-300 welding generator. It is established that welds obtained at powering of the welding arc from a thyristor transformer, practically did not differ in any way from welds made in DC welding. The new thyristor-controlled transformer TDT-251U2 (Figure 4) provided a high stability of the welding process both with AC and DC electrodes, being in no way inferior to welding rectifiers or generators as regards this parameter [9, 11]. TDT-251U2 advantages over DC welding power sources (generators and rectifiers) consist in the possibility of providing a sound narrow-groove welding of root welds also under other difficult conditions, when there is the risk of magnetic blow appearance.

Functional capabilities of the power source of TDT type enable conducting sound welding with coated electrodes of any grades designed for AC and DC welding.

TDT-251U2 specification

Mains voltage, V	380
Rated welding current (at 20 % duty cycle), A	250
Primary current at rated welding current, A	31
Range of welding current adjustment, A	50–275
Open-circuit voltage of power winding, V	45 ± 4
Open-circuit current, A	not more than 4
Rated working voltage, V	30
Rated power, kV·A	not more than 11.43
Efficiency, %	not less than 80
Power coefficient	not less than 0.82
Weight, kg	not more than 45

The power source enables consumable-electrode welding of carbon and some stainless steels (OZL-8

electrodes), cast iron (TsCh-4 electrodes), as well as nonconsumable-electrode welding of stainless steels, aluminium and its alloys in argon.

Production trials of the new power source of TDT-251U2 type with DAS have been conducted in welding butt joints of pipe billets of two typesizes in the following modes.

Sample (in Figure 5, *a*). Pipe diameter 114 mm, wall thickness 10 mm, edge bevel 70°, root face 2 mm, up to 3 mm gap, material – St3sp steel. Welding was performed with UONI-13/45 electrodes with the following welding modes:

- root weld was made by modulated alternating current. Modulation frequency was 0.5 Hz, pulse and pause duration were equal, pulse current was 110 A and pause current was 50 A, arc voltage was 22–25 V. Electrode diameter was 3 mm;
- filling pass was made by alternating current without modulation. Welding current was 140 A, arc voltage 24–26 V, electrode diameter 4 mm;
- facing weld was made by alternating current without modulation. Welding current was 150 A, arc voltage 25–26 V, electrode diameter 4 mm.

Sample (in Figure 5, *b*). Pipe diameter 57 mm, wall thickness 4 mm, edge bevel 70°, gap 2 mm, material – St3sp steel. Welding modes were as follows:

- root weld: pulse current was 95–98 A, pause current 50 A, arc voltage 24 V, modulation frequency 1 Hz, electrode diameter 3 mm;
- facing weld: pulse current was 110–115 A, arc voltage 24–25 V, electrode diameter 3 mm.

X-ray examination showed the operational suitability of the samples. TDT-251U2 source was also successfully tested in nonconsumable tungsten electrode welding of aluminium plates in argon.

Thus, the developed transformer with thyristor control allows conducting the following processes:

- coated-electrode welding of carbon steels (including those with basic coating of UONI-13/45, UONI-13/55 type, etc.), stainless and special steels (OZL-8, OZL-26, TsL-34, etc.), cast iron (TsCh-4);
- nonconsumable-electrode argon-arc welding of stainless steels, aluminium and its alloys in those cases, when initial arc striking by the contact method is permitted;
- welding of root, vertical and horizontal welds.

In addition, TDT-251U2 provides the following functions:

- smooth adjustment (local and remote) of welding current in one range;
- pulsed stabilization of arcing;
- welding current modulation;
- setting the required short-circuiting current before welding (depending on the mode and electrode diameter);
- «hot» (in consumable-electrode welding) and «cold» (in nonconsumable-electrode welding) starts;
- smooth reaching of the mode at the start of welding and crater welding up at the end of welding;

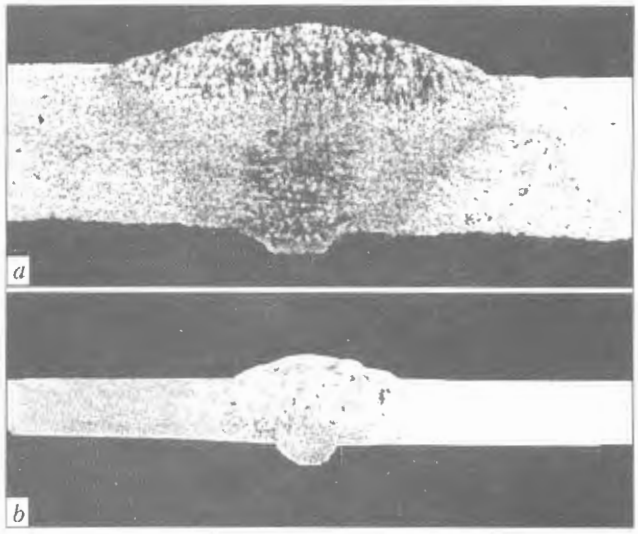

Figure 5. Macrosection of a joint of pipes of 114 (*a*) and 57 (*b*) mm diameter

- blowing with shielding gas after completion of welding;
- formation of various external static characteristics: from the drooping to bayonet.

TDT technological multifunctionality should be regarded as one of its advantages. This source combines to a certain extent the capabilities of AC and DC power sources.

Absence of mobile parts in TDT essentially improves its operational reliability. The cost of the control module is compensated by saving of electrotechnical materials in TDT manufacture and of power in its operation, as well as its higher technological indices compared to the traditional welding transformers and rectifiers.

TDT type power source can find application in fabrication and mounting of metal structures, laying pipelines, etc., which allows recommending it for coated-electrode welding of root and other types of welds on critical items.

1. Zaruba, I.I., Dymenko, V.V. (1982) AC arc stabilizers with dual control. *Avtomatich. Svarka*, **5**, 43–46.
2. Zaruba, I.I., Dymenko, V.V., Bolotko, V.I. (1989) Welding transformers with arc stabilizing devices. *Ibid.*, **10**, 46–51.
3. Zaruba, I.I., Andreev, V.V., Dymenko, V.V. (2001) Improvement of transformers for manual arc welding. *The Paton Welding J.*, **3**, 43–46.
4. Paton, B.E., Zaruba, I.I., Andreev, V.V. et al. (2002) Transformers for arc welding with arc stabilizing devices. *Svarshchik*, **2**, 8–11.
5. Pentegov, I.V., Dymenko, V.V., Sklifos, V.V. (1994) Welding power supplies with pulse arc ignition. *Avtomatich. Svarka*, **7**, 36–39.
6. Zaruba, I.I., Andreev, V.V., Dymenko, V.V. (2002) Improvement of technological effectiveness and efficiency of welding transformers. In: *Proc. of Int. Conf. on Welding and Related Technologies* (Kiev, 2002).
7. Zaruba, I.I., Dymenko, V.V. (1983) Influence of drop metal transfer on stability of AC welding arc. *Ibid.*, **12**, 14–20.
8. (1986) *Equipment for arc welding*: Refer. Book. Ed. by V.V. Smirnov. Leningrad: Energiya.
9. Zaruba, I.I., Andreev, V.V., Dymenko, V.V. (1982) Einige Wege zur Verbesserung des MAG-Schweissprozesses. *ZIS Mitteilungen*, **6**, 592–601.
10. Zaruba, I.I., Dymenko, V.V., Bargamen, V.P (1973) AC CO_2-welding. *Avtomatich. Svarka*, **10**, 64–68.
11. Zaruba, I.I., Andreev, V.V. (1998) Ways of improvement of thyristor power supplies. *Svarshchik*, **2**, 20–21.

ON HEATING AND ACCELERATION OF DISPERSE PARTICLES WITH PULSE PLASMA

M.L. ZHADKEVICH, Yu.N. TYURIN, O.V. KOLISNICHENKO and V.M. MAZUNIN
E.O. Paton Electric Welding Institute, NASU, Kiev, Ukraine

Heat exchange between the shock-compressed layer of pulse plasma and nickel particle of 60 μm size was studied. Numerical analysis of the characteristics of pulse plasma formed in the plasma-detonation accelerator has been performed. Influence of various components of heat exchange at particle heating in pulse plasma has been determined. The influence is shown of radiation heat exchange on heating of discrete particles and sprayed surface.

Keywords: *plasma-detonation spraying, pulse plasma, disperse particle, heat exchange, heat flux, radiation*

Variety of technical solutions for plasma accelerators, wide energy range of conditions of their operation, varying composition of the working mixture provide many possibilities to apply such devices in technological processes of surface treatment and depositing coatings. One of the examples of their implementation are plasma-detonation generators [1], whose advantages over DC arc plasmatrons and detonation-gas plants lies in the capability to accelerate particles to much higher speeds, in so doing density and temperature of the pulse plasma are quite high to ensure rapid heating of discrete particles of refractory alloys and oxides.

To determine the particle temperature, it is necessary to evaluate contribution of various heat exchange participants in their heating with pulse plasma flux, generated in discharging of capacitive energy accumulators based on combustible mixture detonation products (C_3H_8, O_2, N_2). Such evaluation is impossible without complex solution of the problem of determination of heat and gas-dynamic characteristics of ultrasonic plasmă flux, as well as efficiency of energy transfer to the surface of a spraying particle.

Using a mathematical model described in [2], calculation of characteristics of pulse plasma, generated by plasma-detonation accelerator, has been conducted for following parameters of electric-discharge circuit: inductance of circuit L = 15 μH, capacitor battery capacitance C = 800 μF, capacitor plates voltage U = = 3.2 kV. Here the accelerator length was 0.3 m, space between coaxial electrodes was 8 mm.

Calculations of plasma-detonation accelerator gave the following parameters of shock-compressed plasma layer: speed 4.6 km/s, density 8.5 kg/m^3, pressure 23 MPa, plasma temperature immediately behind the detonation wave was 14400 K. Such results correlate well with experimental data from investigation of energy parameters of pulse plasma, formed by plasma-detonation accelerator [3].

It is assumed that energy transfer from pulse plasma to disperse particles is basically realized through their acceleration and heating in the zone of shock-compressed plasma following the shock wave [4]. To evaluate efficiency of shock-compressed plasma effect on a disperse particle, the following assumptions are made: distance, over which plasma flow parameters change, is much greater than particle diameter and distance between them; particles are spherical; particle material does not react with the plasma; dispersion and collision of particles do not occur. Shock-compressed plasma is considered as a continuous medium, characterized by specific values of thermophysical parameters. Temperature, density and pressure in shock-compressed plasma layer are constant. Length of shock-compressed plasma layer is evaluated by technique of [5].

Consider gas-dynamic effect of plasma flux on a spherical particle. Equation, describing particle movement under the influence of aerodynamic resistance force, can be written as follows:

$$m_p \frac{du_p}{dt} = \rho_0 \frac{\gamma + 1}{\gamma - 1} \frac{(u_g - u_p)^2}{2} C_d \frac{\pi d_p^2}{4}, \qquad (1)$$

where m_p, u_p are the mass and speed of particle, respectively; ρ_0 is the initial gas density; d_p is the particle diameter; C_d is the coefficient of particle frontal resistance. For its evaluation the following criterial dependence is used [6]:

$$C_d = \frac{24}{\mathrm{Re}} \left(1 + \frac{3}{20} \sqrt{\mathrm{Re}} + \frac{11}{600} \mathrm{Re}\right), \qquad (2)$$

where Re is the Reynolds number.

Calculations, using the above model, show that with specified above accelerator parameters, a spherical nickel particle, having 60 μm diameter, within $4 \cdot 10^{-5}$ s is accelerated by shock-compressed plasma to 780 m/s, and interacts with the shock-compressed layer within 25–35 mm long distance.

Let us evaluate thermal effect of shock-compressed plasma on a disperse nickel particle. To calculate temperature field in a spherical particle moving in the supersonic plasma flux, non-stationary heat conductivity equation can be used:

$$c_p(T)\rho_p \frac{\partial T_p}{\partial t} = \frac{1}{r_p^2} \frac{\partial}{\partial r_p} \left(r_p^2 \lambda_p(T) \frac{\partial T_p}{\partial r_p}\right), \qquad (3)$$

where $T_p(\rho_p, t)$ is the space and time temperature distribution; r_p is the distance to particle center; $c_p(T)$, ρ_p, $\lambda(T)$ is the effective heat capacity, density and heat conductivity coefficient of particle material, respectively.

Initial and boundary conditions for equation (3) are assumed as follows:

$$\left.\frac{\partial T_p}{\partial r_p}\right|_{r_p=0} = 0; \quad T_p(r_p, 0) = T_p^0; \quad \left.\left(\lambda_p \frac{\partial T_p}{\partial r_p}\right)\right|_{r_p=d_p/2} = Q,$$

where T_p^0 is the initial particle temperature; Q is the heat flux input into a particle.

Integrating equation (3) within 0 to r_p range, we obtain

$$m_p c_p \frac{dT}{dt} = 4\pi r^2 Q. \quad (4)$$

To calculate heat flux input into a particle under conditions of thermal spraying of coatings, only convective constituent of the heat flux is used as a rule [7, 8], which is acceptable at gas temperatures below 4000 K.

Plasma-detonation accelerator generates shock-compressed plasma, where the temperature exceeds 8000 K, consequently, together with convective, also radiation constituent of heat exchange must be taken into account. Let us represent heat flux input into a particle as a sum of two constituents:

$$Q = Q_k + Q_l, \quad (5)$$

where Q_k is the convective constituent of heat flux input into a particle, determined by the following relation:

$$Q_k = \alpha(T_g - T_p); \quad (6)$$

Q_l is the radiation constituent, calculated by the following dependence:

$$Q_l = \xi\sigma_0(T_g^4 - T_p^4). \quad (7)$$

In equations (6) and (7) α is the heat exchange coefficient; T_g, T_p are the temperatures of plasma and particle, respectively; ξ is the reduced to heat radiation spectrum averaged degree of blackness of particle material; σ_0 is the Stefan–Boltzmann constant.

Heat exchange coefficient is calculated in the following way:

$$\alpha = \frac{\lambda_g(T)\mathrm{Nu}}{d_p}, \quad (8)$$

where $\lambda_g(T)$ is the plasma heat conductivity; Nu is the Nusselt number [9]. Heat exchange coefficient (8) can be calculated based on criterial dependence [10]:

$$\mathrm{Nu} = 2\exp(-\mathrm{M}) + 0.459\mathrm{Re}^{0.55}\mathrm{Pr}^{0.33}, \quad (9)$$

where M is the Mach number; Pr is the Prandtl number [6].

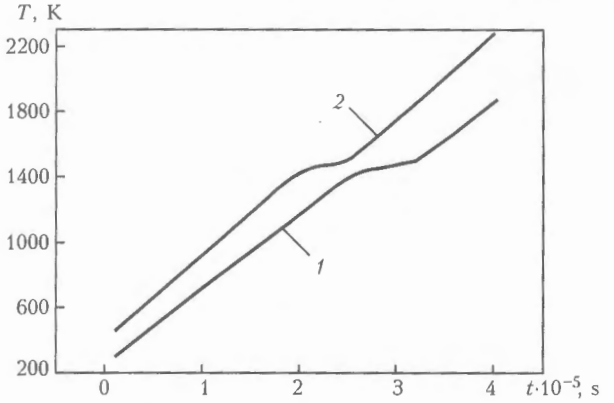

Temperature change of particles moving in a shock-compressed layer of pulse plasma: *1* – Q_k; *2* – $Q_k + Q_l$

The Figure shows temperature change of a particle heated with shock-compressed plasma, with regard for radiation and convective constituents of heat exchange. Calculated data were obtained as a result of numerical solution of equation (4) with regard for (5)–(9). Analysis of the data obtained shows that at plasma temperature exceeding 8000 K radiation constituent must be taken into account. Particle temperature with account of convective or radiation heating is 10 % higher. It should be noted that influence of radiation-induced heat exchange on particle heating begins at the stage of plasma formation in the accelerator, while convective heat exchange occurs only in passing of shock-compressed gas through a cloud of particles.

It has to be concluded that radiation heat exchange plays a substantial role in heat exchange of pulse plasma with spraying particles. Thus, in particular, in spraying nickel particles, having diameter of 60 μm, radiation constituent increases particle temperature by more than 10 %. In this case time of particle staying in the shock-compressed plasma is $4\cdot10^{-5}$ s, and its acceleration to 780 m/s occurs within a 25–35 mm long path.

1. Yushchenko, K.A., Borisov, Yu.S., Tyurin, Yu.N. (1994) Plasma-detonation processes of formation of energy flows and their interaction with metal surface. In: *Transact. on Physics and Technique of Plasma*. Vol. 2. Minsk.
2. Pogrebnyak, A.D., Tyurin, Yu.N. (2005) Modification of material properties and deposition of coatings using plasma jets. *Uspekhi Fiz. Nauk*, **175**, 520–522.
3. Tyurin, Y.N., Pogrebnjak, A.D. (2000) Advances in the development of detonation technologies and equipment for coating deposition. *Surface and Coatings Technol.*, **111**, 269–275.
4. Shkolnikov, E.Ya., Guzeev, M.Yu., Maslennikov, S.P. et al. (2000) Acceleration of microparticles in electrothermal accelerator with multidischarging circuit of discharge module. *Pribory i Tekhnika Eksperimenta*, **6**, 130–135.
5. Gurovich, V.Ts., Desyatkov, G.A., Spektorov, V.L. et al. (1987) Specifics of current envelope and shock wave in high pressure pulse accelerator. *Doklady AN SSSR*, **5**, 1102–1105.
6. Lebedev, A.D., Uryukov, B.A. (1990) *Pulse accelerators of high-pressure plasma*. Novosibirsk: ITF.
7. Zverev, A.I., Sharivker, S.Yu., Astakhov, E.A. (1979) *Detonation spraying of coatings*. Leningrad: Sudostroenie.
8. Shorshorov, M.Kh., Kharlamov, Yu.A. (1978) *Physical-chemical principles of gas-detonation spraying of coatings*. Moscow: Nauka.
9. Landau, L.D., Lifshits, E.M. (1986) *Theoretical physics*. Vol. 6. Moscow: Nauka.
10. Kutushev, A.G., Tatosov, A.V. (1998) Mathematical modeling of emission of gas suspension from channel of shock tube under the action of compressed gas. *Fizika Goreniya i Vzryva*, **3**, 107–116.

SCHEMATIC FOR CONTROL OF WELDING MACHINE DRIVES

Yu.N. LANKIN, Yu.A. MASALOV and **E.N. BAJSHTRUK**
E.O. Paton Electric Welding Institute, NASU, Kiev, Ukraine

A simple schematic has been developed for control of motors of welding machine drives. Its static characteristics are described and oscillograms of the drive acceleration braking are given.

Keywords: *arc welding, electroslag welding, welding machines, drive, controlling, wire feed speed*

In controlled electric drives of welding machines, direct current motors are widely used. As a rule, these are non-reversible drives having 1:10 control range*. Development of modern component base enables to design simple control circuits with rather high technical characteristics. One of such circuits is shown in Figure 1.

To control motor speed a pulse-width converter (PWC) implemented on the basis of field-effect power transistor *VT*1 and controller *DA*1 (TL494). Switch-on frequency of *VT*1 transistor (10 kHz) is set by resistor *R*1 and capacitor *C*1. Disengagement amplifier *Y*1 of controller DA1 controls relative transistor switch-on time. Non-inverting input of the amplifier through resistor *R*3 is fed with voltage from potentiometer *R*7 setting the speed, while through resistor *R*4 comes motor speed feedback voltage from output of amplifier *DA*2.

Pulse-width modulated output pulses of controller *DA*1 control transistor *VT*1, connected into the armature circuit of motor *M*. Armature voltage through resistor *R*11 is fed to the inverting input of amplifier *DA*2, while to its non-inverting input through resistors *R*10, *R*12 from shunt *R*12 is fed voltage proportional to motor armature current. As a result, at the output of amplifier *DA*2, proportional to motor speed voltage is formed, which is also fed to non-inverting input of amplifier *Y*2 of controller *DA*1. To the second input of the amplifier comes reference voltage of setting maximum motor current. With armature current exceeding allowable set maximum (for instance in starting, short circuiting, motor overload, etc.), PWC assumes current stabilization mode.

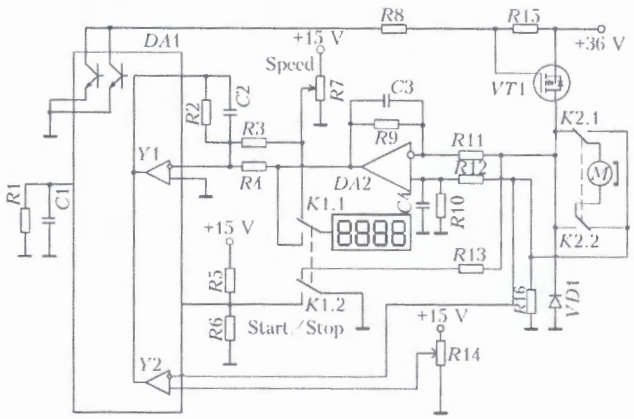

Figure 1. Schematic diagram of drive: *VD*1 — protection diode; *C*2–*C*4 — filtering capacitors (for other designations see the text)

Contactor *K*1.2 (Start/Stop) controls motor rotation switching on/off. Contacts *K*1.1 switch over input of motor speed digital indicator from speed setting potentiometer *R*7 to the output of amplifier *DA*2. Thus, with cut-off motor, the indicator shows the set motor speed, while when it is switched on — measured one. Digital indicator is calibrated in preferred measurement units of drive speed, for instance in meters per minute.

Static characteristics of the control system are shown in Figure 2. It is seen that coarseness of drive characteristics meets the requirements to the drives designed for feeding electrode wire of welding semiautomatic welding machines and drives of carts of automatic welding machines. It presents no difficulty to make load characteristics of any degree of coarseness, having increased the depth of motor current positive feedback, however in so doing, there is a danger of loss of controlling stability. Deep negative voltage feedback of motor armature practically excludes influence of mains voltage oscillations on the speed of the latter.

For dynamic braking of motor in stopping, the armature circuit is shunted by resistor *R*1 through contact *K*1.2. Curves of motor speeding-up and braking are shown in Figure 3. Motor speeding-up time is about 0.25 s when maximum motor current is limited to14 A; braking time is about 0.15 s, which can be made shorter by reducing resistance of *R*13. Time for program change run-out of speed setting is less than mentioned above, and decreases with decreased task jump.

The schematic described has been developed for control of motors *D*25–*D*90 types, but can also be applied to motors of other types, having similar power and supply voltage.

*(1986) Automation of welding processes. Ed. by V.K. Lebedev and V.P. Chernysh. Kiev: Vyshcha Shkola. 296 pp.

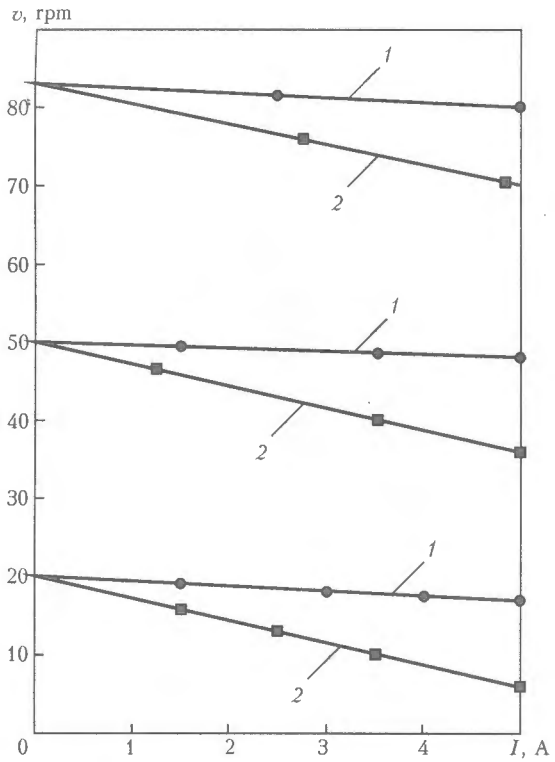

Figure 2. Static characteristics of drive with (*1*) and without (*2*) positive current feedback

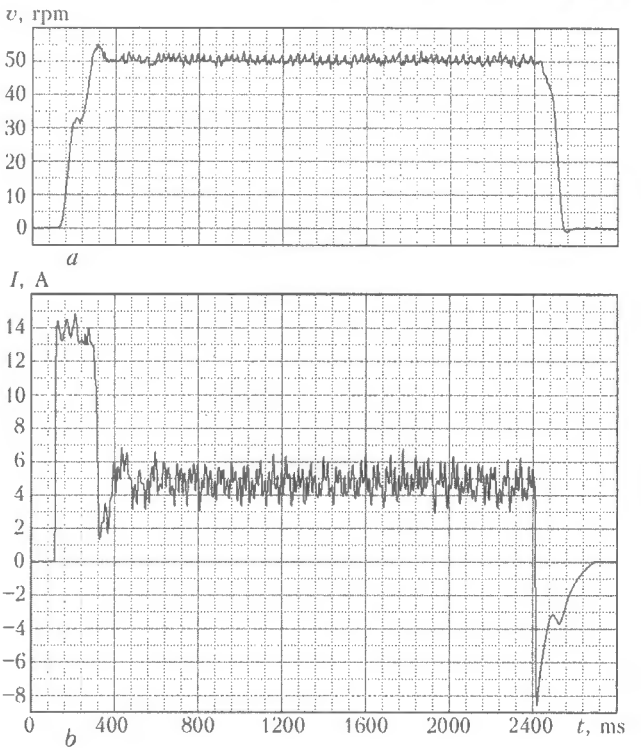

Figure 3. Oscillograms of drive (*a*) and current of motor armature (*b*) in drive speeding-up–braking

In most applications technical characteristics of the described drive meet the requirements for drives of welding equipment. For systems of automatic control of arc voltage, systems of electrode weaving, discrete feeding of consumable electrode and others, a reversing drive with improved dynamic characteristics at the stage of speed deceleration (braking), is necessary. In this case drive circuits are becoming substantially more complicated; PWC bridge circuit and more complex algorithms of transistor control are used, which both increases the cost and reduces reliability of the drive.

In applications, where exact positioning, high-speed response, or a wide drive speed variation range is required, more complex drives with motor speed sensors should be used. However, expenses in this case may amount to hundreds of US dollars.

TECHNOLOGY OF MANUFACTURING LIGHT-WEIGHT WELDED CYLINDERS

The technology was developed at the E.O. Paton Electric Welding Institute and is aimed at solving two priority problems, namely lowering the specific weight and increasing the operating reliability. The novelty consists in the laminated structure of the cylinder wall and a rational combination of metals with different physico-mechanical properties.

The new approach to the technology of cylinder manufacturing allows using metals with a high specific strength, and, therefore, reducing the item weight by 30 to 50 %; increasing the operating reliability by minimizing the structure imperfections associated with the welds located on the cylindrical part and the nozzle; making the technology simple and accessible for implementation under the factory conditions.

There are no foreign analogs.

Pilot production batches have been made of cylinders of small and medium volume for the working pressure of 14.7 MPa (150 kg/cm^2) with the strength margin of 2.6 according to the DNAOP 0.00-1.07–94 Rules. Technical documentation for cylinders manufacture has been developed.

Application. Storage and transportation of pressurized gases.

Contacts: Prof. Garf E.F.
E-mail: yupeter@ukr.net

THESIS FOR A SCIENTIFIC DEGREE

E.O. Paton Electric Welding Institute of the NAS of Ukraine

A.I. Bely (EWI) defended on the 14th of June 2006 the Candidate's thesis on speciality «Welding and Allied Technologies» on the subject «Materials and Technology of Hardsurfacing Drill Pipe String Elements by a Composite Alloy» (Scientific Leader — Dr. A.P. Zhudra).

The thesis is dedicated to creation of the material and technology of plasma hardsurfacing of composite alloys based on fused tungsten carbides applied for strengthening of external surface of drill pipes locks. Analysis of the existing methods for lock strengthening shows the advantages of applying on the locks composite alloys based on tungsten carbides as application of cast hardfacing alloys requires deposition of wear-resistant layers more than 3 mm thick that leads to deterioration of well washing. The optimal method for obtaining composite alloys by applying plasma arc and filler material of band spherical tungsten carbide was determined.

On the base of theoretical and experimental studies of friction pair «lock–casing pipe» it was determined that the lock external surface strengthening by cast and composite materials does not lead to increase of casing pipe wear. In the range of real loading conditions of up to 5 MPa wear decreases with the increase of cast surfacing alloy hardness and the increase of armed particle concentration in the composite layer up to 40 % of its volume and higher. With the aim to create a simultaneous contact of reinforcing particles and composite alloy matrix of the strengthened lock surface with the casing pipe material, it is expedient to remove the reinforcing particles from the upper volumes of the alloy, and form an interlayer of matrix alloy over the reinforcing particles.

A mathematical model of compose alloy formation was designed that allows determining the main principles of obtaining the necessary ratio of reinforcing particles and matrix of the deposited metal due to lowering of the maximum heating temperature of reinforcing particles surface and limitation of the time of interaction of particles and matrix melt. It is achieved by applying a nickel coating on them or creating cooling effect of the weld pool when specific volume of reinforcing particles is higher than 40 %. The second method is more rational.

The procedure of quantitative analysis of matrix components was developed, namely solid solution of tungsten in iron, eutectic and secondary iron-tungsten carbides. Optimum matrix properties were registered when the content of tungsten solid solution structure in iron was not less than 55 % of the volume, and structures of the eutectic and secondary iron-tungsten carbides were not more than 35 and 10 % of the volume, respectively. The quantity of reinforcing particles should make not less than 40 % of the volume in the composite alloy. The weight fraction of matrix components is determined by optical emission spectral method. The patent on matrix analysis method is received.

Weld pool deoxidation and alloying by aluminum speeds up the passage of reinforcing particles through the melt, promotes a shortening of the time of contact with weld pool metal. This also provides more uniform particle distribution through the volume of the deposited layer, absence of wear-resistant phase on the surface of composite alloy and simultaneous contact of reinforcing particles and matrix with casing pipes that substantially decreases their wear.

With the aim to prevent brittle secondary iron-tungsten carbides formation in the matrix of composite alloy, weld pool was alloyed with titanium in the amount from 1.3–1.5 to 2.6–3.0 wt.%, that binds carbon into fine carbides. That allowed creating for mechanism influencing the process of dissolving of reinforcing particles and providing optimum matrix formation and correlation of its structural components. Obtained results were the basis for development of the composition of filler material for plasma deposition of composite alloys that was protected by the author's certificate.

The method of plasma hardfacing of composite alloys was developed and protected by the author's certificate. Industrial technology and a series of equipment for automatic plasma hardfacing were designed for drill pipes locks. Extensive industrial testing showed that wear resistance of drill pipes locks deposited by composition alloy is not less than 3 times higher in comparison with unfaced ones. The author's certificate and the patent were received for drill pipe lock design with a hardfaced external surface.

THESIS FOR A SCIENTIFIC DEGREE

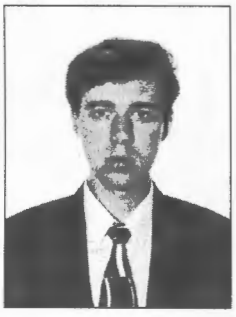

E.O. Paton Electric Welding Institute of the NAS of Ukraine

E.V. Shapovalov (EWI) defended on the 14th of June 2006 the Candidate's thesis on speciality «Automation of Technological Processes» on the subject «Instruments of Technical Vision as a Feedback Element in Following Systems for Arc Welding» (Scientific Leader — Prof. F.N. Kisilevsky).

The thesis is dedicated to the development of the instruments of technical vision for following systems for a square-groove butt. To solve this problem TV method was suggested that is based on computer processing of video images of the butt joint line illuminated simultaneously by sources of structured and diffuse light. When illuminating a butt with the gap close to zero by the source of diffuse light the beams that penetrated into the gap between parts being welded are practically completely absorbed. The butt joint line on the video image looks like an extended dark strip. Computer processing of such a video image allows one to determine the direction of butt joint line. The distance to welded surfaces is determined using the light section method. The developed method permits calculating the actual deviation of the welding tool from the butt joint line.

The method for selection of laser irradiation, diffusively reflected from the metal surfaces being welded is suggested. It is shown that diffusively reflected laser radiation is depolarized much stronger than mirror reflection that permits by means of polarized light filter to blank mirror component from penetrating into the video camera lens.

Adaptive control of a scattered light source is performed by a specialized controller due to the change of PWM frequency of micro processor converter, thus providing sensor invariance to optical properties of welded surfaces.

Experimental and theoretical studies of argon arc spectra that were carried out permitted to make a valid selection of optical ranges of waves of visible and short infra red spectrum. The most acceptable for operation of technical vision instruments are ACS of argon arc welding.

It was shown that in the optical circuit of technical vision instruments, based on laser location method, in order to increase the signal-to-noise ratio, it is advisable to use a polarized light filter that is mounted on the video camera lens, this allowing the signal-to-noise to be increased in practice.

A mathematical model was developed for identification of butt joint image in the video images with the capability of self-teaching. Step-by-step method for taking decisions about objects belonging to classes was realized in this model that allows substantially decreasing the calculation volumes and applying the designed model in real time systems.

Modelling of process of torch guidance to the butt with the help of modern program package MATLAB/Simulink was carried out in the work. Created Simulink model allows studying the stability and behaviour of the tracking system for different operating modes of the sensor and tuning regulator parameters.

COOPERATION BETWEEN PWI AND BRAZILIAN WELDING SOCIETY

There are almost 10 years as the Education, Training and Qualification Harmonized System of the International Institute of Welding (IIW) exists. It was taken over from the European Welding Federation (EWF), which had introduced it in 1991.

This International Education and Qualification System for Welding Personnel is the only system recognised worldwide and also by ISO and CEN bodies.

Companies that are seeking certification, according to EN 729/ISO 3834, need to comply with the personnel requirements. The IIW and EWF qualification system is mentioned in EN 719/ISO 14731 as a way for welding co-ordination personnel to achieve the standard qualification requirements.

So far the following IIW Guidelines have been developed: «International Welding Engineer – IWE», «International Welding Technologist – IWT», «International Welding Specialist – IWS», «International Welding Practitioner – IWP», «International Welding Inspection Personnel – IWIP», and «International Welder – IW».

The International Welding Instructor and the International Welding Designer Guidelines are going to be introduced soon.

In each country there is an appointed organisation to be responsible for ensuring that the standards of education, examination and qualification are maintained and that IIW qualified personnel at a certain level will have achieved the same minimum level of knowledge, irrespective of the country in which they had been qualified. These organisations are known as the IIW Authorised National Bodies (ANBs). An ANB accepts responsibility for the implementation of the current IIW system for education, examination and qualification of welding personnel at the national level. The Ukraine ANB is the E.O. Paton Electric Welding Institute Training and Qualification Centre (PWI TQC).

There are now 32 countries that have ANBs: Australia, Austria, Belgium, Bulgaria, Canada, China, Croatia, Czech Republic, Denmark, Finland, France, Germany, Hungary, Iran, Italy, Japan, the Netherlands, Norway, Poland, Portugal, Romania, Russia, Serbia and Montenegro, Slovak Republic, Slovenia, South Africa, Spain, Sweden, Switzerland, Thailand, Ukraine and United Kingdom. Some countries are applicant ANBs including Brazil, which is represented in the IIW by the Brazilian Welding Society (Associacao Brasileira de Soldagem).

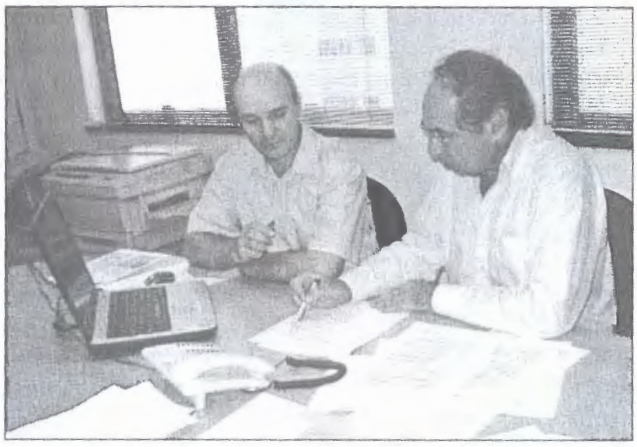

Brazilian ANB application paper set preparation (on the left Vladimir Ponomarev – Ukrainian ANB chief executive; on the right Daniel M. de Almeida – Brazilian ANB chief executive)

The implementation of the IIW system for education, examination and qualification of welding personnel at the national level is a complex and long-term process. That is why an applicant ANB normally to seek help to an ANB which has already a respective experience. The Brazilian Welding Society has been rendered such an assistance by the PWI TQC.

It is a good base for further enlargement of a cooperation between Ukrainian and Brazilian ANBs, as well as between PWI and Brazilian Welding Society.

V. Ponomarev